Studying Unmodeled Physics from Gravitational Wave Data

by

Guillaume Dideron

A thesis
presented to the University of Waterloo
in fulfillment of the
thesis requirement for the degree of
Doctor of Philosophy
in
Physics

Waterloo, Ontario, Canada, 2024

© Guillaume Dideron 2024

Examining Committee Membership

The following served on the Examining Committee for this thesis. The decision of the Examining Committee is by majority vote.

External Examiner:	Katerina Chatziioannou Assistant Professor of Physics, California Institute of Technology
Supervisor(s):	Luis Lehner Adjunct Faculty, Dept. of Physics and Astronomy, University of Waterloo Perimeter Institute for Theoretical Physics Avery Broderick Professor, Dept. of Physics and Astronomy, University of Waterloo
Internal Member:	Niayesh Afshordi Professor, Dept. of Physics and Astronomy, University of Waterloo
Internal-External Member:	Achim Kempf Professor, Dept. of Applied Mathematics, University of Waterloo
Other Member(s):	Huan Yang Adjunct Faculty, Dept. of Physics and Astronomy, University of Waterloo Professor, Dept. of Astronomy, Tsinghua University

Author's Declaration

This thesis consists of material all of which I authored or co-authored: see Statement of Contributions included in the thesis. This is a true copy of the thesis, including any required final revisions, as accepted by my examiners.

I understand that my thesis may be made electronically available to the public.

Statement of Contributions

The research presented in Chapters 2 and 3 are based on [71]. The ideas in this work were developed with Suvodip Mukherjee and Luis Lehner, while I carried out the implementation and numerical work. Chapter 4 is an extension of this work, based on as a publication in preparation with the same authors. Chapter 5 covers parts of a publication [57] I contributed to. The numerical work in this paper was primarily done by Max Corman. I participated in parts of the formulation of the "fixed equations" and in analysing their constraint behaviour.

Abstract

This thesis explores the detection and analysis of unmodeled physics in Gravitational Wave (GW) data. To this end, we develop the `SCoRe` framework, which uses the Correlated Residual Power Spectrum (CRPS) between pairs of detectors to identify deviations from our Standard Model (SM) of GW. This model includes General Relativity (GR) as the theory describing gravity, binary Black Holes (BHs) and Neutron Star (NS) merging as the sources of GWs, our model of the noise in the detectors, and the template waveform models used for data analysis.

The thesis starts with a theoretical overview of GW physics, including an overview of GR, and how it describes the way GWs are generated and how they propagate and interact with matter. We then discuss the practical aspects of GW detection: the modelling of the noise in the detectors and the data analysis techniques used to extract and interpret GW signals.

Next, we describe the `SCoRe` framework in Chapter 2, which is designed to distinguish between noise and deviations from the SM, while also shedding light on the underlying physics of the deviation. We detail its three main components: cross-correlating residual power between detectors, projecting onto physically motivated or agnostic bases, and combining information from multiple events by assuming a dependence of the unmodeled physics on the source parameters.

To illustrate the method, we apply the `SCoRe` framework to toy models in Chapter 3. We demonstrate how the method can recover unmodeled signals without prior assumptions about their form, how to choose the timescale of cross-correlation, and how the method can be used to perform a null test of the SM.

In Chapter 4, we then forecast the precision with which the `SCoRe` method can recover a deviation from the SM from a population of Binary Black Hole (BBH) mergers observed by a network of third-generation GW detectors. As the method leverages the dependence of the deviation from the SM on the source parameters, we investigate the effect the distribution of these parameters has on the method. For a model where the deviation scales with the chirp mass as a decaying power law, we show that the precision of the constraints on the deviation decreases as the power law becomes steeper. This has implications for constraining higher-dimensional operators in Effective Field Theories (EFTs) of gravity: higher dimensional operators correspond to steeper power laws and are, therefore, harder to constrain with the method.

Finally, in Chapter 5, we illustrate another approach to testing the SM of GWs, where the GW signal in an alternative theory of gravity is numerically computed. We give an

overview of the mathematical challenges and describe a method, the "fixing the equations" method, which aims to reduce pathologies in evolving EFTs of gravity by controlling energy flow to high frequencies.

Acknowledgements

Thank you Luis, for encouraging and supporting me through all the opportunities and tribulations that popped up during this journey. Thank you for your patience with me. I am grateful to have worked with Suvodip, who always made it seem like all the mysteries of the universe were just a little bit of hard work away.

I would also like to thank the members of my committee for reading this thesis and providing feedback.

I had a wonderful time at PI with the wonderful people there. So many discussions and ideas, physics and non-physics, that I will always remember. I am grateful to the facility, admin, and bistro staff, who made working at PI a true pleasure. Many of the computations in this thesis were performed on Symmetry at PI, and I thank all the people who keep it unbroken.

I feel lucky to have met so many great people over the last few years—Tim, Hassan, Qiaoyin, Ramigo, Francisco, Conner, Adrian, Sotiris, Jordan, Bruno, Rufus, Nanna, Ami, Barbara... (any list feels too parsimonious). I am grateful for the great times we shared in Waterloo.

And of course thank you Zhong, Sanha and Alex for keeping in touch from the other side of the world; Abhinav for keeping me sane during COVID; Ali, Batia, LV and Miya for making home such a happy place to come back to; and to Antonia for the support in the last tough few months.

Et, bien sûr, maman, pour absolument tout.

Table of Contents

Examining Committee ii

Author's Declaration iii

Statement of Contributions iv

Abstract v

Acknowledgements vii

List of Figures xii

List of Tables xiv

List of Abbreviations xv

1 Introduction 1

1.1 Gravitational waves and gravity 2

1.1.1 Gravitational Waves as ripples in spacetime 2

1.1.2 The Einstein Field Equations 4

1.1.3 Gravitational Waves: propagation 5

1.1.4 Effect of passing GWs on particles 6

1.1.5 GW: sourcing 12

1.1.6 GW sources . . . 13
1.2 Gravitational wave detection . . . 14
1.2.1 Road to GW detection . . . 14
1.2.2 The Current state of GW science . . . 16
1.2.3 Future detectors . . . 18

2 GW data analysis and SCoRe framework 21
2.1 Gravitational waves analysis . . . 21
2.1.1 Detector noise . . . 21
2.1.2 Match filtering . . . 23
2.1.3 Parameter estimation . . . 24
2.1.4 GW templates . . . 26
2.2 Testing the standard model of GWs . . . 28
2.3 SCoRe framework overview . . . 29
2.3.1 Motivation . . . 29
2.3.2 Description . . . 30
2.3.3 Implementation . . . 31
2.4 SCoRe formalism . . . 34
2.4.1 Cross-correlation of the residual signal . . . 35
2.4.2 Choice of residual Templates . . . 37
2.4.3 Projection on a template . . . 39
2.4.4 Inference using the Bayesian framework . . . 41

3 Demonstrating the SCoRe method 45
3.1 Application of SCoRe on a toy example for an unmodeled search . . . 45
3.1.1 Generating mock data . . . 45
3.1.2 Choice of τ . . . 48
3.1.3 Bayesian inference of the injected signal . . . 52

3.2 Application of SCoRe on a beyond GR model . . . 55
3.2.1 Toy model EFT and numerical set-up . . . 55
3.2.2 Choice of template . . . 56
3.2.3 Recovery of injected signal . . . 58
3.3 Discussion . . . 60

4 SCoRe forecast for 3G **62**
4.1 GW source population . . . 63
4.1.1 Redshift evolution . . . 64
4.1.2 Mass spectrum . . . 65
4.1.3 Spin distribution . . . 68
4.2 CRPS model . . . 68
4.2.1 BM waveform model . . . 68
4.2.2 BM source dependence model . . . 69
4.2.3 CRPS computation . . . 70
4.2.4 Fisher Matrix Estimation . . . 71
4.3 Forecast results . . . 72
4.3.1 Cross-correlated power scaling . . . 73
4.3.2 BM signature detection . . . 73
4.4 Discussion . . . 74

5 Challenges in solving Effective Fields of Gravity **79**
5.1 Einstein-scalar-Gauss-Bonnet theory as an EFT of gravity . . . 80
5.2 Well posedness and the *fixing-the-equations* procedure . . . 83
5.3 Fixing scheme for EsGB gravity . . . 88
5.4 Applying the fixing scheme to BHS . . . 90
5.5 Fixing equations and constraints . . . 92
5.6 Discussion . . . 96

Conclusion and future outlook **98**

References **102**

APPENDICES **124**

A Appendix for Chapter 3 **125**

A.1 Modeling residual strain 125

A.2 False Alarm Rate 126

List of Figures

1.1 Gravitational wave polarisations 11
1.2 Representative amplitude spectral density of the LIGO and Virgo detectors 17
1.3 Illustration of the detectable volume of the current and future GW detectors 19

2.1 Outline of the SCoRe method. 34
2.2 Hierarchical Bayesian model. 43

3.1 Eample toy model data 47
3.2 Example cross-correlation data 49
3.3 Effect of τ on the template 50
3.4 Effect of τ on mean power 51
3.5 Posterior on $\tilde{\alpha}_1$ 53
3.6 Bayes factor in favor of BM hypothesis 54
3.7 Residual power and template functions for EFT toy model. 57
3.8 Injected and recovered values of $\tilde{\alpha}_1$ for EFT toy model. 61

4.1 Samples from the redshift model. 66
4.2 Samples from the mass model. 76
4.3 Cross-correlated power scaling. 78
4.4 SCoRe constraints on 3G catalog. 78

5.1 Well- and ill-posedness in the parameter space of possible theories and initial conditions. 86

5.2 Scalar charge for a single BH undergoing scalarization. 92
5.3 Waveform for a head-on collision of two BHs. 93
5.4 Waveform for a BBH inspiral. 94
5.5 Constraint violation for different resolutions 97
5.6 Constraint violation for different κ 97

A.1 False alarm rate for Gaussian distribution 126
A.2 False Alarm Rate scaling with signal and number of events 127

List of Tables

3.1 Projection coefficients of the injected BM signal. 59

4.1 Models and population parameters for the source parameters. 64

List of Abbreviations

BBH Binary Black Hole v, 13, 16, 18–20, 26, 28, 45, 47, 54, 56, 62, 63, 65, 66, 69, 74, 79, 83, 99, 101

BH Black Hole v, 1, 13–16, 18, 28, 42, 43, 55, 56, 64, 66, 67, 76, 81, 82, 90–94, 98

BM Beyond Modeled 28–32, 34, 35, 37, 38, 40–49, 51, 52, 54–56, 58–60, 62, 65, 68–75, 79, 99–101

BNS Binary Neutron Star 13, 15, 16, 19, 20, 28

CBC Compact Binary Coalescence 13, 14, 16, 22, 24, 26, 27, 81, 84

CE Cosmic Explorer 18, 20, 62, 69, 72, 100

CRPS Correlated Residual Power Spectrum v, 30–32, 34, 36–40, 44, 46, 48, 49, 52, 53, 70, 74, 75, 100

EEP Einstein Equivalence Principle 3, 4, 6

EFE Einstein Field Equations 4–6, 12–14

EFT Effective Field Theory v, vi, 4, 5, 41, 43, 55–60, 69, 74, 79–81, 83–85, 87, 88, 90, 91, 98–100

ESGB Einstein Scalar-Gauss-Bonnet 82–84, 88–92, 98, 101

ET Einstein Telescope 18, 20, 100

FAR False Alarm Rate 59, 126, 127

FNC Fermi Normal Coordinates 6, 7, 9

GR General Relativity v, 1–4, 6, 10–15, 18, 27–32, 45, 55–58, 62, 63, 69, 70, 79–82, 89, 91, 92, 94, 98, 101

GW Gravitational Wave v, 1–8, 10–16, 18, 21–24, 26–32, 34–38, 40–44, 46, 62–65, 71, 72, 79, 80, 82, 84, 96, 98, 99, 101

IGWN International Gravitational-Wave Network 15, 16

LIGO Laser Interferometer Gravitational-Wave Observatory 15, 16, 18

LVK LIGO-Virgo-KAGRA 24, 28, 29, 63, 101

MGH Modified Generalized Harmonic 82, 83, 89

MLE Maximum Likelihood Estimator 25–27, 35, 59, 68, 71, 72

NP Newman-Penrose 8–11

NR Numerical Relativity 32, 56, 58–60, 69

NS Neutron Star v, 13–15, 18

NSBH Neutron Star-Black Hole 13, 28

PISN Pair-Instability Supernova 66, 76

PN Post-Newtonian 12, 18, 27–29, 82, 100, 101

PPSN Pulsational Pair-Instability Supernova 66, 67, 76

PSD Power Spectral Density 23, 40, 60, 69, 70

SM Standard Model v, 2, 14, 18, 28–32, 34, 37, 41, 43–46, 52, 54, 59, 68, 74, 79, 80, 96, 99, 101

SNR Signal-to-Noise Ratio 19, 20, 23–25, 34, 36, 40–42, 48, 52, 53, 58, 59, 63, 71, 72, 74

Chapter 1

Introduction

Gravitational Waves (GWs) are a centrepiece of modern astrophysics and their measurement ushered in a second golden age of gravity research. Their importance lies in their ability to offer information that complements electromagnetic observations. They probe regions of spacetime that are void of (cleanly visible/interpretable) electromagnetic radiation, and since they interact with matter with a strength orders of magnitude weaker than electromagnetic waves, they are not distorted by the matter they traverse. In addition, the most powerful GWs are emitted in the regions of spacetime where gravity is strong, by phenomena involving acceleration at relativistic regimes. This last feature makes them a unique probe of strong gravitational phenomena, which are not directly accessible by electromagnetic observations.

Our most successful theory to describe these phenomena is General Relativity (GR). It has passed all our tests (see, for example, chapters 7–9 of [234]). However, these tests were all limited to the regimes of weak gravity and non-relativistic velocities (and of low relativistic velocities, strong gravity in the case of binary pulsars). Despite its success, there is consensus that GR is an incomplete description of gravity. This is because it is a classical theory, and we expect the full theory of gravity to be quantum, just like the Standard Model of particle physics, which describes the other fundamental forces of nature. Even classically, GR has limits to its predictive power. Solutions to the Einstein equations admit singularities—points where physically meaningful quantities, such as the force felt by a particle, become infinite. A quantum theory of gravity is expected to resolve these singularities and other issues that arise in the predictions of GR, such as the Black Hole (BH) information loss [217] and the cosmological constant problems [179]. Theoretical considerations make the new regime of extreme conditions probed by GWs an exciting candidate to reveal departures from GR.

Disentangling any departure from noise or inaccuracies in our understanding of known physics, such as GR or the astrophysics of the sources, is an essential challenge to surmount. It will become vital in future GW detectors, where higher sensitivity will increase the importance of systematic errors. In this thesis, I will describe a method to search for unmodeled physics, including deviations from GR, with this challenge in mind.

In this introduction, I present the ingredients that make up our Standard Model (SM) of GWs. They include the theory of GR, which describes their origin and behavior, and the types of sources that emit them. They also include how the noise in the detectors is modelled and how the signal is extracted from the data, which I summarize in Chapter 2. In Chapter 2, I also describe the current tests of GR with GWs, and the present and future GW detectors. This leads to the presentation of the `SCoRe` framework, which aims to provide a model-independent search for deviations from the SM using the cross-correlation of the GW signal in pairs of detectors and the dependence of the deviation on the parameters of the signal. In Chapter 3, I illustrate how to apply the `SCoRe` framework to search for deviations from the SM in GW data. In Chapter 4, I focus on how the technique can be applied to future GW detectors, and what constraints can be placed on deviations from the SM. Finally, in Chapter 5, I give an overview of some of the challenges faced when modelling GWs in an alternative theory to GR. I focus on the part of the work in [57] that I contributed to.

1.1 Gravitational waves and gravity

GWs were predicted by Einstein soon after the publication of GR [87]. In this section, I describe how GWs arise in GR, and how they may differ in other theories of gravity.

1.1.1 Gravitational Waves as ripples in spacetime

At the core of GR is the principle of relativity. In Newtonian mechanics, the principle of relativity takes the form of the equivalence between a family of coordinates, called *inertial coordinates*, which are related by Galilean transformations. These transformations include translations in space and time, and rotations. Stated differently, the laws of physics are the same for observers with different but constant velocities.

In the 19th century, Maxwell's equations, describing electromagnetism, seemed to contradict the principle of relativity. They seemed to imply that the speed of light should be

the same in all inertial coordinates, which was not compatible with Galilean transformations. Efforts to reconcile electromagnetism with the principle of relativity by measuring a change in the speed of light due to the motion of the observer failed. Einstein resolved the issue by taking the constancy of the speed of light as a postulate, and derived the transformations under which Maxwell's equations are invariant—the Lorentz transformations. He then proposed that all laws of physics, not just electromagnetism, should be be invariant under Lorentz rather than Galilean transformations. This is the basis of special relativity. Lorentz transformations famously mix space and time in conspiring to keep the speed of light constant, leading to the concept of spacetime.

Motivated by the ideas of Ernst Mach, Einstein attempted to extend the principle that the laws of physics should be the same in all inertial coordinates to also being the same in non-inertial coordinates—those that are accelerating with respect to inertial coordinates. This can be achieved by requiring the laws of physics to be invariant under general coordinate transformations rather than just Lorentz transformations. Geometry provides a natural framework to handle arbitrary coordinate transformations. Notably, the rules defining the transformations between coordinates are described by geometric objects, one of which is the metric field, which quantifies the "shape" of spacetime.

The connection to gravity comes with "the happiest thought" of Einstein's life—the realization that gravitational acceleration is indistinguishable from acceleration observed due to a non-inertial coordinate system. In modern language, this is the weak equivalence principle, which states that the trajectory of a free-falling particle is independent of its internal structure and composition. This was later generalised to the Einstein Equivalence Principle (EEP), which, in addition to the weak equivalence principle, also states that special relativity is valid locally and that the outcome of non-gravitational experiments are independent of time and location. The principle points to gravity being an effect of non-inertial coordinates, and therefore the identification of the gravitational field with the metric field, which transforms between coordinates.

The concept of spacetime represented by a metric is not unique to GR. A theory that satisfies the EEP is a metric theory of gravity, where gravity is an inherent property of spacetime described by a metric field (possibly more than one), and where free-falling particles follow the geodesics of this metric (see section 2.3 of [234]). In this type of theory, the metric is the only field describing gravity that interacts with matter, although its dynamics can be mediated by other gravitational fields. GWs can be understood as ripples in the metric field. The details of the theory will affect the properties of the GWs, notably how they are generated, how they propagate, and how they affect the motion of the matter they traverse.

In this section, I will describe GWs in GR, highlighting the places where other theories of gravity can lead to different predictions.

1.1.2 The Einstein Field Equations

The EEP states that the motion of particles affected by gravity is the result of the geometry of spacetime. The formation and behaviour of GWs is a result of the dynamics of this spacetime, which in GR are described by the Einstein-Hilbert action:

$$S = \frac{1}{16\pi G}\int d^4x\sqrt{-g}R + \int d^4x\sqrt{-g}\mathcal{L}_{\text{matter}}, \tag{1.1}$$

where g is the determinant of the metric field g_{ab}, G is the gravitational constant, and $\mathcal{L}_{\text{matter}}$ is the Lagrangian describing the matter content. The Ricci scalar $R = g^{ab}R_{ab} = g^{ab}R^{c}{}_{acb}$ is a scalar constructed from the Riemann tensor, which describes the curvature of spacetime and is itself constructed from the metric and its derivatives:

$$R^{a}{}_{bcd} = \partial_c\Gamma^a_{bd} - \partial_d\Gamma^a_{bc} + \Gamma^a_{ce}\Gamma^e_{bd} - \Gamma^a_{de}\Gamma^e_{bc}, \tag{1.2}$$

$$\Gamma^a_{bc} = \frac{1}{2}g^{ad}\left(\partial_b g_{cd} + \partial_c g_{bd} - \partial_d g_{bc}\right), \tag{1.3}$$

where Γ^a_{bc} are the Christoffel symbols.

The dynamics of the metric field, and therefore of GWs, are obtained by varying the Einstein-Hilbert action with respect to the metric field to give the Einstein Field Equations (EFE):

$$G_{ab} = R_{ab} - \frac{1}{2}g_{ab}R = 8\pi G T_{ab}, \tag{1.4}$$

where T_{ab} is the stress-energy tensor which describes matter and energy distribution and G_{ab} is the Einstein tensor. Comparing with the definition of the Ricci tensor, we see that the EFE are second-order, quasi-linear equations for the metric field. In essence, the EFE means that "space tells matter how to move; matter tells spacetime how to curve" (in [161], attributed to Wheeler).

In the modern language of Effective Field Theories (EFTs), (1.1) is the leading order term in the EFT of gravity. In the EFT formalism, the full theory describing gravity at all energy scales is not assumed. At higher, non-observable energy scales, the full theory includes high-mass degrees of freedom that do not appear in the low energy limit. The effect of those high mass degrees of freedom on the low energy limit is captured by operators built out of the lower energy degrees of freedom (the metric field and its derivatives). The

operators are combined into terms of increasing energy dimension, which are suppressed by appropriate powers of the cut-off energy scale—the upper limit of energy relevant to observation. Schematically, the EFT lagrangian will be of the form: $\mathcal{L}_{\text{EFT}} = R + \frac{\mathcal{L}_n}{E_{\text{UV}}^{2-n}}$, where n is the energy dimension of the operator $\mathcal{L}_n$, and E_{UV} is the cut-off scale. These new terms modify the dynamics of the metric field, and, therefore, the GWs we see. We will discuss examples of higher-order terms in the next chapters.

1.1.3 Gravitational Waves: propagation

The EFE are non-linear and famously challenging to solve. However, we can gain insight into the behaviour of GWs by considering a simplified case: some small deformation in spacetime away from any matter source. In this weak field limit, we regard the metric as a perturbation h_{ab} from flat, Minkowski spacetime η_{ab}:

$$g_{ab} = \eta_{ab} + h_{ab}, \tag{1.5}$$

with $|h_{ab}| \ll 1$. To explore how h_{ab} evolves under the EFE, it is convenient to define the trace-reversed perturbation $\overline{h}_{ab} = h_{ab} - \frac{1}{2}\eta_{ab}h$. Substituting this into the EFE, [1] we obtain an evolution equation for $\overline{h}_{ab}$:

$$-\frac{1}{2}\partial^c\partial_c\bar{h}_{ab} + \partial^c\partial_{(a}\bar{h}_{b)c} - \frac{1}{2}\eta_{ab}\partial^c\partial^d\bar{h}_{cd} = 8\pi T_{ab}, \tag{1.6}$$

where we retained only terms linear in h_{ab}, which implies that we are ignoring the backreaction of the GWs on the metric—that the GWs themselves are not changing the spacetime they propagate through.

To show that this equation leads to waves propagating, we set the gauge condition $\partial_a\overline{h}^{ab} = 0$. This removes redundancies in the mathematical description of the metric field which are not physical degrees of freedom. In this gauge, the EFE take the form of a wave equation for $\overline{h}_{ab}$:

$$\Box\overline{h}_{ab} = -16\pi G T_{ab}. \tag{1.7}$$

Here, $\Box = \eta^{ab}\partial_a\partial_b$ is the d'Alembertian operator with respect to the flat metric. This equation implies the propagation of small perturbations in the metric at the speed of light—GWs.

GWs themselves contain energy, and, therefore, should also affect the evolution of the metric. We neglected this effect in linearising the EFE. However, a similar argument to

[1] The derivations in this section are standard; see, for example, chapter 1.1 of [153].

the one that led to (1.7) shows that even when the non-linear terms are included, the EFE still lead to a wave equation for GWs, this time with respect to the full metric g_{ab} and with a term on the right-hand side that accounts for the energy carried by the GWs. See chapter 6 of [185], for example.

In theories other than GR, the action (1.1), the EFE, and therefore the wave equation (1.7) can be modified, and the speed of GWs can differ from the speed of light. A standard example is massive gravity [68], where an additional term $-m^2\overline{h}_{ab}$ appears in (1.7). This results in a non-trivial dispersion relation and GWs propagating slower than the speed of light.

1.1.4 Effect of passing GWs on particles

In the last section, we described how GWs propagate through spacetime as ripples in the metric. But what is the effect of a GW? To answer this question, we consider a timelike geodesic γ with tangent vector u^a, as would be followed by a detector. Measurements made with the detector are most naturally described in the Fermi Normal Coordinates (FNC) built around this worldline. In these coordinates, the Christoffel symbols vanish, and the metric is flat on the worldline's tangent space. This is to say, the world appears locally flat in a small enough region around the detector (in accordance with the EEP). The time coordinate t is the proper time τ measured on the worldline, and the spatial coordinates ξ^i correspond to the proper distance, the actual length measured in the detector. The Latin indices from the middle of the alphabet, i, j, are the spatial indices in the FNC.

Consider a sphere of test particles around the worldline and at rest in the FNC. As the GW passes, the spacetime around the geodesics is distorted, which causes the geodesics to deviate from their original paths. Such a change in geodesics due to curvature is described by the geodesic deviation equation: [2]

$$u^d \nabla_d u^c \nabla_c \xi^a = R^a{}_{bcd} \frac{dx^b}{d\tau} \frac{dx^c}{d\tau} \xi^d. \tag{1.8}$$

In the FNC coordinates, the Christoffel symbols vanish on γ, so the left-hand side is simply the acceleration. In addition, the time coordinate is the proper time, so $\frac{dx^a}{d\tau} = (1, 0, 0, 0)$ and the equation becomes

$$\frac{d^2\xi_i}{dt^2} = R_{i00j}(t)\xi^j(t), \tag{1.9}$$

[2] See, for example, 3.3 of [223] for a derivation.

where 0 is the time index in the FNC coordinates. Note that the indices in these coordinates are raised and lowered with the flat metric, so $\xi^i = \delta^{ij}\xi_j$, for example. The components R_{i00j} are evaluated along the worldline, and are a measure of the tidal forces acting on the detector. They are sometimes referred to as the "electric" part of the Riemann tensor by analogy of Eq (1.9) with the acceleration of a charged particle in an electric field. In (1.9), we see that the effect of a GW on the test particles can be interpreted as a Newtonian force, with the observed force given by a suitable projection of the Riemann tensor onto the tangent vector of the geodesic.

Assume plane waves of the form $R_{i00j} = H_{ij}e^{i\omega t}$. The condition $|h_{ab}| \ll 1$ implies $|H_{ij}| \ll 1$. We can solve the equations to zeroth order ($\xi_i(t) = \xi_i(t=0)$) and substitute the solution to get

$$\frac{d^2\xi_i}{dt^2} = H_{ij}e^{i\omega t}\xi^j(0), \tag{1.10}$$

$$\xi_i\left(t\right) = \xi_i\left(0\right)\left(1 - \frac{1}{\omega^2}H_{ij}e^{i\omega t}\right). \tag{1.11}$$

The GW causes the test particles to oscillate around their initial positions.

The assumption that we have a metric theory of gravity restricts the components of R_{i00j} and the modes of oscillation of the test particles. From the discussion above, GWs are null—they travel at the speed of light—and their effect is contained by the Riemann tensor, which is linearized around the flat metric.[3]

To carry out the analysis of the Riemann tensor associated with the wave, it is convenient to use a null coordinate system, since the wave itself is null. We first describe the construction of such a coordinate system, and then apply it to the study of a GW. We factor the metric into a flat metric η and tetrad vectors e_a^α:

$$g_{ab} = \eta_{\alpha\beta}e_a^\alpha e_b^\beta, \quad \eta_{\alpha\beta} = \begin{pmatrix} 0 & -1 & 0 & 0 \\ -1 & 0 & 0 & 0 \\ 0 & 0 & 0 & 1 \\ 0 & 0 & 1 & 0 \end{pmatrix}, \tag{1.12}$$

where Roman indices label the original coordinates (we will later use the FNC), and the Greek indices label the null coordinates. We cannot have a complete basis of independent real null vectors—it is not possible to find 2 pairs of linearly independent vectors that are

[3]The derivation that follows can be carried out for a nearly null wave to the same results. See section 11.4.1 of [234].

both null and orthogonal to each other. To build our basis, we must allow two vectors to be complex. As the metric is real, these two vectors must be complex conjugates of each other. To satisfy these conditions, we choose a set of null tetrad vectors l^a, n^a, m^a, $\bar{m}^a$, where the $\bar{}$ denotes complex conjugation. This basis is chosen such that the following relations hold:

$$l^a l_a = n^a n_a = m^a m_a = \bar{m}^a \bar{m}_a = 0, \tag{1.13}$$

$$l^a m_a = l^a \bar{m}_a = n^a m_a = n^a \bar{m}_a = 0, \tag{1.14}$$

$$l^a n_a = -m^a \bar{m}_a = 1, \tag{1.15}$$

where the first two lines are the conditions that the vectors be null and orthogonal, while the last condition is a normalization condition. This is the basis system of the *Newman-Penrose (NP) formalism* [164].

Applying this basis to the study of a null GW, we choose the vector l such that it is tangent to the wavefronts. Defining the retarded time $u = t - \xi^3$, where ξ^3 is the spatial coordinate in the direction of propagation of the wave. The retarded time defines a line along which the wave propagates. By definition, we have:

$$l_a = u_{,a}, \tag{1.16}$$

where the comma denotes a partial derivative.

We can now obtain the electric part of the Riemann tensor in 3 steps. First, we use the key assumption that the Riemann tensor associated with the GW can only depend on the retarded time. This means that we can write derivatives of the Riemann tensor with respect to any coordinate as [79]:

$$R_{abcd,e} = -l_e \frac{d}{du} R_{abcd}. \tag{1.17}$$

Taking the derivative with respect to the other null coordinates, substituting the above equation and using the relations (1.13), we find that the derivative of the Riemann tensor with respect to the null coordinates is zero except with respect to n:

$$R_{abcd,m} = R_{abcd,\overline{m}} = R_{abcd,l} = 0, \tag{1.18}$$

$$R_{abcd,n} = \frac{d}{du} R_{abcd}, \tag{1.19}$$

where we define, for a tensor T, $T_{lnm\overline{m}} = T_{abcd} l^a n^b m^c \bar{m}^d$.

As a second step, we start with the Bianchi identity, which gives

$$R_{\alpha\beta[\delta\epsilon,\zeta]} = 0, \tag{1.20}$$

where the square brackets denote antisymmetrization. The derivatives are partial derivatives rather than covariant derivatives, as we are working with the linearised Riemann tensor. The Riemann terms vanish when the derivative is not taken with respect to n. Therefore, we have $R_{\alpha\beta\lambda\mu,n} = 0$ for λ, μ not equal to n. This means that there are only six non-zero independent components of the Riemann tensor: those of the form $R_{n\alpha n\beta}$. Expressing these components in the notation of the NP scalars, they are

$$\Psi_2 = -\frac{1}{6}R_{nlnl}, \tag{1.21}$$

$$\Psi_3 = -\frac{1}{2}R_{nln\overline{m}} = \overline{R_{nlnm}}, \tag{1.22}$$

$$\Psi_4 = -R_{n\overline{m}n\overline{m}} = \overline{R_{nmnm}}, \tag{1.23}$$

$$\Phi_{22} = -R_{nmn\overline{m}}, \tag{1.24}$$

where Ψ_2 and Φ_{22} are real, and Ψ_3 and Ψ_4 are complex scalars. The Ψ terms are three of the five complex Weyl NP scalars, the independent components of the Weyl tensor—the part of the Riemann tensor which describes tidal deformations that preserve volume. The Φ terms are part of the 10 components of the Ricci tensor, which describes the other part of the Riemann tensor.

Finally, we go back to the FNC, and explicitly construct the NP tetrads with the (t, ξ^1, ξ^2, ξ^3) coordinates as:

$$l^a = (1,0,0,1)\,, \quad n^a = \frac{1}{2}(1,0,0,-1)\,, \quad m^a = \frac{1}{\sqrt{2}}(0,1,i,0)\,, \quad \bar{m}^a = \frac{1}{\sqrt{2}}(0,1,-i,0)\,. \tag{1.25}$$

Then, transforming the NP quantities from the null tetrad to the FNC, we have

$$\Psi_2 = \frac{1}{6}R_{3003}, \tag{1.26}$$

$$\Psi_3 = \frac{1}{2\sqrt{2}}R_{1003} - \frac{i}{1\sqrt{2}}R_{2003}, \tag{1.27}$$

$$\Psi_4 = \frac{1}{2}R_{1001} - \frac{1}{2}R_{2002} - iR_{1002}, \tag{1.28}$$

$$\Phi_{22} = \frac{1}{2}R_{1001} + \frac{1}{2}R_{2002}. \tag{1.29}$$

And, solving for R_{i00j}, we have

$$R_{i00j} = \begin{pmatrix} \Phi_{22} + \mathrm{Re}\Psi_4 & -\mathrm{Im}\Psi_4 & 2\sqrt{2}\mathrm{Re}\Psi_3 \\ -\mathrm{Im}\Psi_4 & \Phi_{22} - \mathrm{Re}\Psi_4 & -2\sqrt{2}\mathrm{Im}\Psi_3 \\ 2\sqrt{2}\mathrm{Re}\Psi_3 & -2\sqrt{2}\mathrm{Im}\Psi_3 & 6\Psi_2 \end{pmatrix}, \tag{1.30}$$

where we have arranged the components in a matrix with the x, y, and z directions in the rows and columns.

The oscillation occurs in multiple directions. This is illustrated in Fig 1.1, where the effect of the different modes on a sphere of test particles is shown. Each of the figures shows the effect of one of the possible NP quantities. The solid and dashed lines represent the particles at two different times. To summarise:

- when only Φ_{22} is present, the particles oscillate in phase in the x and y directions. This is the "breathing mode";
- when only $\mathrm{Im}\Psi_4$ is present, the particles oscillate out of phase at 45 degrees to the x and y axes. This is the "cross" or $\times$ polarisation;
- a non-zero $\mathrm{Im}\Psi_3$ is similar, but at 45 degrees between the y and z axes;
- a non-zero $\mathrm{Re}\Psi_3$ is the same again, in the x and z plane;
- a non-zero $\mathrm{Re}\Psi_4$ is out of phase in the x and y plane. This is the "plus" or $+$ polarisation; and
- Ψ_2 describes the squeezing and stretching of the sphere in the z direction only, and is the "longitudinal" mode.

This description of the effect of GWs is apt when the wavelength of the GW is much larger than the size of the system, which is the case for the GWs detected by ground-based interferometers.

Which of the components of R_{i00j} are free to be sourced and to propagate will depend on the dynamics of the theory. In GR, only Ψ_4 is unconstrained, and only the plus and cross polarizations are physical. Theories with other dynamics than GR can predict different polarizations. We will mention the constraints placed on them in 2.2.

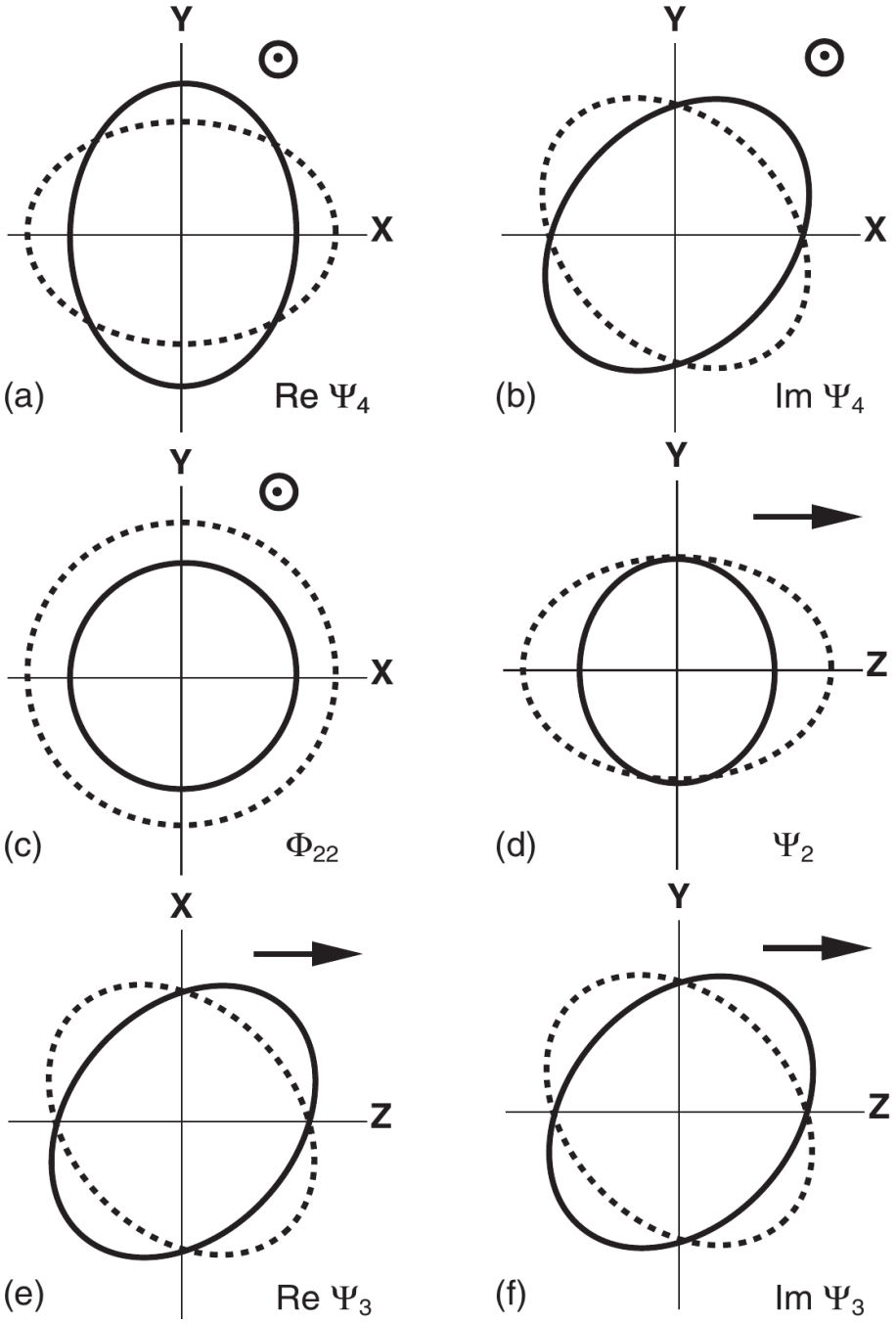


Figure 1.1: The effect of the different NP quantities Ψ_4, Φ_{22}, Ψ_2 and Ψ_3 on a sphere of test particles. The solid and dashed lines represent the particles at different times. The direction of propagation of the GW is shown by an arrow (two circles indicate the arrow pointing out of the page). GWs will cause test particles to oscillate in various patterns depending on the modes or polarizations present. The + and × polarisations corresponding to Ψ_4, on the top row, are the only physical polarisations in GR. Figure 11.1 in [234].

1.1.5 GW: sourcing

We have seen how GWs propagate through spacetime and the measurable effect they can have. We now turn to how they are produced. As the full derivation of the important expressions of this section is not covered here, the reader is referred to Section 3.3 of [153] for an example of the details. The right-hand side of the wave equation (1.7) describes how matter and energy distribution sources the GWs. The equation can be solved using retarded Green's functions, giving the general solution:

$$\bar{h}_{ab}(x) = -\frac{16\pi G}{c^4}\int d^4x' G(x-x')T_{ab}(x'), \tag{1.31}$$

where $G(x-x')$ is the retarded Green's function, which describes how the disturbance due to the source at x' propagates to x. The coordinates x are the coordinates of flat spacetime up to Lorentz transformations. As a simple case, which can be solved analytically, we consider the regime where the source (T_{ab}) is changing non-relativistically, and is far from where the GW is being measured. In that case, the most significant contribution to the GW is

$$\overline{h}_{ij} = \frac{2}{r}\frac{G}{c^4}\ddot{Q}_{ij}\left(t-\frac{r}{c}\right), \tag{1.32}$$

$$Q^{ij} := \int d^3x\rho(t,\mathbf{x})\left(x^i x^j - \frac{1}{3}x^2\delta^{ij}\right), \tag{1.33}$$

where r is the distance to the source, ρ is the mass density of the source, i,j are the spatial indices, and the dot denotes a derivative with respect to the time coordinate. The quadrupole moment of the source, Q_{ij}, is a measure of a particular type of asymmetry in the mass distribution of the source.

Computing the first-order contributions of the perturbation h_{ab} to the EFE, which we previously neglected, we can find the energy loss associated with the GW:

$$\dot{E} = -\frac{G}{5c^5}\left(\dddot{Q}_{ij}\right)^2. \tag{1.34}$$

Equations (1.32) and (1.34) are referred to as the quadrupole formulae.

Higher corrections to the quadrupole formulae are often labelled by the order of the characteristic speed squared $\left(\frac{v}{c}\right)^2$ of the system (the Post-Newtonian (PN) order). The fact that the quadrupole moment is the lowest multipole moment sourcing GWs (as opposed to the monopole or dipole moments) generalizes to the full theory and to relativistic settings in GR (see, for example, [185]). As we will mention in Sec. 2.2, alternative theories of gravity can predict changes to the quadrupole formulae, which can be expressed in terms of the PN order.

1.1.6 GW sources

The quadrupole formulae (1.32) and (1.34) hint at the most significant sources of GWs. They show that the amplitude of GWs is proportional to the second time derivative of the quadrupole moment of the source. This suggests that the loudest sources of GWs are asymmetrical systems under acceleration. Using dimensional analysis, if the system is composed of orbiting objects, the timescale of their orbit, and thus of the change in the quadrupole moment, scales as $\sim \sqrt{\frac{R^3}{GM}}$, where R is the size of the system and M its total mass. Then, the energy loss in (1.34) scales as $\sim \frac{G^4}{c^5}\left(\frac{M}{R}\right)^5$. This means that the brightest sources of GWs are systems with high compactness (the ratio of mass to size). A high compactness implies high gravitational fields—the figure of merit for when GR effects become important is GM/c^2R, and we say that gravity is strong when this is of order unity, as near the surface of a Neutron Star (NS) or the event horizon of a BH. The latter are solutions to the EFE without matter. Indeed, they are the most compact astrophysical objects.

These objects can orbit each other, in pairs of two BHs (Binary Black Hole (BBH)), two NS (Binary Neutron Star (BNS)), or a BH and a NS (Neutron Star-Black Hole (NSBH)), collectively referred to as Compact Binary Coalescences (CBCs). As they orbit each other, the objects have a time-varying quadrupole moment, which causes their orbital energy to be emitted as GWs. After an initial *inspiral* phase, where the objects spiral towards each other at low relativistic speeds, the objects undergo *merger*, in a highly non-linear, strong gravity regime. The merger is followed by a *ringdown* phase, where the remnant object (usually a BH) settles into a stationary state, emitting GWs with characteristic frequencies and damping times.

Since they are the prime emitters of GWs, it is essential to understand the parameters that describe these objects. BHs are simple and can be encapsulated by a single class of solutions—the Kerr metric [124], which describes a rotating BH with no charge. The Kerr metric has only two parameters: the mass and the angular momentum/spin of the BH. This simplicity is the result of a succession of theorems. First, the Penrose geodesic incompleteness theorem [180] states that, in likely physical conditions, found notably in gravitational collapse, a singularity will form.[4] Second, the Cosmic Censorship Conjecture [181] states that the singularity must be shielded from the rest of the universe by an event horizon.[5] Third, an important series of uniqueness theorems [48, 194] shows that the

[4]To be precise, assuming the null energy condition, the existence of a trapped surface, and the global hyperbolicity of the spacetime, at least one null geodesic will be incomplete.

[5]Given a geodesically complete initial Cauchy surface, the maximal development of this surface is

Kerr metric is the generic solution to the EFE with an event horizon.[6] The first theorem implies that singularities are likely generic endpoints in the collapse of massive objects. The second means that this singularity will be hidden behind an event horizon. The third implies that the Kerr metric will describe this event horizon.

Unlike BHs, NS contain matter in the form of layers of atoms, nuclei, and degenerate neutrons. While their structure is more complex than that of BHs, the effects of this structure only becomes important in the final stages of the inspiral, when the separation between the objects is comparable to the size of the NS. The stars are deformed by tidal forces, inducing a quadrupole moment, which increases the energy loss to GWs [66, 63, 94].

The SM of GWs assumes the CBC emitting the GWs we detect are either BHs or NS. It is possible that other sources of GWs exist, such as exotic compact objects [155, 145, 100, 67], which could emit GWs with similar waveforms to BHs.

1.2 Gravitational wave detection

1.2.1 Road to GW detection

In the framework of GR, the idea of GWs appeared soon after Einstein published GR in 1915-18 [87, 88]. Yet, it remained unclear whether these waves were real or just an artifact of a choice of coordinates that could be transformed away.

It was in the late 1950s, at the start of the first golden age of general relativity, that it became more widely accepted that GWs were real. Arguments such as the one we presented in Sec. 1.1 were used by Pirani [183] to show that GWs would produce an effect akin to Newtonian tidal forces, which was, in theory, measurable. In the Gedanken experiment, one would put a spring in between the free-falling test masses, and the geodesic deviation engendered by the passing wave would transfer energy to the spring. This energy is detectable and, thus, physical. This concept inspired the design of the first GW detectors, envisioned by Joseph Weber—founder of the field of gravitational wave astronomy—in the 1960s. Weber's detectors were 2m long, thin cylinders of aluminum tuned to resonate at a particular frequency that would convert the energy of a passing GW into a detectable

inextendible.

[6] Specifically, any stationary, axisymmetric, asymptotically flat solution of the EFE, regular on and outside a connected event horizon, is isometric to the Kerr-Newman metric. This latter metric describes a rotating BH with an electric charge. However, we expect astrophysical BHs to be electrically neutral, so we assume that charge is zero.

electrical signal. The range of frequencies and sensitivity level of the bars were insufficient to detect gravitational waves. The results Weber obtained [224, 225, 226] were controversial at the time and could not be reproduced by other groups.

In parallel, Rainer Weiss thought that the amplitude of GWs could be measured directly. Likely due to his familiarity with the developing field of laser physics, Weiss conceived the design [229] for a Michelson interferometer that would use the phase shift of a laser to measure the length change in the arms of the interferometer during the passage of a GW. The core design of the current International Gravitational-Wave Network (IGWN) detectors is still the same.

But where would these waves come from?

Eddington first applied the quadrupole formula to binary stars in 1922 [84], but the primary source candidate during Weber's experiments were anisotropies in supernovae. Starting around the time of Weber's experiments, NS and BHs became the subject of serious astrophysical studies. As more compact objects with potentially higher quadrupole moment acceleration, they became the primary candidates for sources of gravitational waves. [7] In 1975, the first binary pulsar, PSR1913+16, was discovered [111]. This is a BNS system with one pulsar. By tracking the timing of the pulsar's pulses, it was possible to measure the orbital decay of the system, and this was found to be consistent with the loss of energy due to gravitational waves predicted by GR [209]. This discovery showed the existence of GWs and that astrophysical objects could emit them. It was crucial for spurring the development of the field, and to the funding of the Laser Interferometer Gravitational-Wave Observatory (LIGO) project.

How loud would the signals from these objects be? From energy conservation, the GW strain falls with distance r as $h \sim \frac{1}{r}$. From dimensional analysis of (1.32), h should depend on G, c, r, and E (the energy released in the GW). We must have:

$$h \sim \frac{G}{c^4}\frac{E}{r}. \tag{1.35}$$

Substituting $G \sim 1.3 \times 10^{21} \mathrm{m}^3 M_\odot^{-1} \mathrm{s}^{-2}$ and the value of c, and converting to Mega parsecs, we find

$$h \sim 10^{-19} \left(\frac{E}{M_\odot c^2}\right) \left(\frac{r}{\mathrm{Mpc}}\right)^{-1}. \tag{1.36}$$

[7] The first mention I can find of BNSs as possible sources of gravitational waves is in Dyson's [78], where he mentions them in the peculiar context of being creations and, therefore, signs of extraterrestrial intelligence. More possible formation channels have been proposed since then—see, for example, [92] for a review.

For an extra-galactic source, $r \geq 1$Mpc. Assuming a fraction of order $\mathcal{O}(10^{-1})$ of the initial total mass of the binary is emitted (from the efficiency limit imposed by the second law of BH mechanics), and a typical mass of a BBH $< 100M_{\odot}$, $E \lesssim M_{\odot}c^2$ and we find that the strain would not be expected to exceed 10^{-19}.

Since Weiss' paper, the effort has been in the identification of noise sources and the ways to mitigate them to reach below that level of sensitivity. Early GW interferometer prototypes were built in the 1970s. The LIGO and Virgo projects were proposed in the late 1980s, and a decade later, construction of the three detectors began.

The initial LIGO detectors were designed to measure a strain of 10^{-21} over a frequency ranging from 10Hz to 10kHz [222]. Seismic noise dominates and sets the lower frequency limit, while photon shot noise dominates at high frequencies. This goal was surpassed by Enhanced LIGO in 2009 (with a strain sensitivity of 10^{-22} [20]), and by Advanced LIGO in 2015 (with a strain sensitivity of 10^{-23} [56]).

GW interferometers respond to the amplitude of the wave (as opposed to its energy density). As a result, the detection horizon grows linearly with the sensitivity (increasing from 30Mpc to 200Mpc for BNS signals between Enhanced LIGO and Advanced LIGO). Compare this to energy flux measurements, for which the detection horizon only increases as the square root of the sensitivity.

1.2.2 The Current state of GW science

The first event was detected a few months after the start of the Advanced LIGO observation run, in September 2015 [10]. Further improvements to the sensitivity are still being made to this day. As part of the current Advanced LIGO upgrade, for example, the development of frequency-dependent squeezing injections [146] allowed the detectors to surpass the standard quantum limit. This latter improvement alone increased the sensitivity by a factor of 1.6. As of the writing of this thesis, the current IGWN network includes not only the LIGO detectors in Hanford, Washington and Livingston, Louisiana, and the Virgo detector in Santo Stefano a Macerata, Italy, but also the Kamioaka detector in Japan, with LIGO-India expected to join the network in the next decade [216]. Such a network of detectors is essential to increase the precision of the sky localization of the sources, and to improve the recovery of polarization information [93].

In its first three observing runs, the IGWN has detected on the order of 100 CBC events. As of the end of the first part of the fourth observation run (O4a), the IGWN has seen on the order of 100 more candidate signals. Below is a list of some of the key results extracted from this catalogue of events so far:

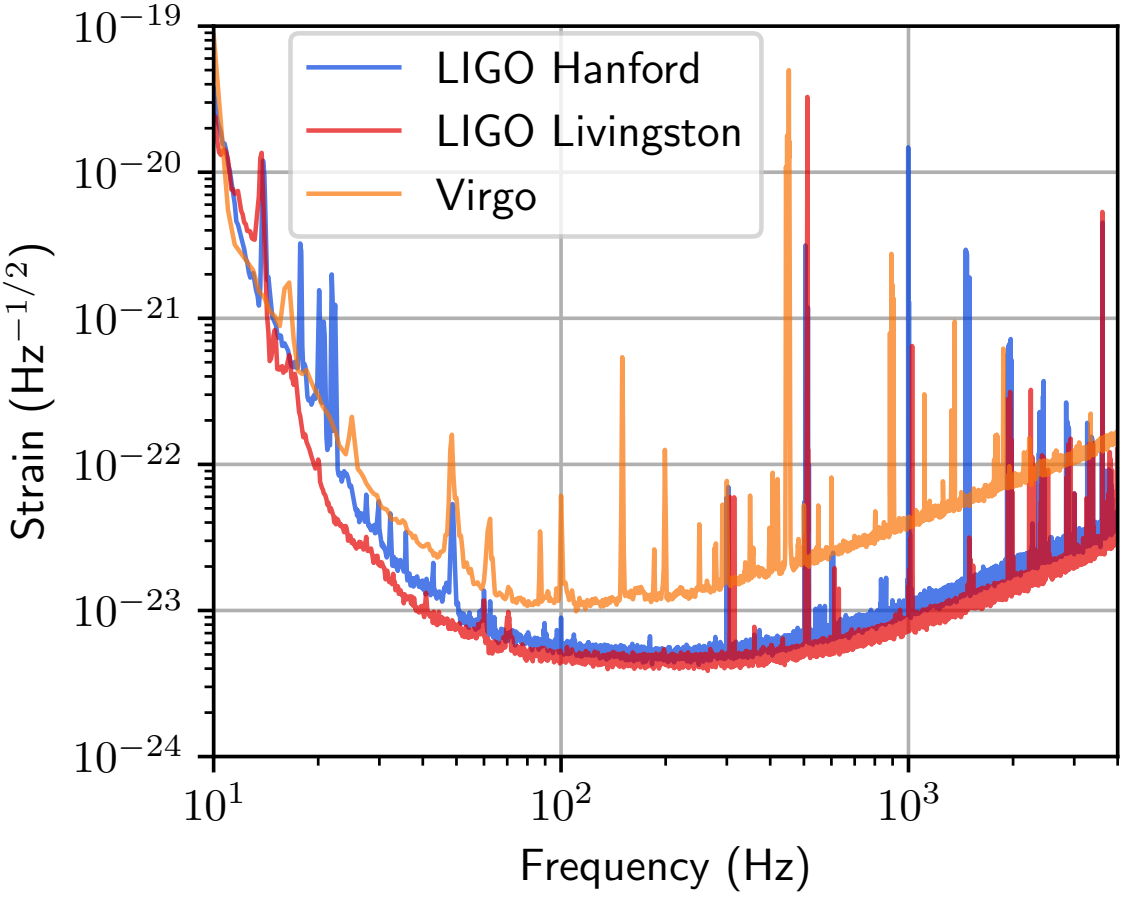


Figure 1.2: Representative amplitude spectral density of the LIGO and Virgo detectors during the O3a observing run (April 1, 2019 to March 27, 2020). Low frequency noise is dominated by seismic noise, while high frequency noise is dominated by photon shot noise. Fig. 6.10 in [22]

- GWs are real, and can be directly measured;
- objects consistent with BBHs merge within Hubble time;
- NS merge and are progenitors of short gamma-ray bursts and of kilonovae that produce r-process elements;
- BHs in binaries have masses ranging from several to hundreds of solar masses;
- an estimate for the Hubble constant can be obtained with electromagnetic counterparts, notably with GW170817 and its correlation with the Dark Energy Survey data [210, 212, 211]; and
- the detected signals so far are consistent with the SM of GWs, notably GR and BBHs being sources of GWs. For example, there is no strong evidence of polarization modes other than the standard + and × modes (the hypothesis of other modes being present is disfavoured by a factor of at least 2); and the combined measurement of the PN coefficients all contain their GR value within the 90% credible interval [24].

We will elaborate on the last item in section 2.2.

1.2.3 Future detectors

With the success of the current generation of detectors, new third-generation ("3G") detectors are planned for the next few decades. Cosmic Explorer (CE) [91] is a proposed set of US-based interferometers with the same design as the current LIGO detectors, but with 10 times the sensitivity. This increase in sensitivity is mainly due to the increase in the length of the arms of the interferometers (20–40km, compared to the 4km arms of the current LIGO detectors). The Einstein Telescope (ET) [4] is a proposed European detector with a triangular configuration of 10km arms with similar sensitivity to CE.

Closer term (2030s) plans for "2.5G" include the "A$^\sharp$" [102] and "Voyager" upgrade of the current LIGO detectors and the LISA mission, a space-based interferometer. The Voyager update aims to mitigate all major sources of noise to increase the sensitivity by a factor of 4–5 compared to the current Advanced LIGO detectors [90]. The LISA mission is a triangular configuration of three spacecrafts with an arm length of 2.5×10^6 km, which will be sensitive to lower frequencies [25] ($\sim 10^{-1}$Hz compared to the $\sim 10^2$Hz of the ground-based detectors).

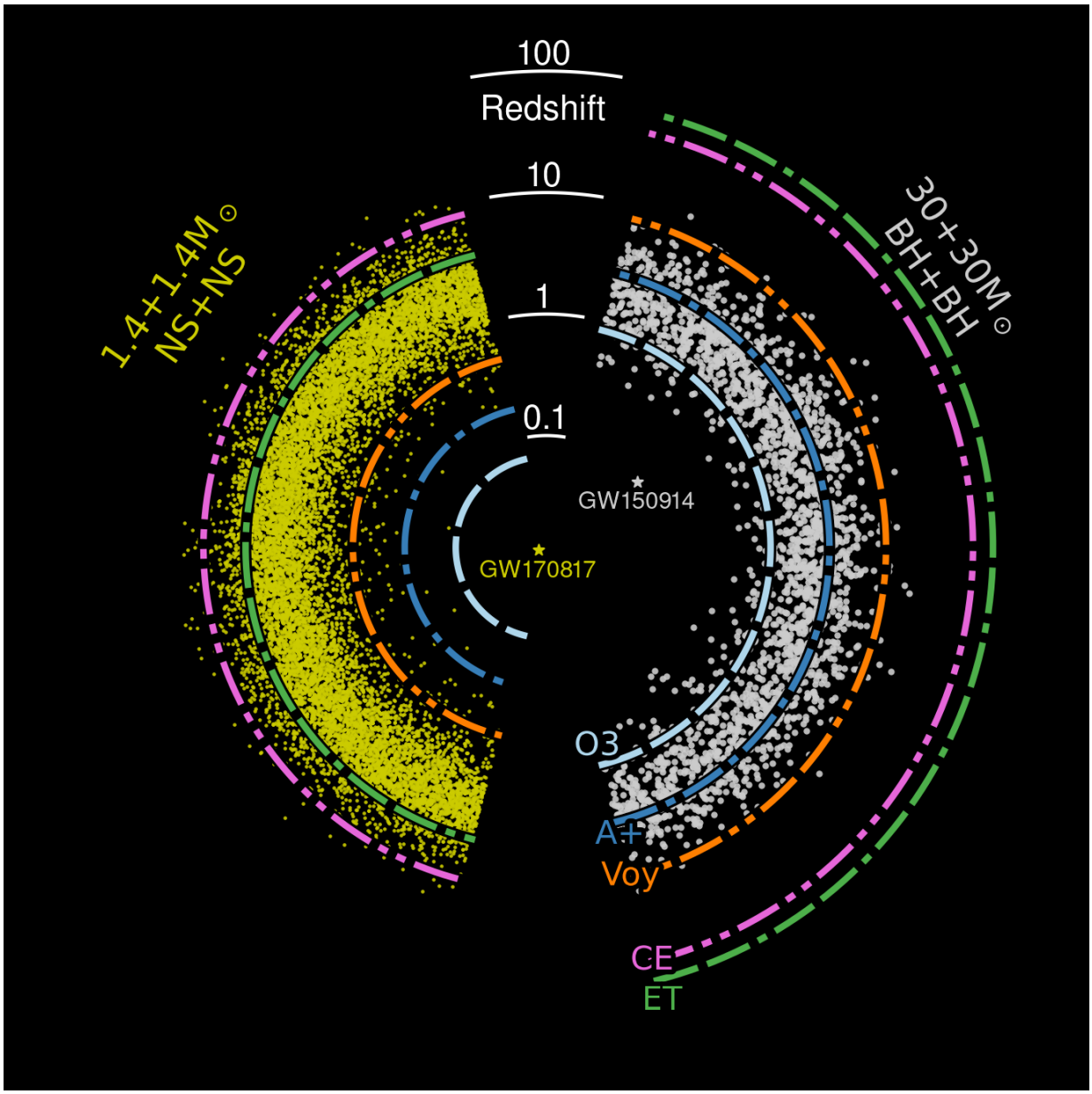


Figure 1.3: Illustration of the detectable volume of the current and future GW detectors. The lines represent the sensitivity to BBH and BNS mergers with masses similar to GW150914 and GW170817 (the lines represent the redshift at which such a merger will have an optimal SNR above 8). The dots represent a presumed distribution of events. Fig. 3.4 in [91]

The detectable volume for current and future ground-based detectors is represented by the lines in Fig. 1.3. This is the distance at which a source can be detected with an SNR (see Sec. 2.1.2) of 8. The sensitivity is to BBH and BNS mergers with masses similar to GW150914 and GW170817, respectively. The dots illustrate the presumed distribution of events, assuming the Madau-Dickinson redshift distribution. This distribution is proportional to observed star formation rates and is characterized by a rise in the star formation rate from the present day to a peak at redshift $z \approx 2$, followed by a power law decline at higher redshifts (see Sec. 4.1.1 for further details).

As a figure of merit, the ET and CE are forecast to detect events with maximum SNR on the order of $\mathcal{O}(10^3)$ and at rates in the order of $\mathcal{O}(10^5)\mathrm{yr}^{-1}$[152]. This is compared to the typical SNR or order $\mathcal{O}(10^1)$ for the order $\mathcal{O}(10^2)$ events detected so far. The prospect of new and more precise science with future detectors with this number of events and sensitivity is exciting. However, as greater sensitivity reduces statistical errors, it may reveal not only new unmodeled physics but also systematic errors in our model. With the increase in SNR given above, the accuracy of current waveform models would have to increase by 1–3 orders of magnitude for the effect of the systematic errors on parameter inference to be smaller than that due to statistical errors [186].

Chapter 2

GW data analysis and SCoRe framework

2.1 Gravitational waves analysis

In this section, we describe the fundamental tools of data analysis for ground-based GW detectors. We only cover the essentials needed for the rest of the thesis and refer to [153, 61, 120] for textbooks on which this section is based and where derivations can be found.

2.1.1 Detector noise

GW detectors measure a strain signal $d(t)$, the fractional change in length of the arms of the interferometer, a therefore dimensionless quantity. This signal is measured as a discrete time series with sampling rate of 4096 Hz or 16384 Hz. In our analysis, we assume that the data consists of a linear combination of the signal and noise:

$$d(t) = s(t) + n(t). \tag{2.1}$$

In practice, $n(t)$ is a time series—a set of real numbers which are added to the signal $s(t)$ at each time sample. However, to derive the statistical properties of the data, we consider $n(t)$ as a realization of some random process, where the value of n at each sampled time is drawn from a probability distribution. In a frequentist interpretation, this probability distribution could be reconstructed by an ensemble of identical detectors measuring the

same signal, each sampling a different realization of the noise. We make four assumptions about this probability distribution.

First, we assume that the noise is Gaussian-distributed. The dominant noise sources in GW detectors include shot noise—uncertainty in the number of photons measured by the photodetectors—and thermal noise due to the motion of the atoms in the mirror coatings. These sources cause Gaussian fluctuations in the measured strain [189], and so we assume that the noise $n(t)$ is also Gaussian distributed.

Second, we assume that n has mean zero, so that in the absence of a signal, the expected value of the data is zero.

Third, we assume the noise is stationary, meaning that its statistical properties do not change with time. Stationarity is a good assumption when analyzing short coherent waveburst on the order of seconds to minutes, which is the case for CBC signals detected in ground-based detectors [15]. Over these timescales, the detector and noise sources are not expected to change significantly.

Finally, noise sources and thus the time series $n(t)$ are generally specific to each detector. There are important exceptions, such as Schumann resonances (due to the resonance of the Earth-ionosphere cavity), and correlated seismic noise [199, 119, 118].

Besides the slow drift in the noise properties over the scales of minutes to hours, which makes the noise non-stationary, the data can also contain transient noise artifacts which are neither Gaussian nor stationary. These are called "glitches". Some example glitch sources include mechanical resonances in the mirror suspension apparatus and scattered light. Their origin and identification is an important focus of study in the analysis and detection of data [15].

With the assumptions of Gaussianity and stationarity, the noise can be characterized by its auto-correlation function, which is the expected value of the product of the noise at two different times:

$$C(\tau) = \langle n(t)n(t+\tau)\rangle, \tag{2.2}$$

where we note the lack of dependence on the absolute time t, due to stationarity. The brackets $\langle\rangle$ denote a mean over an ensemble of noise realizations. Its properties are estimated assuming ergodicity—that taking an average over time is equivalent to taking an average over an ensemble. The auto-correlation measures the correlation between the noise at different times, so that $C(0)$ is the variance of the noise. Stationarity also implies that $C(\tau) \to 0$ as $\tau \to \infty$.

That there is correlation between the noise at different times means that the probability distribution of $n(t)$, although Gaussian, has a covariance matrix that can have important

non-diagonal elements. Because of this, we find it useful to work in the frequency domain. There, stationary implies that the frequency components of the noise are uncorrelated, giving:

$$\langle \tilde{n}(f)\tilde{n}^*(f')\rangle = \frac{1}{2}S_n(f)\delta(f-f'), \tag{2.3}$$

where $\tilde{n}(f)$ is the Fourier transform of the noise, and δ is the Dirac delta function. S_n is the single-sided Power Spectral Density (PSD) of the noise, twice the variance of the noise at frequency f. The name "single-sided" is added with the factor of $\frac{1}{2}$. It is convention for convenience: because the noise is real-valued, the PSD is symmetric, and we only need to integrate over positive frequencies to obtain the covariance of the noise: $\langle n\,(t)^2\rangle = \int_0^\infty S_n\,(f)\,\mathrm{d}f$. In practice, the PSD can be estimated from the data using the Welch method [230]. Other techniques, such as fitting it using the BayesWave pipeline [59, 60], can also account for non-stationarity in the noise. Once the PSD is estimated, the data can be whitened by re-weighting the data in frequency space with the inverse of the square root of the PSD.

2.1.2 Match filtering

In the previous section, we described the properties of the noise that is added to physical signal in GW detectors. How can we establish whether a signal is present in the data? One solution is to use *match filtering*. The idea is to correlate the data with templates $h(t;\theta)$ which model the signal $s(t)$ underlying the data. Whether the correlation passes a certain threshold then suggests the presence or absence of a signal. The correlation quantity is $x := (d,h)$, the *match filter*. The inner product $(\cdot,\cdot)$ is defined for convenience, and to give later discussion a geometric interpretation:

$$(A,B) = 4\mathrm{Re}\int_0^\infty df \frac{\tilde{A}^*(f)\tilde{B}(f)}{S_n(f)}. \tag{2.4}$$

It measures the overlap of two time series A and B, with less importance given to the frequencies where the noise is large.

The match filter depends on the parameters θ of the template, and it is also a random variable since it depends on n. To quantify the strength of the correlation for a given θ, we define the SNR ρ as the ratio between the match filter and its standard deviation σ_x, which can be shown to be $\sqrt{h|h}$:

$$\rho = \frac{x}{\sigma_x} = \frac{(d,h)}{\sqrt{(h,h)}}. \tag{2.5}$$

When no signal is present, the SNR is a random variable with zero mean and unit variance. Sometimes, the SNR is defined as the expectation value $\langle\rho\rangle = \sqrt{h|h}$. The value of θ that maximises the SNR also maximises the likelihood ratio, which is the ratio of the probability that a signal is in the data against the probability that there is only noise in the data. A threshold on the SNR corresponds to a threshold on that likelihood ratio.

For GW templates, it is not possible to analytically compute the SNR. Instead, the data is compared to a set of templates arranged on a grid in parameter space. This grid is called a *template bank* and is chosen so that the loss in SNR due to not having the exact template is less than a certain threshold.

With the sensitivity of current detectors and the expected strain amplitude of the GW signals passing through them, detecting a GW signal is a noise-dominated problem, where we generally have $|n| \gg |h|$. Using a model is a good strategy in this regime, as it allows us to extract signals that would otherwise be buried in the noise. The assumption of a model has its downsides, as the actual signal may not be well represented by the template bank (for example, core-collapse supernovae are not well captured by CBC templates), in which case the signal will be missed. Some detection pipelines, therefore, do not rely on match-filtering. For example, the coherent WaveBurst [129, 130, 131, 132, 128] pipeline identifies excess power that is coherent across detectors and has been used in LIGO-Virgo-KAGRA (LVK) analyses. The MLy [202] pipeline uses convolution neural networks to identify coherent signals between detectors.

2.1.3 Parameter estimation

Detection of a signal is only the first step in analyzing GW data. We also want to extract the physical parameters of the source. To do so, we assume again that we have a template model for the signal $h(t;\theta)$, where θ is a set of parameters we want to estimate. Given the description of the noise in the previous section, what is the best estimator for θ?

The random process in the data is the noise n. The probability that we observe the data $d(t) = h(t;\theta) + n(t)$ given that the signal $s(t) = h(t;\theta)$ is the probability of observing the realisation $n(t)$. With the assumptions we made in Sec. 2.1.1—Gaussianity, stationarity, and zero-mean of the noise—the logarithm of this probability is

$$\log p(n(t)) = -\frac{1}{2}\int_{\infty}^{\infty} \frac{|\tilde{n}(f)|^2}{\frac{1}{2}S_n(f)} + \mathcal{N}, \tag{2.6}$$

where $\mathcal{N}$ denotes unimportant normalisation constants that do not depend on the variables.

With the inner product defined in (2.4), (2.6) becomes

$$\log p(n(t)) = -\frac{1}{2}(n,n) + \mathcal{N}. \tag{2.7}$$

We obtain the probability of observing the data $d(t)$ with an underlying signal $h(t;\theta)$ by substituting $n(t) = d(t) - h(t;\theta)$:

$$\log p(d(t)|\theta) = \log p(n(t)) = -\frac{1}{2}(d-h(\theta), d-h(\theta)) + \mathcal{N} \tag{2.8}$$

$$= (d, h(\theta)) - \frac{1}{2}(h(\theta), h(\theta)) + \mathcal{N}, \tag{2.9}$$

where $p(d(t)|\theta)$ is the probability of observing the data $d(t)$ given that the signal is $h(t;\theta)$, and the term $\frac{1}{2}(d,d)$ has been absorbed into the normalization constant since it does not depend on θ.

The Maximum Likelihood Estimator (MLE) $\theta_{\rm MLE}$ is the value of θ that maximises (2.9). It is obtained by solving

$$\frac{\partial}{\partial\theta^i}\log p(d(t)|\theta)\big|_{\theta=\theta_{\rm MLE}} = \left(\frac{\partial h}{\partial\theta^i}, d-h\right) = 0. \tag{2.10}$$

Note the geometric interpretation of the MLE. The template models $h(t;\theta)$ define a manifold in the space of possible signals (where each dimension is the value of a time sample). The parameters θ are coordinates on this manifold. The MLE is the point on the manifold that is closest to the data point $d(t)$: the value of θ that minimizes $(d-h, d-h)$. The condition (2.10) is the statement that the line between the data and the template is orthogonal (with respect to the metric induced by the inner product) to the manifold at the MLE. It can be shown (see Appendix to Chapter 2 in [83]) that the value of θ that maximises the SNR is the MLE.

At this point, discussing the meaning of $p(d|\theta)$ is important. In a frequentist interpretation of probability, $p(d|\theta)$ has meaning as the distribution many repeated measurements would produce if $h(t;\theta)$ is the true signal. To infer physics from the data, however, we want to make some measurement of θ and therefore compute $p(\theta|d)$. This quantity does not have a frequentist interpretation—θ is either the true parameters of the signal or not; it is not a repeatable measurement. Instead, Bayesian inference is used, where we define the *posterior probability* $\mathcal{P}(\theta|d) := p(\theta|d)$, which measures our belief that the parameter θ is true given the data d. In Bayesian nomenclature, $\mathcal{L}(d|\theta) := p(d|\theta)$ is called the *likelihood*. The posterior is obtained from the likelihood using Bayes' theorem [28]:

$$\mathcal{P}(\theta|d) = \frac{\mathcal{L}(d|\theta)\,\pi(\theta)}{Z}, \tag{2.11}$$

where $\pi(\theta) := p(\theta)$ is the *prior* on θ, which encodes our knowledge of the parameters before the data is known, and $Z := p(d)$ is the *evidence*. As the evidence does not depend explicitly on θ, it is often treated as a normalisation constant.

Computing the posterior is expensive as it requires the evaluation of the waveform model for ranges of each parameter in θ. As we will discuss in Sec. 2.1.4, these number 15 or more for CBC signals. A computationally efficient way to obtain the shape of the posterior as well as statistically meaningful quantities, such as the MLE and the credible intervals (which give the range of values of θ within which we expect the true value to lie with a certain probability), is to produce samples of sets of parameters θ distributed according to the posterior. Sampling can be done, for example, by using specialized algorithms like Nested Sampling or Markov Chain Monte Carlo methods.

2.1.4 GW templates

What do the templates $h(t;\theta)$ look like for GW signals? For a BBH signal, the parameters θ are

- the masses of the binary components;
- the spins of the binary components (6 parameters);
- the luminosity distance d_L to the source;
- the angle between the total angular momentum of the binary and the line of sight θ_{JN};
- the time of coalescence;
- the phase of the signal at coalescence;
- The position of the binary on the sky, given by the right ascension α and declination δ; and
- the polarisation of the signal ψ.

This list of parameters can be categorized into two. Intrinsic parameters are the properties of the CBC independent of the detector. They determine the dynamical evolution. They include the masses and spins of the binary components, to which the eccentricity is sometimes added. The eccentricity of the binary is generally expected to be small in

the bandwidth of ground-based detectors, as the energy loss circularises the orbit early in the inspiral. However, some CBC signals may retain a detectable eccentricity at coalescence [195]. This small number of parameters needed to describe the signal is a consequence of the uniquess theorems mentioned in Sec. 1.1.6. Although few, these parameters affect the signal in a complex way.

The other parameters are called extrinsic parameters and depend on the position of the source with respect to the detector. Their effect on the signal can be written in an analytic, closed form and is generally decoupled from the intrinsic parameters. [1] This decoupling is practical when computing the MLE, as the expensive computation need only be performed over the intrinsic parameters (template banks do not have to cover all possible values of the coalescence time, for example).

As a representative, GW signal templates are of the form

$$\tilde{h}_+(f) = \frac{1}{d_L} F_+(\alpha, \delta, \psi) \left(\frac{1 + \cos^2(\theta_{JN})}{2} \right) A(f; a) \exp(\Phi(f; a)), \tag{2.12}$$

$$\tilde{h}_\times(f) = \frac{1}{d_L} F_\times(\alpha, \delta, \psi) \cos(\theta_{JN}) A(f; a) \exp(\Phi(f; a) + i\pi/2), \tag{2.13}$$

where $\mathcal{A}(f; a)$ is the amplitude of the signal, $\Psi(f; a)$ is the phase of the signal, and a stands for the intrinsic parameters. Only the $+$ and $\times$ polarisation modes, which are the only polarization modes in GR, are shown above. The form of the amplitude and phase can be obtained analytically to some PN order; using the Effective-One-Body formalism [37]; or some other approximation method in the inspiral phase of the CBC. Template banks are constructed using approximant waveforms, which combine analytical methods giving the waveform in the inspiral and interpolating merger phase waveforms from numerical relativity simulations (see [143, 106, 54, 144] for reviews) to obtain a semi-analytical waveform that covers the entire coalescence.

Besides the dependence on the distance and the line-of-sight angle, the extrinsic parameters also affect the signal through the antenna patterns F_+ and $F_\times$. In addition to the sky localization and polarisation, the antenna patterns also depend on the specific configuration of the detector, including the orientation of the arms. They are functions of time since the orientation of the detector changes as the Earth rotates (and as the Earth/detector moves with respect to the source). This effect is negligible for short signals, such as those from more massive compact binaries, but become consequential as the signal duration increases.

[1] As a counter-example, precession due to the spins of the binary components being misaligned with the orbital angular momentum can cause the inclination angle to change over time, thus coupling it with the intrinsic parameters.

2.2 Testing the standard model of GWs

The previous sections gave an overview of the body of assumptions that make up the "Standard Model (SM)" of GWs. These assumptions include that GR is the theory describing the generation, propagation, and polarization of GWs; that the astrophysical sources emitting the GWs detected by ground-based detectors are BBHs, BNSs, and NSBHs; and that the noise in the detector is mostly stationary and Gaussian. These assumptions are used in the detection (see Sec. 2.1.2) and in the physical interpretation (see Sec. 2.1.3) of the GW signals. We will refer to any deviation from this combination of assumptions as a "Beyond Modeled (BM)" signature. These deviations can be due to the presence of new physics, such as additional terms in the action of gravity as explained in Sec. 1.1.2, or due to the incompleteness of our model. For a review of possible Beyond Modeled (BM) deviations that are not due to new physics, see [104].

Current tests for BM signatures examine potential deviations from the SM. Null tests are arguably the cleanest approach to testing the current SM. They determine whether signals are consistent with the expectations of the model. However, on their own, they do not inform us of the physical meaning of a given deviation. To that end, other tests have been devised that target parameterized deviations in the PN (and Post-Einsteinian) description of the inspiraling behaviour and quasi-normal modes of the newly formed BH that might result from a merger (see e.g. [24, 5] and references cited therein). With these tests, such deviations can, in principle, be closely connected with specific effects from particular theories—or at least provide physical information on the main impact of deviations from GR [239]. On the other hand, agnostic tests examine the residual (between the consistent SM signal and the observed data) and aim to qualify the behaviour of any departure (see e.g [24, 122]). [2] This approach can accommodate yet-to-be-modelled physics.

To date, available observations obtained with the LVK network have already made it possible to place constraints on BM phenomenology. For instance, by constraining beyond-GR gravity and potential effects associated with exotic compact objects. For the former, some constraints have been derived on deviations with particular physical consequences. For example, constraints have been derived on the coupling parameters of certain Scalar-Tensor theories in BNSs [149, 166], the graviton mass [24], and the number of possible space-time dimensions [178]. Others have been derived on deviation coefficients that

[2] Rather than looking at the difference between the data and the best-fit waveform template, agnostic tests can also add deviations with general forms directly to the waveform templates, such as in [85], where splines are used to fit the deviations.

may arise in many different beyond GR theories; for example on the PN expansion coefficients [163, 240], on propagation effects [134, 154, 168, 201], on additional modes of polarizations and on some potential signatures of black hole mimickers [3, 8, 215, 231].[3] Constraints for all of the effects mentioned above have been presented by the LVK collaboration [13, 24].

Notably, no compelling evidence has so far been found for deviations from the SM. However, as the sensitivity of GW detectors improves [238, 241, 218], new ground- [218] and space-based [26] detectors become available, and more events are detected, deeper tests will be increasingly possible. In addition, it is worthwhile to recall from Sec. 1.2.3 that the accuracy of current BM templates will have to be increased by several orders of magnitude for the impact of systematic error to remain below that of statistical errors in 3G detectors. Thus, devising suitable strategies to analyze residuals will become increasingly important.

2.3 `SCoRe` framework overview

In the previous sections, we introduced the SM of GWs, which consisted of a set of assumptions that describes GW signals as well as the noise in the detectors. We considered an overview of current GW science, in particular, the tests for BM signatures that examine potential deviations from the SM. In the rest of this chapter, we introduce the `SCoRe` framework, which provides tools to detect and interpret BM signatures in GW data. The contents of this chapter are based on the first part of [71].

2.3.1 Motivation

The search for BM physics using GWs is challenging due to multiple reasons, including both theoretical and experimental limitations. We are limited by our understanding of the instrument noise properties when differentiating any BM signature from noise artifacts, especially in light of current evidence suggesting any deviation is likely to be subtle. Indeed, even in the scenario where the statistical properties of a detector are well characterized, and it is difficult to confidently assign the origin of a small BM signature as astrophysical

[3] Frameworks for obtaining these constraints are developed in [232] for the mass of the graviton, in [29, 30, 165, 162] and [159, 160, 172] for propagation effects and for exotic compact objects by analysing the post-merger ringdown [32, 44, 45, 47, 101, 158, 77]. Some descriptions of possible exotic compact objects include [155, 145, 100, 67]. The use of detectors to search for non-GR polarization modes was described as far back as 1973 [80].

and not from a known (or unknown) instrumental property. This is because the noise properties of a detector can be far from a Gaussian distribution and can also have non-stationary behaviour [9, 15, 140, 55, 187, 86]. In particular, glitches and other uncontrolled sources of noise make searching for BM signatures challenging [139].

Distinguishing the BM signature from detector noise is only the first challenge—as then one would also like to understand the physics of such signature and its dependence on the GW source properties. We are limited by the number of theoretical waveforms needed to test for the vast range of potentially BM scenarios (either for missing physics within GR, or sufficiently generic and complete waveforms beyond it).

Thus, often, one fits the data with available waveform models to infer the best-fit source parameters and searches for any coherent residual signal [16, 11, 14, 24, 18]. However, the limitation remains in how well a framework can identify a BM signature and the appropriate metric to quantify a deviation. An example is the uneven performance of specific tests with different events (e.g. [122]).

A few salient features expected from any BM signature(s) in GW data are (i) BM signatures will be common in the data of multiple detectors, but uncorrelated detector noise will not, (ii) a large class (if not all) of BM signatures can be understood as additional loss/gain in the orbital energy of a coalescing binary (e.g. [64, 239, 27, 233]) when compared to the SM (GR, and sources involving black holes and/or neutron stars), (iii) BM signatures can depend on the GW source properties.

2.3.2 Description

Motivated by the above considerations, we propose a new method called *Structured Correlated Residual* (`SCoRe`) power spectrum. `SCoRe` searches for BM signatures by measuring the Correlated Residual Power Spectrum (CRPS) between multiple pairs of GW detectors. This method is designed such that it is not susceptible to contributions from uncorrelated noise between a pair of GW detectors and can search for any (un-)modelled signals. The method has three key characteristics, each exploiting and targeting the three features of BM signatures listed previously: (i) the residual GW data obtained after subtracting a modeled GW signal for a given waveform and source parameters are cross-correlated within pairs of detectors—to help distinguish signal from noise; (ii) the CRPS obtained is projected on a physically motivated template. This template is either composed of the derivatives of the orbital frequency up to order n (for a model-independent search) or derived from a particular physical model (for a model-dependent search)—to help characterize the signal;

(iii) the projection is estimated as a function of the GW best-fit source parameters from the signal after marginalizing its uncertainties.

The first step applies cross-correlation to the residual data obtained after subtracting a *best-fit* signal model from the strain data. This best-fit model is constructed using the values allowed by the posterior on the GW source parameters inferred from the detector network using the SM. We do this to help mitigate the contribution from uncorrelated noise to the residual signal by cross-correlating a total of $N_{\rm det}(N_{\rm det}-1)/2$ pairs of detectors, where $N_{\rm det}$ is the number of detectors. Cross-correlation is a useful technique to search for weak signals from noisy GW data and is often used to search for stochastic GW background signals [19, 6]. It is a time averaging over the product of the strains in two different detectors. Because the noise at the two detectors is not correlated, its mean average is zero, and its standard deviation decreases as the timescale of integration increases. A price is paid, however, for this noise reduction: features shorter than the averaging timescale will be lost.

The second step aids in looking for a *physics-driven* BM signal in either a model-dependent or a model-independent way. The method searches for a specific type of frequency dependence in the CRPS which can be unmodeled and driven by *chirp-like* behavior, or model-specific. Projecting onto template functions also further reduces noise by filtering particular, model-motivated structures in the signal. We suggest templates that are naturally expressible in terms of the orbital frequency.

The cross-correlation technique ensures that uncorrelated noise sources will not contribute to the mean of the CRPS. Meanwhile, projection to a suitably chosen set of functions can help pick features missing from the SM for follow-up analysis on their physical meaning. This is described in detail in Sec. 2.4.2. It is important to note that any source of correlated noise, such as the noise that arises due to the Schumann resonance [199, 175, 213, 214], will contaminate the cross-correlation signal. We do not consider correlated noise in this work. Future studies will investigate the impact of correlated noise on `SCoRe` and how it can be mitigated.

The final step takes into account possible dependencies of the BM signal on the GW source parameters and can also mitigate uncertainties related to the source parameters.

2.3.3 Implementation

In this work, we consider the "best-fit" model of the signal to be the maximum likelihood GR waveform obtained by parameter estimation of the network strain. In the presence of a BM signature, this estimator may have a "stealth bias". This is when a GR waveform

with different source parameters can—even partially—account for the signature [220, 221]. A different set of GR parameters may perfectly reproduce the BM signature in the worst scenario. Any residual test would then be unable to distinguish such BM signatures from the SM. In [169], the effect of stealth biases on the measurement of a particular BM model was studied. The model consisted in Numerical Relativity (NR) waveforms produced through an "order-by-order" strategy designed to capture, to a certain extent, dynamical Chern-Simons gravity with source parameters similar to a detected signal, GW150914 [10]. Although GR waveforms could partially reproduce the residual strain, it was found that at least part of it could not be accounted for by the GR source parameters correcting for the BM signature, a consequence of deviations lying off the GR waveforms manifold. We note in passing that it is not guaranteed that all BM models have an orthogonal component to the SM manifold. There exist beyond GR theories allowing for signals purely degenerate with GR waveforms for some source parameters and not for others. For example, theories that predict more significant deviations at higher curvature scales may not lead to measurable differences with GR for larger compact object masses. Another well-known example is spin-induced moment [196, 184, 141, 138], which by definition is an effect proportional to the spin of the object. We do not explore such degenerate scenarios in this work.

Although the idea of using template functions in frequency space is similar to the frames used in the `BayesWave` framework [59, 60] (which can also be used as template functions in `SCoRe`), our method does not seek to reproduce the residual signal with a set of functions. This is unlike current residual tests that use `BayesWave` [18, 24]. Instead, we measure the degree to which a pre-determined finite set of functions can explain the residual strain. This makes `SCoRe` morphology-dependent, but the morphology of the chosen template functions is arbitrary and can be non-specific. For example, one could reproduce the deviations parameters used in parametrized tests [5, 117, 157, 18], but choosing an agnostic template set using `SCoRe` is also possible as we will explain in Sec 2.4.2.

By using cross-correlation and projection onto a template, we hope to reduce noise well below that of individual detectors. With this noise reduction, `SCoRe` may be able to unearth minute BM signatures, which would otherwise, remain undetected by only considering the strain of individual detectors. By looking at the structure of the CRPS, the method can help constrain potential deviations with a vast range of possible forms. This also means that the search for potential deviations can be made tighter as their form is guided by theoretical work. Furthermore, the method can probe for correlations between the BM signature and the GW source parameters. A schematic diagram illustrating the basic principles of this technique is depicted in Fig. 2.3.3.

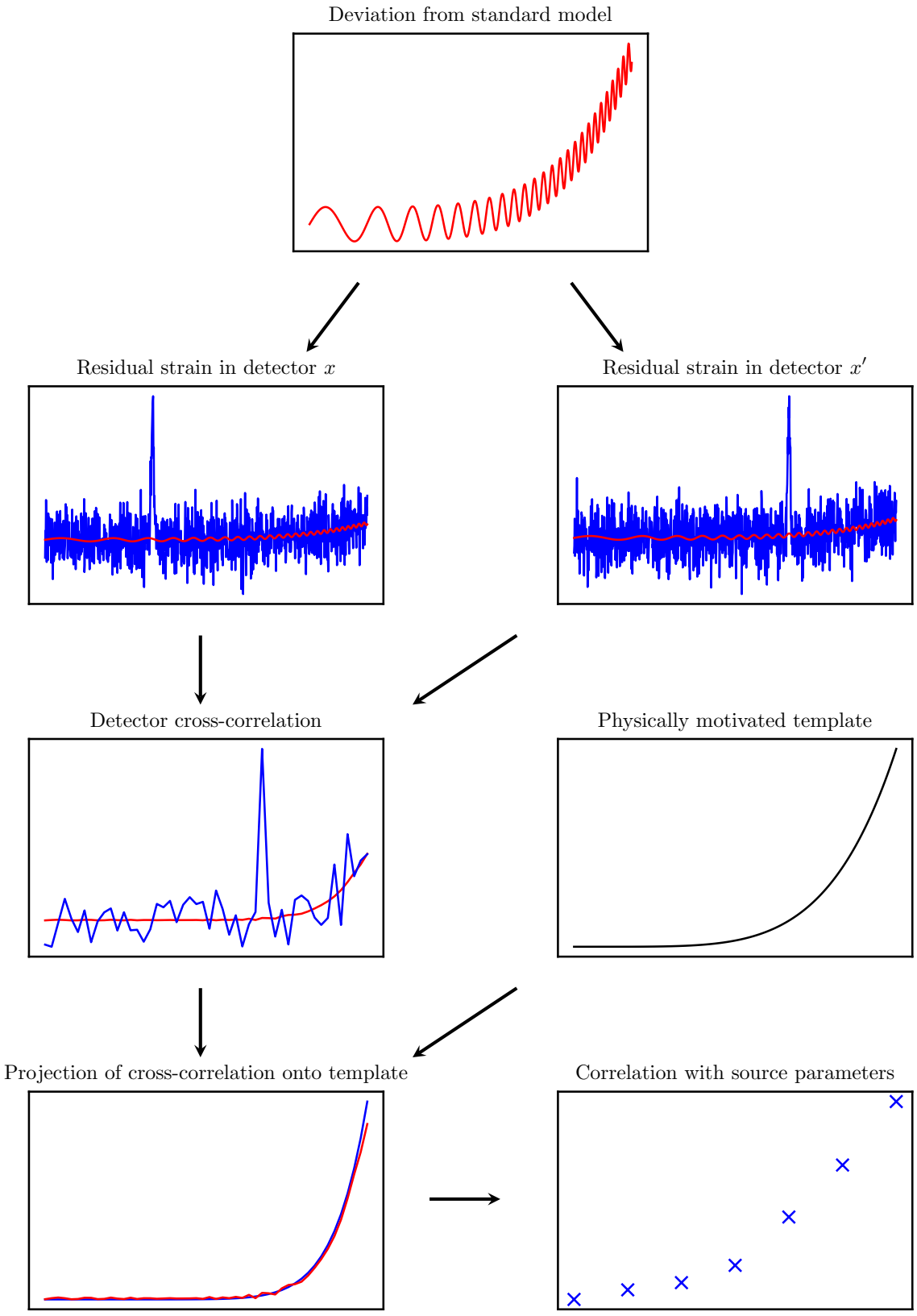

Deviation from standard model
Residual strain in detector x
Residual strain in detector x'
Detector cross-correlation
Physically motivated template
Projection of cross-correlation onto template
Correlation with source parameters

Figure 2.1: (Opposite page) Outline of the SCoRe method. When a BM signature (in red) is measured by a pair of GW detectors, each detector will add different noise to it. The resulting residual strains, computed by subtracting the best-fit SM waveform from the data are plotted in blue. Noise that is uncorrelated between detectors will be reduced when taking the cross-correlation between the two detectors. Higher power transient noise and correlated noise may remain but can be mitigated by projecting CRPS onto some physically motivated template. Most BM signature models have a dependence on the source parameters. The projection coefficients measured over events of different source parameters may reveal such correlation.

2.4 SCoRe formalism

We describe in this section the formalism of SCoRe, which consists of four parts, **(A) Cross-correlation, (B) Choice of a residual template, (C) Projection on a template, and (D) Inference using a Bayesian framework**.

As discussed in Sec. 2.1.1, we write a linear model of the GW data $d^x(t)$ in a detector denoted by x as

$$d^x(t) = s^x(t) + n^x(t), \tag{2.14}$$
$$\tag{2.15}$$

where $s^x(t) = \sum_i F_i^x(t) s_i(t)$ denotes the observed GW signal as seen by a detector, written in terms of the actual signal $s_i(t)$ for the polarization state "i", and the corresponding detector response function $F_i^x(\mathrm{t})$. The noise in detector x is $n^x(t)$. Whether a signal is detected in a particular detector depends on the noise in the detector and the detector response function $F_i^x(\mathrm{t})$ to the source position. In this work, we consider that a GW signal detected with a SM template in multiple detectors with a matched filtering SNR ρ greater than a minimum threshold network SNR ρ_* is classified as an event.[4]

We define the BM signature Δs^x as the difference between the model $h^x(t;\theta)$ at the true parameters θ_T and the physical signal s^x, so the data can be written as

$$d^x(t) = h^x(t;\theta_\mathrm{T}) + \Delta s^x + n^x(t). \tag{2.16}$$

As discussed in Sec. 2.3.1, the BM signature can be due to new physics or model inaccuracy. Overlapping signals can also contribute to Δs^x, and will be particularly important for next generation detectors [110].

[4] See [12, 17, 23] for a description of the actual pipelines used by the LVK to identify candidates.

From the data, we can approximate the BM signature by computing the residual strain for a given model $h(t;\theta)$:

$$r^x(t;\theta) = d^x(t) - h^x(t;\theta) \tag{2.17}$$
$$= h^x(t;\theta_{\rm T}) - h^x(t;\theta) + \Delta s^x + n^x(t). \tag{2.18}$$

The difference between the true parameters $\theta_{\rm T}$ and the estimated parameter θ is due both to noise and degeneracies between the BM signature and the model (the "stealth bias"). We call the difference between the model at the true parameters and the model at the estimated parameters $\Delta h^x := h^x(t;\theta_{\rm T}) - h^x(t;\theta)$. The challenge is correctly modelling Δs^x.

Performing parameter estimation over the strains in the detector network gives a posterior over θ. By definition, the MLE $\theta_{\rm MLE}$ of the parameters (see Sec. 2.1.3) corresponds to the minimum residual strain amplitude in comparison to the variance in the detector noise, as $\theta_{\rm MLE}$ should maximize the likelihood.

We propose performing tests of BM physics on the residual data $r^x(t;\theta_{\rm MLE})$ constructed using the MLE parameters inferred using a network of detectors, $\theta_{\rm MLE}$. The MLE parameters need not be the true parameters of the source parameters—they only resemble the data best given a waveform model and the assumption of the standard model. Since such parameters will be generically described with a distribution, we introduce in Sec. 2.4.4 a Bayesian framework to marginalize their (posterior) distribution.

2.4.1 Cross-correlation of the residual signal

One of the critical aspects of a BM signature in the residual data is that it is likely to be correlated in all the detectors. However, depending on the detector response function, it will be observed differently in each detector. Noise between multiple GW detectors from unrelated sources will be random. To identify the origin of the residual as either astrophysical (a BM signature) or due to detector noise, we propose to do a cross-correlation of the residual signal between the data from two detectors. Given the output $d^x(t)$ and $d^{x'}(t)$ of two detectors x and x', the general cross-correlation $Y(\tau)$ of the two signals over a timescale τ is defined as

$$Y(\tau) \equiv \frac{1}{\tau}\int_{t-\tau/2}^{t+\tau/2} dt_1 \int_{t-\tau/2}^{t+\tau/2} dt_2 d^x(t_1) d^{x'}(t_2) Q(t_1,t_2), \tag{2.19}$$

where $Q(t_1,t_2)$ is a filter function. The choice of τ should balance two effects: correlated noise is better reduced as τ increases, but averaging washes away signal features with

timescale shorter than τ. In the limit where τ spans the length of the signal, the cross-correlation becomes the total residual power observed. There are natural choices of τ, which rely on maximizing SNR while ensuring the features of the signal are preserved. They will depend on the source parameters, most notably the chirp mass, which sets the timescale of the orbital frequency evolution and the choice of template function on which to project the CRPS. We discuss the methodology behind choosing τ with a specific example in Sec. 3.1.2.

The definition (2.19) has been used to search for stochastic GW signal [19, 6]. There, the strain in multiple detectors is used to search for a common, periodic signal [70]. In stochastic GW background searches, the phase of the signal is not expected to be resolved. This makes choosing the optimal filter function non-trivial. By contrast, we can measure the phase of a well-detected event and measure Δt, the delay time separating the two detectors within a timing uncertainty. The optimal filter function, which gives the highest SNR, will correspond to the signals in the detectors overlapping in time. It is therefore $Q(t_1, t_2) = \delta(|t_1 - t_2| - \Delta t)$ (assuming $\tau \gg \Delta t$). We can then define the cross-correlation with maximum SNR with angular brackets:

$$\left\langle d^x(t) d^{x'}(t + \Delta t) \right\rangle_\tau \equiv \frac{1}{\tau} \int_{t-\tau/2}^{t+\tau/2} dt' d^x(t') d^{x'}(t' + \Delta t). \tag{2.20}$$

In `SCoRe`, we consider the cross-correlation of the residual strains. We first expand the product between the residual strains in the two detectors:

$$\begin{aligned} r^x r^{x'} &= \Delta s^x \Delta s^{x'} && (2.21)\\ &+ \Delta h^x \Delta h^{x'} + \Delta s^{x'} \Delta h^x + \Delta s^x \Delta h^{x'} && (2.22)\\ &+ \Delta s^{x'} n^x + \Delta s^x n^{x'} + \Delta h^x n^{x'} + \Delta h^{x'} n^x && (2.23)\\ &+ n^x n^{x'}. && (2.24) \end{aligned}$$

Taking the cross-correlation of the residual strains gives the mean excess power emitted within time bins of width τ, which we denote as $D^{xx'}(t)$. Since the noise in the two detectors is uncorrelated and the mean of the noise in each detector is zero, the terms on the third line of Eq. (2.21) are reduced by $\tau^{\frac{1}{2}}$. We do not consider terms involving Δh^x here. The key assumption is that the term $\Delta s^I \Delta s^J$ on the first line of Eq. (2.21) is correlated between detectors and does not average to zero within τ, while the uncorrelated noise in the two detectors averages to zero. Therefore, when taking the cross-correlation of the residuals, we obtain:

$$\begin{aligned} D^{xx'}(t) \equiv& \langle r^x(t; \theta_{\rm MLE}) r^{x'}(t + \Delta t; \theta_{\rm MLE}) \rangle_\tau, \\ =& \langle \Delta s^x(t) \Delta s^{x'}(t + \Delta t) \rangle_\tau + \langle n^x(t) n^{x'}(t + \Delta t) \rangle_\tau. \end{aligned} \tag{2.25}$$

The value of Δt will depend on the source parameters such as the sky position and also on the position of the two GW detectors x and x' between which the signal is correlated. This can be inferred for individual pairs of detectors and need not be assumed in the analysis. The detection of the correlated signal $D^{xx'}(t)$ depends on the overlap of the signal $\Delta s^x(t)$ between the individual detectors, which depends on the response functions of the detectors $F_i^x(\mathrm{t})$. We can marginalize over the response functions and extrinsic source parameters, as explained in Sec. 2.4.4, so that we may account for different residual signatures that will be induced by the same BM deviation in different detectors. But, if, for a given antenna pattern, a theory predicts no measurable residual signature in multiple detectors, then the cross-correlation will not yield anything.

Using the cross-correlation definition given in Eq. (2.20), we can model the measured cross-correlated signal as

$$D^{xx'}(t) = S^{xx'}(t) + \mathcal{N}_c^{xx'}(t), \tag{2.26}$$

where the first term denotes the correlated signal between the two detectors and the second term denotes the correlated residual noise between the two detectors. We usually assume that the noise between detectors is uncorrelated. In reality, some noise, like magnetic noise, can be correlated. These types of noise can play a role at some level in the mean, and their impact on the signal should be estimated when this technique is applied to the data.

If the noise is uncorrelated between the two detectors, then the second term in Eq. (2.26) vanishes, and only the first term is non-zero. As a result, we can write

$$\begin{aligned} D^{xx'}(t) =& \langle \Delta s^x(t) \Delta s^{x'}(t+\Delta t) \rangle_\tau \\ &+ \langle n^x(t) n^{x'}(t+\Delta t) \rangle_\tau \delta_{xx'}. \end{aligned} \tag{2.27}$$

Alternatively, one can work in the time-frequency domain using the short-time Fourier transforms of the strains $s^x(t)$ and $s^{x'}(t)$ and substituting in Eq. (2.20). The timescale used to compute the short-time Fourier transform should not be greater than the timescale of cross-correlation τ.

In the remaining analysis, we will work in the time domain for concreteness.

2.4.2 Choice of residual Templates

The second "key-physics"-driven aspects that we want to explore in CRPS signals is that there might be more energy injection/extraction from a binary system in BM scenarios than in the SM templates. This difference in power released results, in particular, in a change

in the orbital frequency evolution $f(t)$. Previous residual tests, such as the ones using BayesWave [59, 60], have proposed decomposing residual signals in terms of frames that have a natural expression in the frequency domain (Morlet-Gabor sine-Gaussian wavelets and "chirplets" [59]). Along similar arguments, we propose decomposing the CRPS signal into a template of n orbital frequency-dependent functions $Z_i(f(t))$, which can capture any gain/loss in the (radiated) energy of the binary source after taking into account the dependence on the source parameters

$$S^{xx'}(t) = \sum_{i=1}^{i=n} \alpha_i(\theta, t) Z_i(f(t)), \tag{2.28}$$

where the (real) coefficients α_i may depend on the source parameters and time. These coefficients vanish when no BM signature is present in the data. Either side of the equation is valued in strain squared and will depend on the integration timescale τ. The only requirement on the set of templates $Z_i(f(t))$ is that its elements should not be parallel to one another. They need not be either normalized or orthogonal. For example, one could choose wavelets or chirplets. Notice that one can also model the BM signature in terms of the residual strain of the GW signal rather than the power. As one still uses the CRPS to extract posterior information in either approach, they will yield the same information. We describe the strain modelling in Appendix A.1.

The specific form of the template functions $Z_i(f(t))$ can be motivated by a particular type of BM signature if such knowledge is available. As an alternative to choosing a specific, model-dependent set of template functions, we present a choice of template that we argue allows for an unmodeled BM search. The unmodeled template is constructed from the following observation: BM effects modify the rate of energy dissipation. This, in turn, impacts the rate at which orbital frequency increases. We thus expect the derivatives of the orbital frequency of the system to be good tracers of a BM signature.

More specifically, to capture the proportional change in time of the orbital frequency, we use the derivatives of $\dot{f}/f$ as our template functions

$$Z_{i>0}(t) = \left\langle \left(\frac{d^i \ln f(t)}{dt^i} \right)^2 \right\rangle_\tau , \tag{2.29}$$

while $Z_0(t)$ is constant, defined to capture any BM signature with constant power. If the template functions are defined as functions of continuous time, one can take the angular bracket, as defined in Eq. (2.20), to define the expected CRPS functions.

We note that for inferring the values of α_i from data, it is convenient to orthogonalize and normalize the template functions, e.g. using the Gram-Schmidt process, if possible. If

the physical interpretation of the coefficients is more straightforward in the original form, then one can always transform the functions and their coefficients back.

2.4.3 Projection on a template

The projection of the CRPS of the data onto the chosen template encodes how well the model matches the signal. In this subsection, we define the projection coefficients and the associated uncertainty. The projection coefficient $\Gamma_i(D)$ of the CRPS signal $D^{xx'}(t)$ onto the template Z_i is:

$$\Gamma_i(D) = \int_{t_s}^{t_e} dt D^{xx'}(t) Z_i(f(t)), \tag{2.30}$$

(t_s, t_e are the start/end of the signal in the data). Then, the requirement that the template functions should not be parallel is

$$Z_i - \Gamma_i(Z_j)\tilde{Z}_i \neq 0 \,\forall\, \{j \neq i\} \in n, \tag{2.31}$$

where $\tilde{Z}_i$ is normalized, so $\Gamma_i(\tilde{Z}_i) = 1$. The templates can be made orthonormal, that is $\Gamma_i(Z_i) = 1$ and $\Gamma_i(Z_j) = \delta_{ij}$, if required for the inference of the signal. If an orthonormal set is chosen, then the projection coefficient $\Gamma_i(S)$ will be equal to α_i. This is possible as long as the template functions are not linearly dependent. In the rest of this work, we will assume that the Z_i used are orthonormal ; hence, the value of α_i is measured as the mean value of the data projection onto the template functions.

When measuring the CRPS and the coefficients, we will need to know the associated uncertainty. In this work, we compute the standard deviation in the limit of small-signal (zero mean value). In the limit where the cross-correlation scale goes to zero, $\tau \to 0$, the noise on the cross-correlation estimator can be obtained as

$$K_n^2 \equiv \langle (r^x(t) r^{x'}(t + \Delta t))^2 \rangle_\tau - D^{xx'}(t)^2. \tag{2.32}$$

Assuming that the noise in each detector is Gaussian, stationary, and uncorrelated, we can simplify the above expression as [5]

$$\begin{aligned} K_n^2 \equiv & \langle n^x(t) n^x(t) \rangle \langle n^{x'}(t) n^{x'}(t) \rangle, \\ = & N_x^2 N_{x'}^2, \end{aligned} \tag{2.33}$$

[5]The angular brackets are defined in Eq. (2.20). From this point, we drop the subscript τ for brevity.

where in the second line, we have defined the noise auto-correlation of each detector as $N_x^2 := C(0)$ (see Sec. 2.1.1).

If there are no BM signatures present in the data, then the value of the coefficients α_i should be consistent with zero. However, in the case of a non-zero signal, we can write the estimator $\hat{\alpha}_i$ from the data. Assuming α_i does not depend on time, then we can write it in terms of the CRPS $D^{xx'}(t)$, the template functions $Z_i(f(t))$, and the noise on the CRPS, K_n, as

$$\hat{\alpha}_i^{xx'} = \int_{t_s}^{t_e} dt W_i(t) D^{xx'}(t) Z_i(f(t)), \tag{2.34}$$

$$\text{where } W_i(t) \equiv \frac{K_n^{-2}(t)}{\int_{t_s}^{t_e} K_n^{-2}(t) Z_i^2(f(t)) dt}. \tag{2.35}$$

In the above equation, $W_i(t)$ are weights which serve two purposes: (i) they ensure that the equation is normalized, and (ii) they account for any variation in the noise properties in the detector by inverse noise weighting. This helps reduce uncertainty in the estimator. For the situation of uncorrelated stationary Gaussian noise considered in this analysis, the values of $W_i(t)$ will be constant and will simply normalize $Z_i(t)$. However, if the PSD across a data segment shows variation with time $N_x^2(t)$ (non-stationarity), then $W_i(t)$ will not be a constant. If the $Z_i(f(t))$ are not orthogonal, $\hat{\alpha}_i$ will generally be non-zero even when $D^{xx'}(t) = Z_j(t)$, for $j \neq i$. When $\hat{\alpha}_i = 1$, the mean excess power measured for the template function Z_i is equal to the expected power due to noise.

Finally, it is of interest to estimate the SNR for measuring the parameters $\hat{\alpha}$. For N_{GW} sources with GW similar source parameters and with $N_{\rm det}$ GW detectors, we can write the combined SNR, ρ_i, as

$$\rho_i = \bar{\alpha}_i \times \left[\sum_{x=1,x'>x}^{N_{\rm det}} \sum_{j}^{N_{GW}} \left(K_{\alpha_i}^{xx'}\right)^{-2} \right]^{1/2}, \tag{2.36}$$

where, $\bar{\alpha}_i$ is the mean value of the inferred signal for all the detectors pairs and sources, and $(K_{\alpha_i}^{xx'})^2$ is the noise on the parameter α_i, defined as

$$(K_{\alpha_i}^{xx'})^2 = \int_{t_s}^{t_e} dt \left(W(t) K_n Z_i(t)\right)^2. \tag{2.37}$$

From the expression given in Eq. 2.36, we can conclude that the total SNR ρ to measure a deviation α_i scales as $\sqrt{N_{GW}}$ and $\sqrt{N_{\rm det}(N_{\rm det}-1)/2}$. Finally, it is important to clarify that the value of α can explicitly depend on the value of the source parameters θ, and in that case so will the number of GW sources $N_{GW}(\theta)$ with the source parameter θ (for e.g $\theta_{\rm MLE}$) that needs to be combined to obtain the SNR.

2.4.4 Inference using the Bayesian framework

The final step of `SCoRe` is to combine the information from different events, assuming a dependence of the BM signature on the source parameters. The proper framework to do this is hierarchical Bayesian inference, where we define multiple stages of parameters, each given by a probability distribution parametrized by the previous stage. The hierarchy of the model is defined by the directed relations between the parameters. The intermediate parameters are marginalized over, allowing the inference of the highest level parameters called hyperparameters.

In this section, we formulate a hierarchical Bayesian framework to measure the presence of any BM signature in the observed data by marginalizing over the uncertainties associated with the GW source parameters. Let us denote Δ_M as a set of parameters which captures deviations from the SM. They denote parameters that are common to all events, such as the coefficients of higher dimensional terms in the EFT of gravity. Then, we can write the posterior distribution $\mathcal{P}\left(\Delta_M|\{d^x(t)\}\right)$ on the parameters Δ_M given the observed set of data $\{d^x(t)\}$ detected at detectors labelled $x, x', \ldots$ using Bayes' theorem [28] as

$$\mathcal{P}\left(\Delta_M|\{d^x(t)\}\right) \propto \mathcal{L}\left(\{d^x(t)\}|\Delta_M\right)\pi\left(\Delta_M\right), \tag{2.38}$$

where $\mathcal{L}\left(\{d^x(t)\}|\Delta_M\right)$ denotes the likelihood on the data set and $\pi\left(\Delta_M\right)$ denotes the prior on the deviation hyperparameters. For a set of $N_{\rm obs}$ independent events of GW sources detected (denoted by $\mathcal{S}$) above a matched filtering SNR ρ_*, the likelihood on the data set is the product of the likelihood on individual events, weighted by the probability of detecting the event:

$$\begin{aligned}\mathcal{L}\left(\{d^x(t)\}|\Delta_M\right) &= \prod_{x,x'>x=1}^{N_{\rm det}} \prod_{i=1}^{N_{\rm obs}} \mathcal{L}\left(\{d^x, d^{x'}\}_i|\mathcal{S},\Delta_M\right) &(2.39)\\ &= \prod_{x,x'>x=1}^{N_{\rm det}} \prod_{i=1}^{N_{\rm obs}} \frac{p(\mathcal{S}|\{d^x, d^{x'}\}_i,\Delta_M)\mathcal{L}\left(\{d^x, d^{x'}\}_i|\Delta_M\right)\right)}{p(\mathcal{S}|\Delta_M)}. &(2.40)\end{aligned}$$

In the second line, the first term denotes the probability of detecting events in the data given a deviation Δ_M, and the second term $\mathcal{L}\left(\{d^x, d^{x'}\}_i|\Delta_M\right)$ is the likelihood on the data from the i-th event given the deviation Δ_M.

The parameters Δ_M do not affect the signal directly. Rather, they control the distribution of the BM signatures Δs, which are parametrized, for example, by α. Similarly, the GW source parameters θ are distributed according to the population hyperparameters Λ,

such as the maximum and minimum possible BH masses (see Sec. 4.1). This hierarchy is illustrated in Fig. 2.2.

The dependence structure in the figure appears when we marginalize over θ and α to obtain the likelihood conditioned on Δ_M. We can write the likelihood on the event data, including the GW source parameters θ with a prior $\Pi(\theta)$, and the dependence of any deviation on the GW source parameter, $p(\Delta_M|\theta)$, as

$$\mathcal{L}\left(\{d^x, d^{x'}\}_i|\Delta_M\right) = \int d\theta d\alpha \mathcal{L}\left(\{d^x, d^{x'}\}_i|\alpha, \theta\right) p\left(\alpha, |\theta, \Delta_M\right) \pi\left(\theta\right), \tag{2.41}$$

where α is the set of template coefficients for Δ_M. In the above, we have assumed that θ does not depend on Δ_M (there is no arrow going from Δ_M to θ in Fig. 2.2). The key point in our analysis is that we would like to model the dependence of α on both θ and Δ_M (the red dashed arrow in Fig. 2.2 and the term $p(\alpha|\theta, \Delta_M)$ in (2.41)). As is generally done in hierarchical models, we have assumed that the likelihood on the data of individual events depends on Δ_M only through the parameters α, so that $\mathcal{L}\left(\{d^x, d^{x'}\}_i|\alpha, \theta, \Delta_M\right) = \mathcal{L}\left(\{d^x, d^{x'}\}_i|\alpha, \theta\right)$.

We do not take into account the impact of BM effects on the source population (which would represent another term in (2.41) and another arrow between Δ_M and Λ in Fig. 2.2). In the most comprehensive model, we would also include the effect of cosmological models. This could, for example, be taken into account by adding the node Θ in 2.2. In this example, the cosmological parameters could depend on the BM model for example if the BM model is an extension to GR which modifies cosmological expansion, and it could, in turn affect the source population by changing source formation history.

The term in the denominator in Eq. 2.39 is the evidence, which we can write in terms of all possible events which are detectable above a matched filtering SNR ρ_* as

$$p(\mathcal{S}|\Delta_M) = \int_{\rho \geq \rho_*} d\{d^x(t)\} \int d\theta d\alpha p(\{d^x(t)\}|\theta, \alpha) p(\alpha|\theta, \Delta_M) \pi\left(\theta\right). \tag{2.42}$$

If the detector noise does not change with time, then the term $p(\{d^x(t)\}|\theta, \alpha)$ will not vary with time and only depend on the detectability of an event above ρ_*, which we usually denote by $p_{\rm det}(\theta, \alpha)$. If we assume any signal with a matched filtering SNR above ρ_* is detected, then Eq. (2.39) further simplifies. The term $\int p(\mathcal{S}|\{d^x, d^{x'}\}_i, \alpha)$ becomes unity. Putting all of this together, we can write the posterior on the parameters Δ_M as

$$\mathcal{P}(\Delta_M|\{d^x(t)\}) = \Pi(\Delta_M) \times \prod_{x, x'>x=1}^{N_{\rm det}} \prod_{i=1}^{N_{\rm obs}} \frac{\int d\theta d\alpha \mathcal{L}\left(\{d^x, d^{x'}\}_i|\theta, \alpha\right) p(\alpha|\theta, \Delta_M) \pi\left(\theta\right)}{p(\mathcal{S}|\Delta_M)}. \tag{2.43}$$

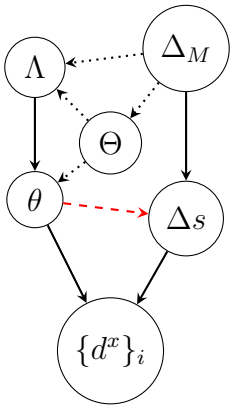


Figure 2.2: Schematic representation of the Hierarchical Bayesian model for the inference of a BM signature in the GW data. An arrow from node A to node B denotes that the prior on B depends on A. The physics underlying the BM signature is common to all events and determines the deviation Δs in individual events according to the parameters Δ_M, which should ultimately describe the underlying physics of the BM model (e.g the energy dimension of the leading EFT operator). Although the morphology of the deviation is not known (and must be modelled by the template functions), we expect it to vary consistently with the source parameters θ (e.g with a power law dependence on the mass of the BH in our EFT-motivated model). We include this dependence, which corresponds to the red dashed arrow, in our model. We then attempt to infer the deviation Δ_M from the data $\{d^x\}_i$ by marginalizing over the uncertainties in the intermediate parameters θ and α. The source parameters themselves are distributed according to the population hyperparameters Λ. For the most complete model, we would also include the effect of cosmological models, which could depend on the BM model and affect the source population.

This is the most general hierarchical Bayesian framework to search for a BM signature marginalizing over the source parameters uncertainties.

In this analysis, we perform the Bayesian estimation on the residual signal obtained around a set of best-fit model parameters $\theta_{\rm MLE}$ assuming the SM. This allows us to define the deviation Δ_M as a function of $\theta_{\rm MLE}$ so we may check any correlation between BM signature and source parameters. Searches around the best-fit can also help reduce the computational cost of performing the Bayesian analysis. However, the analysis pipeline can be easily modified to include the full Bayesian framework. The above equation around

a best-fit value can be simplified into

$$\mathcal{P}(\Delta_M|\{d(t)\}) = \Pi(\Delta_M) \prod_{x=1,y>x}^{N_{\rm det}} \prod_{i=1}^{N_{\rm obs}} \frac{\int p(\{d^x, d^{x'}\}_i|s(\theta_{\rm MLE}), \Delta_M) p(\Delta_M|\theta_{\rm MLE}) p(\theta_{\rm MLE}) d\theta_{\rm MLE}}{p(\mathcal{S}|\Delta_M)}, \tag{2.44}$$

where, $s(\theta_{\rm BF})$ is the GW signal for the set of best-fit parameters, $p(\theta_{\rm BF})$ is the posterior on the best-fit parameters obtained from the data assuming the SM.

The likelihood $p(\{d^x, d^{x'}\}_i|\theta, \alpha)$ can be written in terms of the CRPS as

$$p(\{d^x, d^{x'}\}_i|\theta, \alpha) = p(D^{xx'}(t)|\alpha). \tag{2.45}$$

If we further assume the likelihood to be Gaussian and there is no correlated noise, then it becomes

$$p(\{d^x, d^{x'}\}_i|\theta, \alpha) \propto \exp\left(- \int dt \frac{(D^{xx'}(t) - S(\theta, \alpha))^2}{2K_n^2(t)} \right), \tag{2.46}$$

where $D^{xx'}(t)$ can be calculated using Eq. (2.27) and the noise covariance matrix can be calculated using Eq. (2.32). In the presence of correlated noise $\mathcal{N}_c$ it can be included in the noise covariance matrix.

Though this method can detect the presence of any BM signature in the GW data, model-independent searches may fail to completely capture the structure of the deviation if the chosen template only partially overlaps with the BM signature. However, using the Bayesian framework proposed here, one can do a Bayesian model comparison for different BM scenarios and perform a tuned search for the model with higher Bayesian evidence.

Chapter 3

Demonstrating the SCoRe method

3.1 Application of SCoRe on a toy example for an unmodeled search

We now illustrate the SCoRe method by using the unmodeled power template to recover a toy model injection from simulated data. We describe the toy model and then discuss the appropriate choice of cross-correlation timescale. Using the SCoRe framework, we recover the injected value in the simulated data. Then, we perform the Bayesian analysis described in Sec. 2.4.4.

3.1.1 Generating mock data

As a toy model, we create simulated mock data by adding Gaussian noise realizations n^x over a simulated strain $s(t)$ as

$$d^x(t) = s^x(t) + n^x(t). \tag{3.1}$$

The strain is $s^x(t) \equiv s^x_{\rm SM}(t) + \Delta s^x_{\rm BM}$; it includes an SM signal $s_{\rm SM}(t)$ (e.g a currently available waveform model for a BBH merger in GR) and a BM signal $\Delta s_{\rm BM}$. The BM signal is modeled as $\Delta s_{\rm BM}(t) = b\frac{d\ln f_{\rm SM}(t)}{dt}$, with b as a free parameter that controls the strength of the BM signal, while $f_{\rm SM}(t)$ is the orbital frequency computed using the SM waveform model. The SM signal is the same for all events. It is computed using LALSuite [147] called through PyCBC [1] and the IMRPhenomD approximant [112, 126] for an equal mass, non-spinning, circular BBH merger, at a luminosity distance of 100 Mpc and the individual

masses are both set to $m = 5M_\odot$. A sampling rate of 16384Hz is used throughout this work to allow a more precise exploration of the effect of τ on the method. Both cross- and plus-polarizations are used to derive $f_{\rm SM}$, the orbital frequency. The plus-polarization is used as the SM signal $s_{\rm SM}$. We assume Gaussian, stationary noise and the same sensitivity for all detectors. Different events in each of the two distinct detectors are then simulated by drawing realizations n^x of the expected O4 noise sensitivity [21].[1]

We project the CRPS onto the unmodeled template given in (2.29). In the rest of the work, we implement the angular bracket average of Eq. (2.20) as a binned mean. This means that the operation $\langle\cdot\rangle_\tau$ returns a single value for each range of time of width τ, so that the CRPS has fewer data points than the strain. [2] Out of the template terms given in Eq. (2.29), we only use the linear term Z_1 for simplicity. [3] The toy model with the BM signal $\Delta s_{\rm BM}$ is constructed such that it perfectly overlaps with the template Z_1 to show how the recovery can happen for the best-case scenario. We expect that the template coefficient α_1 can recover the injected BM signal $\Delta s_{\rm BM}$ completely. Certainly, in reality, different BM theories will only have a partial projection on the template unless one performs a model-dependent search. In the future, we will explore different template choices to illustrate how they can project onto different BM theories. Theoretical efforts to produce waveforms in some such theories have been presented in e.g. [27, 31], and so have their impact on data analysis in modelled and unmodeled searches e.g. [198, 85].

We generate $N_{\rm GW}$ pairs of strain data as in Eq. (3.1) and attribute each strain to one of the two detectors x or x'. Examples of each component used to construct these data are shown in Fig. 3.1. We assume that the best-fit parameters are known exactly and that they are those used to generate $s_{\rm SM}(t)$. We therefore subtract $s_{\rm SM}$ from each of these strains to obtain $r^{x,x'}$. In real data, the error from estimating $\theta_{\rm MLE}$ needs to be accounted for both in the residual strains and the template, and we need to perform the marginalization described in Sec. 2.4.4.

Each pair of $r^{x,x'}$ is then cross-correlated as in Eq. (2.25) to obtain the CRPS, $D_i^{x,x'}$, where i labels events. We obtain $N_{\rm GW}$ residual time series that, for real data, would each be associated with a GW event. Examples of the CRPS are shown by orange lines in Fig. 3.2. An estimator $\hat{\alpha}_1$ is obtained for each time-series by projecting onto the template

[1] We have used the noise file aLIGOAdVO4T1800545 in PyCBC.

[2] One could also use a running mean, where each time sample is given a CRPS value instead of a binned mean value.

[3] Since we only use one template function, our template is orthogonal by construction.

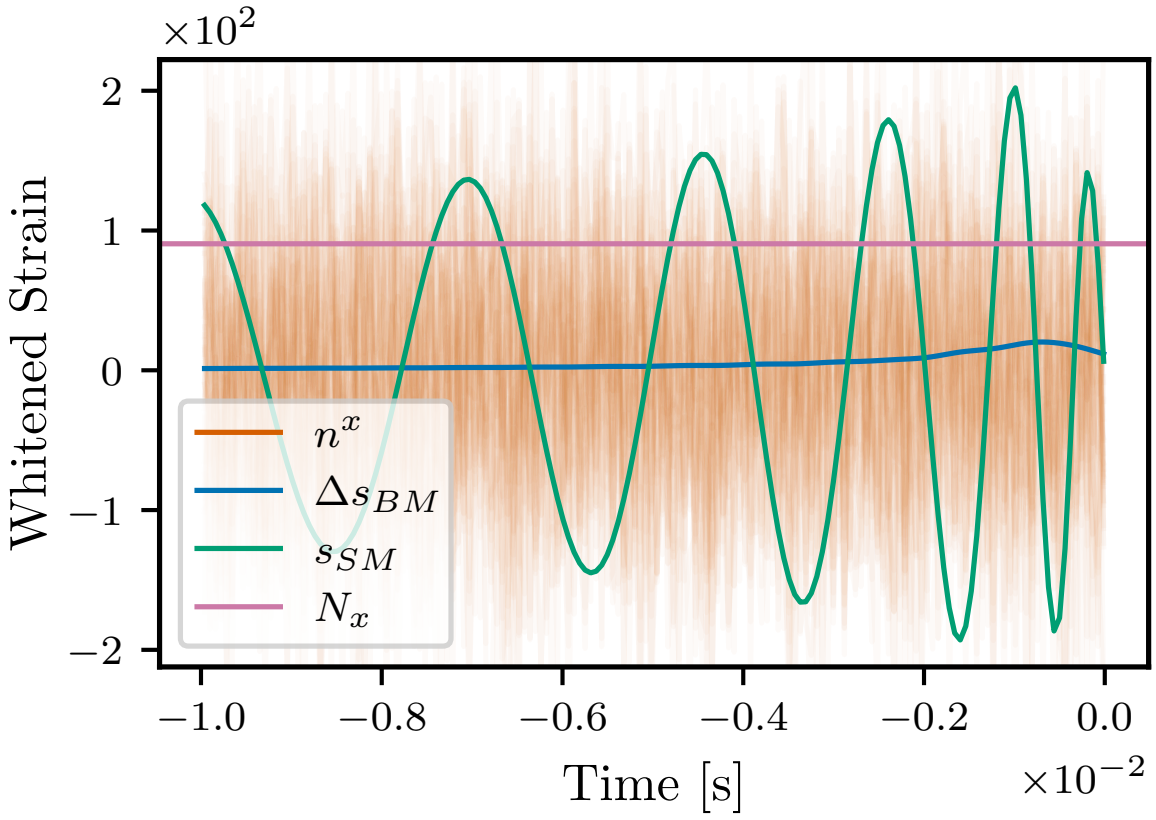


Figure 3.1: Example toy model data. We use the PyCBC software package to generate $s_{\rm SM}$, the waveform for a circular, non-spinning, equal mass BBH, with individual masses both equal to $5M_\odot$. This is plotted in green. We add onto it a BM signature, $\Delta s_{\rm BM}$ (blue line), that is proportional to the change in the orbital frequency logarithm ($\tilde{\alpha}_1 = 0.05$). It is normalized so that, for $\tilde{\alpha}_1 = 1$, the maximum amplitude reaches to the noise auto-correlation, N_x (purple line). Realizations of Gaussian stationary noise are added to $s_{\rm SM} + \Delta s_{\rm BM}$ to obtain different events. Some examples of noise realizations are plotted in orange.

.

according to Eq. (2.34). It is convenient to define the dimensionless quantities

$$\begin{aligned} \tilde{Z}_1 &= P^{-1} Z_1, \quad \text{such that} \int_{t_s}^{t_e} \tilde{Z}_1^2 dt = 1, \\ \tilde{\alpha}_1 &= \frac{\alpha_1}{\alpha_1^0}, \quad \alpha_1^0 = \frac{P N_x^2}{\max\left(\frac{d \ln f}{dt}\right)^2}, \end{aligned} \tag{3.2}$$

where α_1^0 is defined so that, when the maximum amplitude of $\Delta s_{\rm BM}$ is N_x, the projection of its cross-correlation onto $\tilde{Z}_1$ is $\tilde{\alpha}_1 = 1$. The normalization constant, P, measures the mean power per bin in the template function. The timescale τ over which the residual strains are cross-correlated is a free parameter during this procedure. We discuss the choice of τ in the next subsection.

3.1.2 Choice of τ

The definition of the CRPS signal in (2.27) depends on the choice of parameter τ. The choice of τ is a trade-off between the SNR and the the information content of the cross-correlation: larger τ values reduce the noise in the cross-correlation, but useful features of the signal may be lost in the averaging. Here we discuss what one should consider when choosing τ.

When τ is finite, the noise on the cross-correlation estimator in the limit of a small signal is

$$K_D^2 = \frac{1}{n_{\rm window}} K_n^2, \tag{3.3}$$

where $n_{\rm window}$ is the number of data points measured in the timescale τ. The advantage of taking the mean over a timescale τ is that $K_D \propto 1/\tau$, so, in the limit of large τ, the cross-correlation tends to be the residual signal (and correlated noise). On the other hand, as mentioned, some information is lost in the averaging over the timescale τ. This is illustrated in Fig. 3.3. The cross-correlation template $\tilde{Z}_1$ is computed from $s_{\rm SM}$ with different values of τ. As τ increases, the shape of $\tilde{Z}_1$ is qualitatively changed. By integrating over τ, we lose the ability to differentiate between BM models that give different template predictions below this timescale.

For a specific template, two choices of τ have equivalent signal content if no new physical behaviour arises at an intermediate timescale. The average power per bin, P, will be the same if they are equivalent. This quantity is plotted in Fig. 3.4 as a function of τ. For

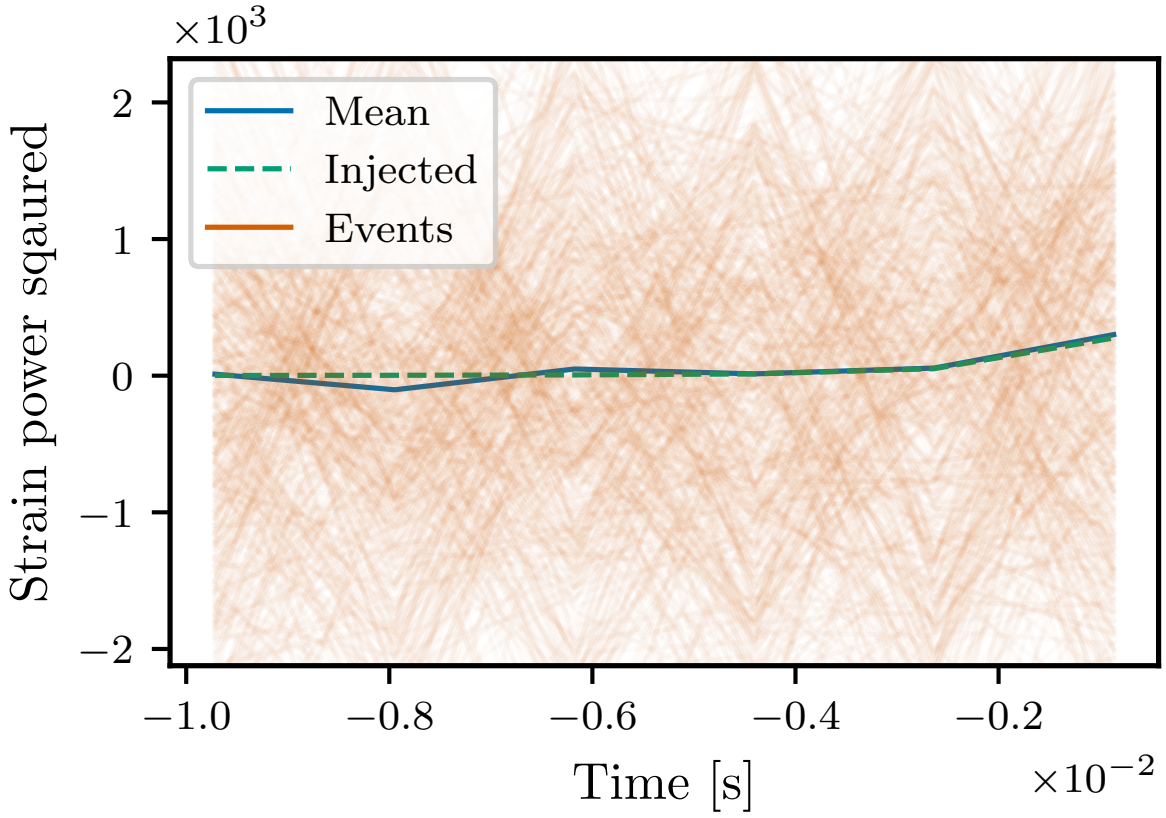


Figure 3.2: Residual data and injected BM signature cross-correlated over $\tau = 1.28 \times 10^{-3}$s. The blue line is the mean of the CRPS over 500 events, plotted in orange. It corresponds to the MLE value of $\tilde{\alpha}_1$ when projected onto the template. The dashed green line is the cross-correlation of $\Delta s_{\rm BM}$.

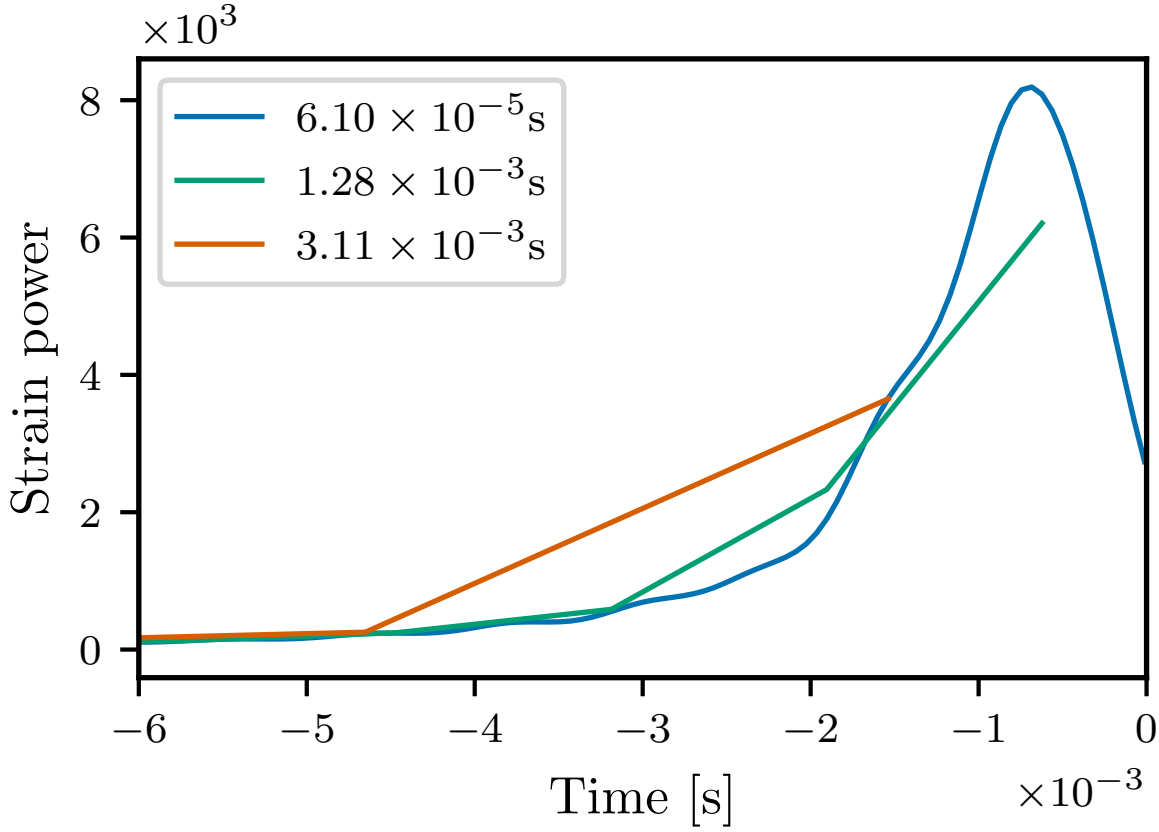


Figure 3.3: Cross-correlation template $\tilde{Z}_1$ for different cross-correlation timescales τ. The smallest timescale allowed by the sampling rate, $\tau = 6.10 \times 10^{-5}$ s, has features that are washed away as the timescale increases. With $\tau \in [0.8, 1.6] \times 10^{-3}s$, no new physical features appear and information remains the same as τ is increased. For timescales longer than 2.1×10^{-3} s, all the power is effectively concentrated in a single bin.

this example, at timescales shorter than 0.8×10^{-3} s, the mean power decreases as the "pulse" feature of the template seen in Fig. 3.3 is integrated out. For $\tau \in [0.8, 1.6] \times 10^{-3}$s, the mean power remains constant as the template functions resemble power laws, and a smaller τ does not add information. An example of a template with a timescale in this range is shown by the green line in Fig. 3.3 (obtained by averaging over $\tau = 1.28 \times 10^{-3}$ s). When averaging over timescales larger than $\tau \sim 2.1 \times 10^{-3}$ s, the BM signature's power concentrates in a single bin. Past this point, the mean power per bin, P, scales as $(\tau)^{-1/2}$.

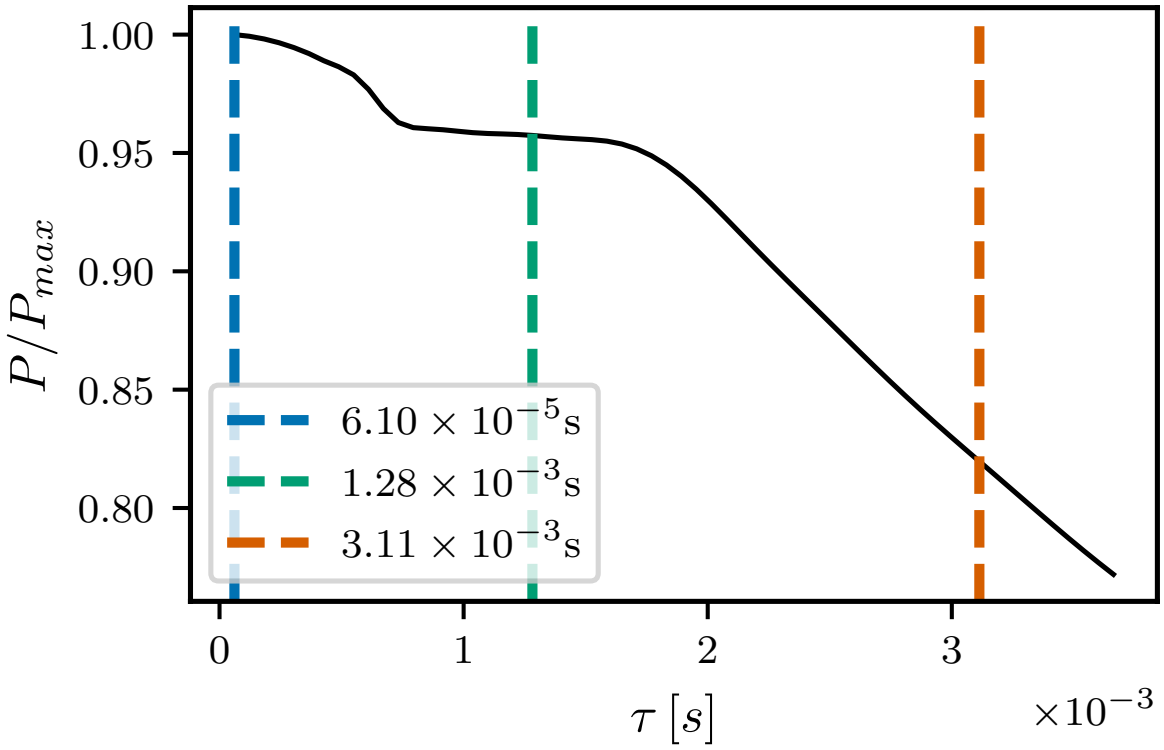


Figure 3.4: Template normalization factor (mean power per bin P) as τ is increased. The template with $\tau = 6.10 \times 10^{-5}$ s contains a pulse. As the pulse is washed away by the averaging, the mean power per bin decreases. Between $0.8 \times 10^{-3}s < \tau < 1.6 \times 10^{-3}s$, averaging over a greater τ does not change the shape of the template, and the mean power remains constant. At scales greater than 2.1×10^{-3} s a single bin contains the majority of the power, and the mean power scales as $\tau^{-1/2}$.

This exact evolution sequence of the mean power per bin P as a function of τ is specific

to our chosen template (2.29) and the SM waveform used for the computation. However, the criteria for choosing τ will be the same in all cases.

The first natural choice of τ corresponds to the maximum SNR, achieved when most of the power is concentrated in as small a bin as possible. This is determined by the τ where the mean power per bin, P, starts scaling as $\tau^{-1/2}$. This may not, however, correspond to the highest Bayes factor in favour of a BM signature.

If information about the structure of the BM signal is preferred over a higher SNR, then τ should be accordingly chosen. In our toy model, for our specific choice of template and SM waveform, to conserve information about the "chirp" part of the template, the τ value needs to be set to the rightmost point on the horizontal section of the P shown in Fig. 3.4, $\tau = 1.8 \times 10^{-3}$ s. In this case, it is not possible to preserve information about the pulse shape while still taking the cross-correlation, as one would need to set τ to the sampling interval. It may yet be possible to keep some benefits of taking the cross-correlation while not averaging over the pulse shape by letting the averaging timescale vary with time. For example, we may set τ to 1 over the sampling rate from $t = -10^{-3}$ s to $t = 0$, and set $\tau \in (0.8, 1, 6) \times 10^{-3}$ s for $t \in (-5, -1) \times 10^{-3}$ s to maximise noise reduction over the "chirp". Finally, we could average the rest of the time domain, where the CRPS is dominated by noise, into one bin ($t = (t_s, -5) \times 10^{-3}$ s).

In this section, we consider only a time-constant τ, which we set to the SNR-maximising value, $\tau = 1.8 \times 10^{-3}$ s. The cross-correlations plotted in Fig. 3.2 are computed over this timescale. This choice of τ is specific to this template function and best-fit source parameters, as the variation of the mean power P with τ will change for other choices of template and source parameters. Since the templates depend on the orbital frequency, we expect the choice of τ to vary (scale) with chirp mass for all choices of templates.

3.1.3 Bayesian inference of the injected signal

In this section, we use the Bayesian framework presented in Sec. 2.4.4 to combine events into one measurement of $\tilde{\alpha}_1$. We assume the source parameters are perfectly known to be $\tilde{\theta}_{\rm BF}$. Therefore, $p(\tilde{\theta}_{\rm BF}) = \delta(\theta_{\rm MLE} - \tilde{\theta}_{\rm BF})$, where $\delta(x)$ is the Dirac delta function. This assumption is made to show how this new method will work in the best-case scenarios. In reality, each estimated parameter will have an error, and one can marginalize the uncertainty as presented in Sec. 2.4.4. Furthermore, since we assume α_1 is unique for the given source parameters, $p(\alpha_1|\tilde{\theta}_{\rm BF}) = 1$. The posterior on $\tilde{\alpha}_1$ is then

$$\mathcal{P}\left(\tilde{\alpha}_1|\{d(t)\}\right) \propto \Pi(\tilde{\alpha}_1) \exp\left(-\frac{1}{2\tilde{K}_{\tilde{\alpha}}^2}\left(\tilde{\alpha}_1 - \tilde{\alpha}_{1,MLE}\right)^2\right), \tag{3.4}$$

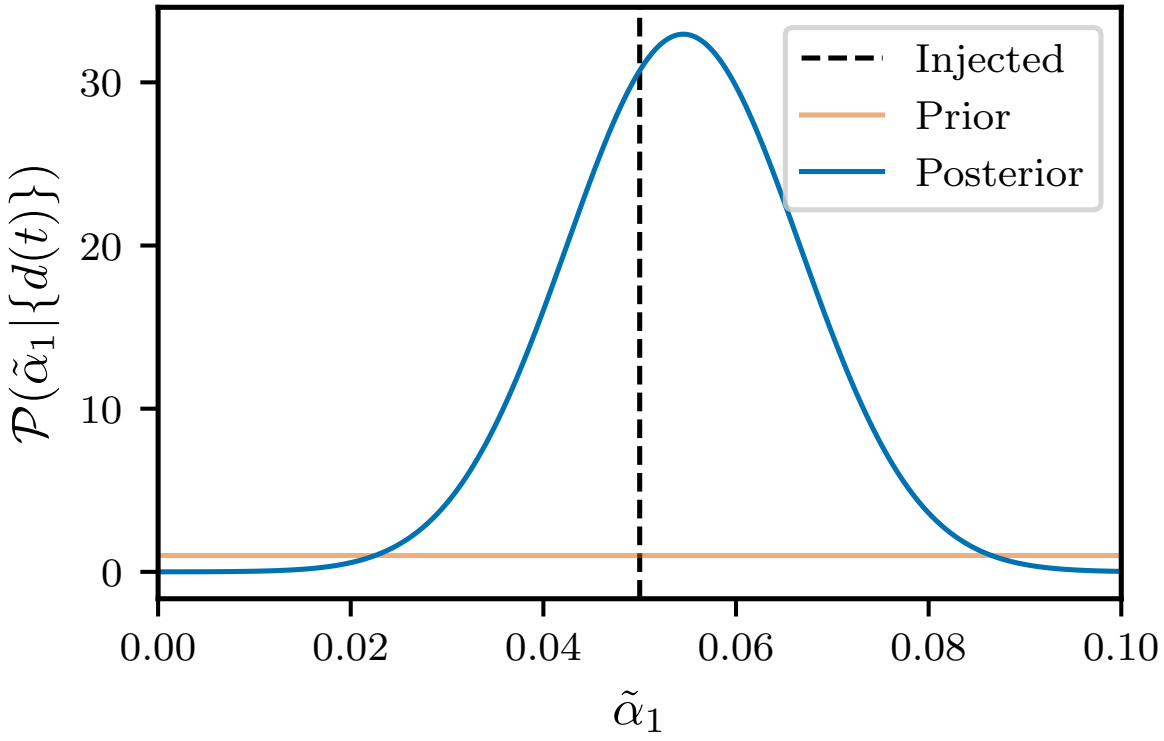


Figure 3.5: Posterior on $\tilde{\alpha}_1$ for $N_{\rm GW} = 500$, when the template function Z_1 is injected in Gaussian, stationary noise. We used a flat prior from 0 to 1, giving a Bayes factor of 773. The error on $\tilde{\alpha}$ is $\tilde{K}_{\tilde{\alpha}}$, the SNR for this measurement is 4.5.

where $\tilde{\alpha}_{1,MLE} = 1/(N_{\rm GW}\alpha_1^0)\sum_i^{N_{\rm GW}}\int_{t_{\rm s}}^{t_{\rm e}}\tilde{Z}_1 D_i dt$, and

$$\tilde{K}^2_{\tilde{\alpha}_1} = \frac{K^2_{\alpha_1}}{\left(a_1^0\right)^2 N_{\rm GW}}. \tag{3.5}$$

The likelihood is thus a Gaussian distribution with Maximum Likelihood Estimator (MLE) $\tilde{\alpha}_{1,\rm MLE}$ and variance $\tilde{K}^2_{\tilde{\alpha}_1}$. With our assumption, the MLE is the mean over events of the estimator $\hat{\alpha}_1$. Since the projection is linear, it corresponds to the projection of the mean CRPS, shown in blue in Fig. 3.2.

If a signal is correlated between detectors, its cross-correlation $S^{xx'}(t)$ must be positive. Our template function is positive, therefore so must be α_1 and $\tilde{\alpha}_1$. We choose a flat prior

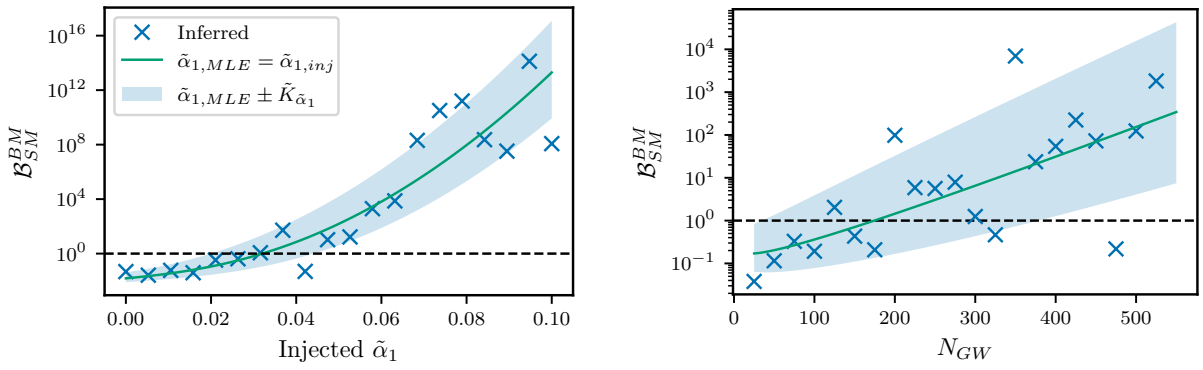


Figure 3.6: Bayes factor $\mathcal{B}^{\rm BM}_{\rm SM}$ in favor of a BM hypothesis over the SM hypothesis *left* for different values of $\tilde{\alpha}_{1,\rm inj}$ ($N_{\rm GW} = 500$), *right* for different $N_{\rm GW}$ ($\tilde{\alpha}_{1,\rm inj} = 5 \times 10^{-2}$). The solid green line indicates the case of perfect accuracy as a guide. The blue region covers one $\tilde{K}_\alpha$ deviations in the measured value of $\tilde{\alpha}_{1,\rm MLE}$. The SM waveform used is that of an equal mass BBH with individual mass $5M_\odot$.

on $\tilde{\alpha}_1$ ranging from 0 to $\tilde{\alpha}_{1,max}$, so that $\Pi(\tilde{\alpha}_1) = (\tilde{\alpha}_{1,max})^{-1}$. The posterior obtained from the events in Fig. 3.2, which have injection $\tilde{\alpha}_1 = 0.05$, is shown in Fig. 3.5. The prior used is set with $\tilde{\alpha}_{1,max} = 1$.

With this posterior, we can compare the SM hypothesis with the hypothesis of a BM signature by computing $\mathcal{B}^{\rm BM}_{\rm SM}$, the Bayes factor in favour of a BM signature being present instead of just the SM. Since the SM is recovered when the coefficient α_i is zero, we compute $\mathcal{B}^{\rm BM}_{\rm SM}$ as the Savage-Dickey density, which is the ratio of the prior to the posterior at $\tilde{\alpha}_1 = 0$:

$$\mathcal{B}^{\rm BM}_{\rm SM} = \frac{\Pi(0)}{P(\tilde{\alpha}_1 = 0|\{d(t)\})}. \tag{3.6}$$

The Savage-Dickey density can be computed directly in our toy model since the analytical form of the posterior in terms of $\tilde{\alpha}_{1,MLE}$, K_D^2, and $N_{\rm GW}$ is known. In fact, the expression for $\mathcal{B}^{\rm BM}_{\rm SM}$ can be written explicitly in terms of error functions

$$\begin{aligned}\mathcal{B}^{\rm BM}_{\rm SM} = \sqrt{\frac{\pi}{2}}\frac{\tilde{K}_{\tilde{\alpha}_1}}{\tilde{\alpha}_{1,\rm max}} \exp\left(-\frac{1}{2}\left(\frac{\tilde{\alpha}_{1,\rm MLE}}{\tilde{K}_{\tilde{\alpha}_1}}\right)^2\right) \times \\ \left(\mathrm{erf}\left(\frac{\tilde{\alpha}_{1,\rm MLE}}{\sqrt{2}\tilde{K}_{\tilde{\alpha}_1}}\right) - \mathrm{erf}\left(\frac{\tilde{\alpha}_{\rm MLE} - \tilde{\alpha}_{1,\rm max}}{\sqrt{2}\tilde{K}_{\tilde{\alpha}_1}}\right)\right),\end{aligned} \tag{3.7}$$

where $c = (1/2)\tilde{K}^2_{\tilde{\alpha}_1}$ and $\mathrm{erf}(x) = (2/\sqrt{\pi})\int_0^x \exp(-y^2)\,dy$. This can be computed numerically. We plot the dependence on $N_{\rm GW}$ and on the injected value of $\tilde{\alpha}_1$ in green on Fig. 3.6,

assuming a perfectly accurate measurement ($\tilde{\alpha}_{1,MLE} = \tilde{\alpha}_{1,\rm inj}$). In the left plot, the number of events is kept fixed at $N_{\rm GW} = 500$ as the injected value of $\tilde{\alpha}_1$ is varied, while on the right plot, $N_{\rm GW}$ is varied as $\tilde{\alpha}_{1,\rm inj}$ is kept fixed. We also plot values of $\tilde{\alpha}_{1,MLE}$ measured from realizations of the toy model data with crosses.

The value of $\Pi(0)$ can significantly change the recovered value of the Bayes factor. This is a manifestation of Occam's penalty [114]: a wider prior compared to the likelihood indicates a more constraining underlying hypothesis. The prior we choose has $\tilde{\alpha}_{1,max} = 1$. This maximum prior is quite large ($1 \gg \tilde{\alpha}_1 + \tilde{\Sigma}_{\tilde{\alpha}_1}$), and reducing it can increase the Bayes factor obtained without truncating most of the area under the likelihood. However, we choose it on the grounds that any yet undetected BM signature has to be smaller than the noise variance.

3.2 Application of SCoRe on a beyond GR model

3.2.1 Toy model EFT and numerical set-up

To explore our method in a realistic scenario—including inspiral, merger and ringdown—we construct a waveform model that captures key effects expected from an EFT extension of General Relativity under the assumption that the coupling scale is of the order (or below) that of the lightest BH scale.[4] The model accounts for (i) higher curvature corrections in the inspiraling regime can be captured at leading order by tidal effects, (ii) the merger transitions to a post-merger regime described by quasinormal modes for the BH described by such a theory and, importantly, that corrections scale with the mass of the system appropriately. To fix ideas and choose a convenient scaling so its dependence is sufficiently marked, we envision our system described by a Lagrangian $\mathcal{L} = R + l^4\mathcal{L}_{(6)}$, where $\mathcal{L}_{(6)}$ indicates the higher order corrections to the curvature, scaling in this example as M^{-4} (see e.g. [69, 46, 43, 52]). For modelling the merger, we follow [156] and construct an interpolating signal between inspiral and ringdown guided by the behaviour of null geodesics corresponding to the final BH. The main characteristics (mass and spin) of such a final BH can be estimated using a strategy similar to that given in [39, 125] as long as the general solution for a rotating BH in a given theory is known. For the inspiral regime, we use a simple effective one-body EOB model [38] with tidal interactions as in [109] (see also [65]) transitioning to the final BH at the innermost stable circular orbit (ISCO) frequency

[4] If such a scale is larger, as considered in [200], $\mathcal{O}(1)$ corrections to the GR gravitational Lagrangian are induced, rendering unclear what describes the regime with smaller scales (thus including merger and ringdown), as they would lie outside the EFT regime.

of the final BH. For concreteness, we focus on the equal mass, non-rotating, BBHs with no eccentricity. [5] Importantly, we note that for the theories described by the above Lagrangian, closed-form solutions are only known for slowly (or non) rotating scenarios, while the merger outcome should yield a BH with spin $a/M \approx 0.67$—with a small correction that also scales as M^{-4}. Without such a solution, the specific value of such correction can not be computed yet. However, we note that this correction is quite smaller than the correction to the horizon area (e.g. [46]) and so BH compaction is more affected than associated quasinormal modes. Last, gravitational radiation from this theory can be captured to leading order by the correction to the Quadrupole of the system; its the associated effect, in turn, can be accounted for in the stationary phase approximation to the waveform as discussed in [200]. Combining the above information, we "phenomenologically" account for dynamical departures in the theory by extrapolating from the slowly rotating case with the following assignments:

$$C = \frac{1}{2} - \frac{5}{16}\epsilon\,,\; k^T = \frac{1008}{25}\epsilon\,, \tag{3.8}$$

$$\delta\omega^R_{\rm QNM}/^{GR}\omega^R_{\rm QNM} = 1 + 0.45\epsilon, \tag{3.9}$$

$$\delta\omega^I_{\rm QNM}/^{GR}\omega^I_{\rm QNM} = 1 - 2.75\epsilon, \tag{3.10}$$

with C the compaction of each BH, k^T the tidal Love number, $\delta\omega$ the correction to QNMs and where $\epsilon = (M_*/M_T)^4$ and M_* a base scale which we take to be $= M_\odot = 1.5$ km. That is, the EFT is such that it assumes corrections to General Relativity, become $\mathcal{O}(1)$ at such length, thereby affecting the inspiral only at a subtle level.

3.2.2 Choice of template

We perform the same analysis as in Sec. 3.1 on the NR waveforms motivated by the EFT. The strain signal $s(t)$ is the full numerical waveform obtained with the source at $d_l = 100$ Mpc. We assume that the standard waveform corresponding to the best-fit parameters, $s_{\rm SM}(t)$, is the NR waveform obtained with the same source parameters in GR. These correspond to equal mass, non-spinning, quasi-circular BBHs with individual masses given by $m/M_\odot = 1, 2$ and 5.

In Sec. 3.1, the BM signature introduced was directly proportional to the template function, Z_1. As described in Sec. 2.4, more realistic residual signals such as the one

[5] As noted in [35] eccentricity can introduce a systematic bias in the identification of departures from GR—a potential issue that should be contemplated carefully in the analysis.

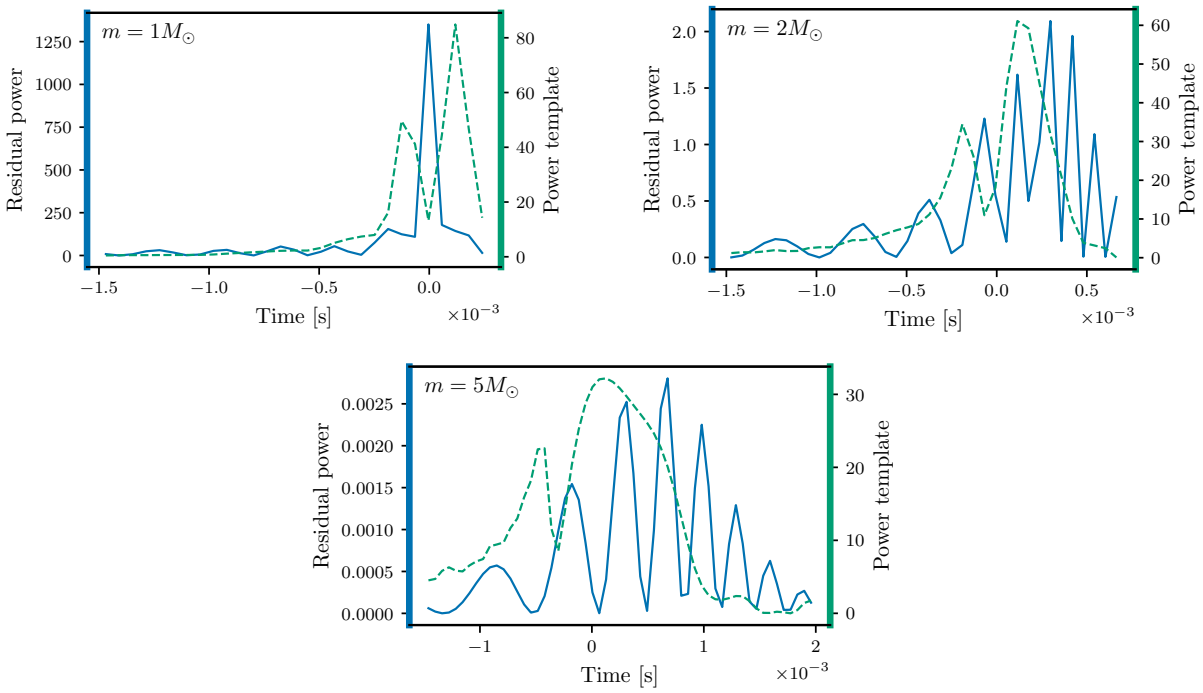


Figure 3.7: Residual power and template functions. The residual signals are obtained from subtracting the GR waveforms from the EFT waveforms with the same source parameters. They are plotted with blue, solid lines (left axis). The template functions $\tilde{Z}_1$ are computed from the GR signal using a value of τ equal to the sampling interval. They are plotted with dotted green lines (right axis). The template in Eq. (2.29) is unmodeled, and is not expected to match the actual signal at finite order, but it does capture the time interval over which the most power is present.

obtained from the EFT-inspired waveform will require a possibly infinite number of higher-order terms to be accurately described. The first order (normalized) template function $\tilde{Z}_1$ obtained from the GR waveforms using τ equal to the sampling interval is plotted for different m with dotted lines in Fig. 3.7. The power of the residual strains is plotted with full blue lines. Although the template functions do not track the short-scale time evolution, they capture the time interval over which residual power is present.

To choose the timescale over which to cross-correlate, we note that the power templates have two peaks. Ideally, one would integrate over the smaller feature seen in the template—in this case, the narrower of the peaks in power. This would be the feature seen around -0.2 to 0 milliseconds for $m = 1M_\odot$, -0.4 to 0 milliseconds for $m = 2M_\odot$, and from -0.6 to 0.2 milliseconds for $M = 5M_\odot$. However, for $m = 1M_\odot$ and $2M_\odot$, at the maximum currently available sampling rate (16384Hz), the residual power signals only span 2-5 sample points. We, therefore, choose to lose precision in favour of a higher SNR: averaging over both peaks (up to the value of τ at which the mean power per bin P scales as $\tau^{-1/2}$), which gives the highest SNR. This corresponds to integrating from around -0.25 to 0.25 milliseconds and from -0.5 to 0.5 milliseconds for $m = 1M_\odot$ and $2M_\odot$, respectively. The larger peak is smoother for $m = 5M_\odot$. As a result, integrating over both peaks (for example, from -1 to 1 milliseconds) does not give a larger SNR. For all masses, lower values of τ lead to a decrease in SNR.

The values of τ chosen for each mass are shown in Table 3.1. The coefficients obtained by projecting the residual power onto the template with the aforementioned values of τ are also shown in the table.

3.2.3 Recovery of injected signal

The values of $\tilde{\alpha}_1$ corresponding to the injected residual power are plotted with green crosses in Fig. 3.8. The values recovered from toy data with $N_{\rm GW} = 500$ are plotted with blue discs and error bars. For $m = 2$ and 5 $\mathrm{M}_\odot$, the recovered values are consistent with zero in comparison to the standard deviation $\tilde{K}_{\tilde{\alpha}_1}$, as indicated by a downward arrow on the error bars.

In this particular BM model, the power of the residual signal decreases with mass as m^{-8}. Regardless of the template chosen, the projection of the residual power onto it will also scale as m^{-8}. This is the case for the injected values of $\tilde{\alpha}_1$. The dotted orange line corresponds to a fit though these points with gradient m^{-8}—the template functions correctly capture the scaling of the NR waveform residuals. The fact that the template functions correctly capture the timescale and the power scaling of the BM signature is not

$\frac{m}{M_\odot}$	τ (s)	$\tilde{\alpha}_{1,\mathrm{inj}}$	$\tilde{\alpha}_{1,MLE}$	SNR	$\mathcal{B}^{\mathrm{BM}}_{\mathrm{SM}}$	FAR
1	4.27×10^{-4}	7.20×10^{-2}	1.02×10^{-1}	3.05	8.69	1.6×10^{-3}
2	1.22×10^{-3}	2.22×10^{-4}	1.66×10^{-2}	0.60	0.06	2.7×10^{-1}
5	1.22×10^{-3}	1.78×10^{-7}	5.47×10^{-3}	0.46	0.02	3.2×10^{-1}

Table 3.1: Projection coefficients of the injected BM signal and the recovered maximum likelihood estimation (MLE) of the NR EFT waveforms for 500 events. The values of τ are chosen so that the SNR is maximized and the smallest scale feature captured. They depend on the best-fit waveform. The drop in Bayes factor from $m = 1M_\odot$ to $m = 2, 5M_\odot$ is due to the mean recovered value of $\tilde{\alpha}_1$ moving within error range of $\tilde{\alpha}_1 = 0$. The FAR is computed as the probability of obtaining a value equal or larger than the $\tilde{\alpha}_1$ measured when there is no signal in the data (see Appendix A.2) for a Gaussian stationary noise.

trivial, as they are agnostic to the model and were not informed about the nature of the EFT used to simulate the NR waveforms. This is one of the salient aspects of the method `SCoRe`. For $m = 2$ and 5 $\mathrm{M}_\odot$, $\tilde{\alpha}_{1,\mathrm{inj}} \ll \tilde{K}_{\tilde{\alpha}}$. The Bayes factor for both these masses is inconsequential, and we cannot recover the scaling with mass.

We have assumed that the only term scaling with the source parameter we are investigating, which is mass in this example, is due to the BM signature so that the residual strain scales with a power k, where k captures the dependence of the BM signal, on the source parameters θ as $\Delta d \propto \theta^k$. For the EFT model considered here, $k = -4$ and θ is the source mass. In reality, the residual strain may contain contributions from unaccounted BM physics, waveform systematics, or a stealth bias, for example. These contributions may scale with the same source parameter as the BM signature but with a different dependence, such as $\theta^{k'}$. Then, depending on the value of k' relative to k and the range over which the value of θ is observed, one may still fail to recover the scaling with k even with large network SNR and $\tilde{K}_{\tilde{\alpha}} \ll \tilde{\alpha}_{1,\mathrm{inj}}$. In the case of a stealth bias, we would naïvely assume $k' = -4$. This is because, as the magnitude of the BM signature changes, so will the magnitude of its projection onto the SM manifold. More complicated dependence on the source parameters of the BM signature may arise, as noted in [169].

3.3 Discussion

In this chapter, we have illustrated the `SCoRe` method by applying it to a toy model and also to waveforms motivated by an EFT of gravity [69, 46, 43, 52]. In both cases, the injected residual power was mainly concentrated in the last few milliseconds (before the peak of the waveform) of a signal and the noise was Gaussian, stationary, and coloured according to the expected O4 PSD.

For the toy model, we showed how well different signal strengths could be recovered, as measured by the Bayes factor in favour of the presence of a BM signature, for varying levels of power injected and number of events combined.

The illustration of the method on the EFT-motivated NR waveforms constrained the BM signatures around zero and could not detect the injected signatures for the masses giving the smallest residual power ($m = 2, 5M_{\odot}$). However, the model-independent template we suggest for agnostic searches was successful in capturing the time range over which most of the residual power was emitted. It could also correctly infer the minute BM signal for $m = M_{\odot}$. As the search we performed used a model-independent template, it could not reproduce the exact structure of the residual signal, as expected. In this scenario, we suggest that once one has identified a promising result using the model-independent search, the templates should be refined. This can either be done by using a model-dependent template or by adding higher-order derivatives to the model-independent template functions.

The events used for the toy model all had the same source parameters, while for the EFT-motivated NR waveforms, we only varied the mass of the binary. In reality, sources are expected to be distributed over a large range in the space of source parameters. In addition, since the properties of the source and their astrophysical population will critically impact inference of BM signatures, as we generally expect BM signatures to vary across the source parameter space. In the next chapter, we will take into account astrophysical populations to obtain more realistic estimates of how well the method can infer the presence and structure of BM signatures.

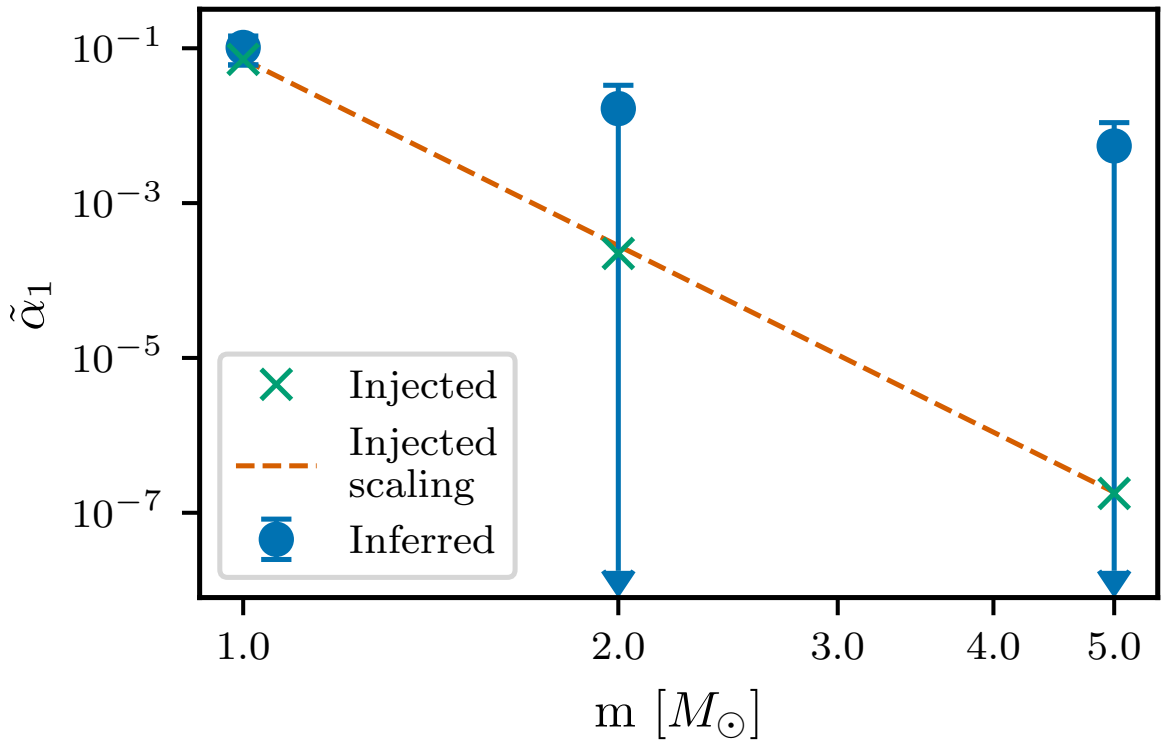


Figure 3.8: Injected and recovered values of $\tilde{\alpha}_1$. The projections of the actual residual signal on Z_1 are shown with green crosses. They correctly scale as m^{-8}, shown by the orange dotted line. The blue discs are values measured from toy data constructed with 500 events. The error $\tilde{K}_{\tilde{\alpha}}$, shown by the error bars, is several orders of magnitude larger than the injected values for $m = 2$ and 5 $\mathrm{M}_\odot$. The measurements for these masses are consistent with zero, as indicated by the downward porting arrows, and the scaling with m cannot be recovered.

Chapter 4

SCoRe forecast for 3G

BM signatures need not be identical for all events. However, if they originate from the same underlying BM effect (e.g beyond-GR effects, or a lower accuracy of the waveform model in certain regions of the parameter space), they should consistently vary with the source parameters. The last step of the SCoRe method is to combine the information from different events, assuming a dependence of the BM signature on the source parameters. In doing so, we model the dependence of the BM signature on the source parameters based on the BM scenario—for example, the power law scaling of the BM signature with the mass of the chirp studied in Sec. 3.2.

Two challenges arise when inferring the BM dependence on source parameters. First, degeneracies at the waveform level may exist between the source parameters and the BM signature. Second, observed GW events follow a distribution over source parameters. The most informative regions of parameter space for BM inference may not be covered enough by the observed events for the inference to give meaningful bounds.

In this chapter, we forecast the constraints that can be placed with SCoRe on the presence of a BM signature from a population of BBH mergers expected to be observed by a network of CE-like detectors. We first describe how the source parameters for the population are sampled. Then, we define a model for the BM waveform and its dependence on the source parameters. Finally, we use a Fisher forecast to estimate the constraint that can be placed on the BM deviation from with such a population of events.

4.1 GW source population

The goal in this section is to obtain a set of samples for the source parameters listed in Sec. 2.1.4. We sample from the probability distribution of BBH mergers in GR parameter space, which is proportional to the expected merger rate. The distribution of the intrinsic parameters (the masses and the spins) is both critical for the morphology of the waveform and rich in information about the formation of the binary system. The redshift/luminosity distance distribution is also important as it controls the sensitivity of the detectors to the sources while being tied to the astrophysics of star evolution. The other parameters (sky location, inclination, polarization, inclination, time and phase) are also important in determining the SNR of the event, and set the projection of the waveform on the different detectors via the antenna pattern functions. However, they are not as dependent on the underlying physics of the source.

We select our models for the merger rates with respect to each parameter following the analysis done in the LVK population papers [2]. Briefly, the redshift rate is assumed to track the Madau-Dickinson Star formation rate [151] at the same redshift; the mass merger rate is the Power-Law + Gaussian Peak from [208] with the best-fit parameters from [2]; and the spins are aligned, with effective spin sampled from a Gaussian distribution. The extrinsic parameters are sampled from uniform and isotropic (for sky localization) distributions. We assume a flat ΛCDM cosmology, with

$$H_0 = 70 \mathrm{kms}^{-1}\mathrm{Mpc}^{-1}, \quad \Omega_\Lambda = 0.7, \quad \text{and} \quad \Omega_m = 0.3. \tag{4.1}$$

As mentioned in Sec. 2.4.4, modifications to GR can also affect the source population. We did not account for this in this study.

Our samples were drawn from the distribution:

$$P(\vec{\theta}_{\mathrm{GR}}) = P\left(m_1, m_2\right) P\left(\chi_{\mathrm{eff}}\right) P(z) P\left(\vec{\theta}_{\mathrm{ext}}\right), \tag{4.2}$$

where $\vec{\theta}_{\mathrm{ext}}$ includes the sky location, the angle between the total angular momentum and the line of sight, the polarisation angle, geocentric time and the GW phase at merger. Table 4.1 summarises the models and parameters used in equation (4.2).

Note that we assume that the component masses and the effective spin are independent of each other. This may not be the case in reality, especially for dynamical formation channels. Indeed, evidence of a correlation between the mass ratio and the effective spin has been observed in the data [42]. Such an effect would be important to study when

recovering mass and/or spin dependent BM signatures. We sample from each independent distribution using inverse transform sampling.

Planned GW detectors, such as Cosmic Explorer (CE) [62] and the Einstein Telescope [150], are expected to detect events at rates in the order of $\mathcal{O}(10^5)\mathrm{yr}^{-1}$ [152]. We thus sample 10^5 events from the population model, and make the simple assumption that events with a signal-to-noise ratio $\rho > 8$ are detected.

In the next section, we describe the particular models for the redshift and masses.

Parameter	Model	Parameters
Redshift (z)	Madau-Dickinson SFR	$\gamma = 2.7$ $\kappa = 2.9$ $z_p = 1.9$
Primary mass (m_1)	Power-Law + Gaussian Peak	$\alpha = 3.4$ $m_{\mathrm{min}} = 5$ $m_{\mathrm{max}} = 100$ $\mu_m = 35$ $\sigma_m = 3.9$ $\lambda = 0.04$ $\delta_m = 4.8$
Secondary mass (m_2)	Conditional Power-Law	$\beta = 0.8$
Effective spin (χ_{eff})	Gaussian	$\mu_\chi = 0.06$ $\sigma_\chi = 0.12$

Table 4.1: Models and population parameters for the source parameters.

4.1.1 Redshift evolution

We assume that the GW source merger rate, measured per unit time and co-volume in the source frame, is proportional to the star formation rate at the same redshift:

$$\frac{dN_{\mathrm{GW}}}{dt_s dV_c} \propto \frac{dN_{\mathrm{SFR}}}{dt_s dV_c}. \tag{4.3}$$

This notably ignores two effects. The first is the dependence of the merger rate on metallicity. Specifically, BHs form more easily in low metallicity environments, and metallicity varies with redshift. In addition, there is a delay between BH formation and merger. This

delay can be accounted for by convolving the star formation rate with a delay time distribution, as is done, for example, in [123]. Although these effects are important for GW population analysis, the focus of this study is the effect of a realistic population on the recovery of BM, and we do not consider further precision in the population model to be necessary.

The right-hand side, the star formation rate, is a well-studied quantity. The Madau-Dickinson Star formation rate (modified from Equation 15 in [151]) is a fit to observations given by

$$\frac{dN_{\rm SFR}(z)}{dV_c dt_s} = R_0 \left(1+z\right)^{\gamma} \frac{1+(1+z_p)^{-(\gamma+\kappa)}}{1+\left(\frac{1+z}{1+z_p}\right)^{\gamma+\kappa}} {\rm M}_{\odot}{\rm yr}^{-1}{\rm Mpc}^{-3}, \tag{4.4}$$

where R_0 is the rate at $z = 0$. This phenomenological model accounts for a peak in the star formation rate, followed by a decline at high redshifts. The power indices γ and κ control the low redshift growth and large redshift decay, respectively. The pivot redshift, z_p, controls the peak of the star formation rate.

The rate is given per time in the source frame and per comoving volume. Converting to the relevant time at the detector and redshift rate, we get

$$\frac{dN_{\rm GW}}{dz dt_d} = \frac{1}{1+z}\left(\frac{dV_c}{dz}\right)^{-1} \frac{dN_{\rm GW}}{dV_c dt_s}. \tag{4.5}$$

When we convert from comoving volume to redshift rate, we make assumptions about the rate of cosmological acceleration. For a set of the cosmological parameters

$$\frac{dV_c}{dz} = 4\pi \left(\frac{c}{H_0}\right)^3 (1+z) \frac{1}{E(z)} \left(\int_0^{z'} \frac{dz'}{E(z')}\right)^2, \tag{4.6}$$

$$E(z) = \sqrt{\Omega_m (1+z)^3 + \Omega_\Lambda}, \tag{4.7}$$

see [108] for a review of cosmological measures, and (4.1) for the values used in this study.

The samples drawn for our study are shown in Figure 4.1, along with the model for the parameters in Table 4.1.

4.1.2 Mass spectrum

Here, we describe the phenomenology and the expression of the Power Law + Gaussian Peak model, introduced in [208]. This model assumes the primary mass of the BBH follows a power law with a maximum and minimum mass and a Gaussian-shaped peak in between.

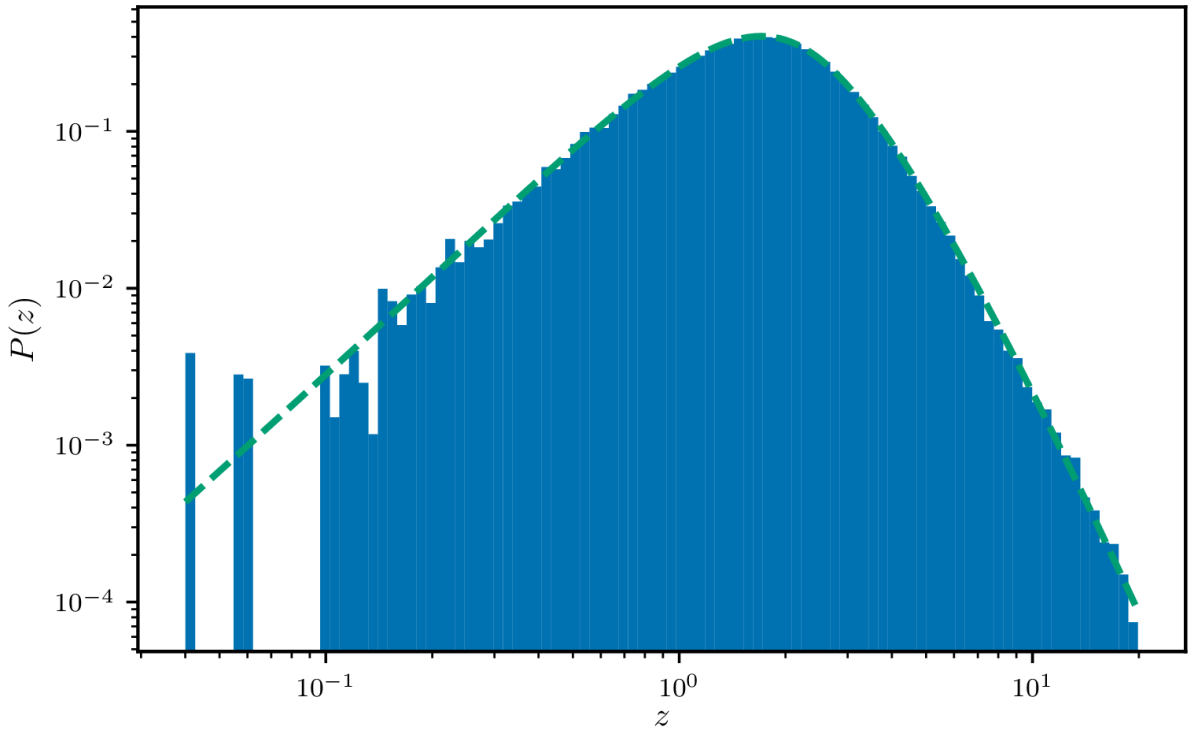


Figure 4.1: Samples drawn from the redshift model. The redshift distribution of BBH sources is assumed to track the star formation rate at the same redshift given by the Madau-Dickinson Star formation rate. This model increases as a power law with redshift, peaks around $z \sim 2$, and then decreases as a power law. The parameters used are listed in Table 4.1.

Just as when fitting the redshift dependence, we assume, as in [137], that the mass of the BHs tracks that of the stars that form them—the mass of stars is empirically known to follow a power law distribution (see [197], for example). Observations of galactic X-ray binaries [174] suggest a dearth of BHs under 5 $M_\odot$.

At the other end of the spectrum, there is theoretical motivation for a maximum mass of BHs formed from stellar collapse: the Pulsational Pair-Instability Supernova (PPSN) and the Pair-Instability Supernova (PISN) mechanisms [95, 96, 188, 235]. These instabilities happen when photons in the core of the star become energetic enough to produce electron-positron pairs, which reduces photon pressure and leads to shedding of mass through pulsating. The mass loss increases with the mass of the star until a stable point is formed

and leaves a remnant of around 40 $M_\odot$. All stars of masses 100-150 $M_\odot$ are expected to follow this channel, so we expect an accumulation ("graveyard") of BHs around this mass—hence a peak in the mass distribution. Past a certain mass, no remnant is expected. As a result, there is a maximum expected size of BHs formed from stellar collapse, which is around 70 $M_\odot$, although estimates vary.

The Power Law + Gaussian Peak model, introduced in [208], takes into account this phenomenology and uses the following model for the distribution of the primary mass m_1:

$$P(m_1|\alpha, m_{\min}, m_{\max}, \mu_m, \sigma_m, \lambda, \delta_m) \propto \big[\,(1-\lambda)\,P_{\rm pow}(m_1|\alpha, m_{\min}, m_{\max}) \tag{4.8}$$

$$+\,\lambda P_{\rm peak}\,(m_1|\mu_m, \sigma_m)\,\big]\,S(m_1, m_{\min}, \delta_m), \tag{4.9}$$

where $P_{\rm pow}$ is a power law with index α and cutoffs $m_{\min}$ and $m_{\max}$. The other component, $P_{\rm peak}$, is a Gaussian with mean at μ_m and standard deviation σ_m representing the PPSN graveyard. The mixture parameter λ determines the fraction of BHs formed through the PPSN channel.

A smoothing function S is applied at the lower end of the mass spectrum:

$$S(x, m_{\min}, \delta_m) \tag{4.10}$$

$$= \begin{cases} 0, & m < m_{\min}, \\ \left(\exp\left(\frac{\delta_m}{x-m_{\min}} + \frac{\delta_m}{x-m_{\min}-\delta_m}\right) + 1\right)^{-1}, & m_{\min} \leq m < m_{\min} + \delta_m, \\ 1, & m_{\min} + \delta_m \leq m. \end{cases} \tag{4.11}$$

The smaller component mass is drawn from a conditional power law, with equal mass ratios preferred:

$$P(m_2|m_1, m_{\min}, \delta_m) \tag{4.12}$$

$$\propto \begin{cases} \left(\frac{m_2}{m_1}\right)^\beta S(m_2, m_{\min}, \delta_m), & m_2 < m_1, \\ 0, & \text{otherwise}, \end{cases} \tag{4.13}$$

where the index β is dependent on the binary formation channel [137].

The samples drawn for our study are shown in Figure 4.2, along with the model for the parameters in Table 4.1.

4.1.3 Spin distribution

The effective spin is sampled over the range $\chi_{\rm eff} \in [-1, 1]$ from a Gaussian with mean μ_χ and standard deviation σ_χ :

$$P(\chi_{\rm eff}|q, \mu_\chi, \sigma_\chi) \propto \exp\left[-\frac{\left(\chi_{\rm eff} - \mu_\chi\right)^2}{2\sigma_\chi^2}\right], \tag{4.14}$$

and we use the MLE values found in [2]: $\mu_\chi = 0.06$, $\sigma_\chi = 0.12$. This is simply a fit of the currently available data, with evidence for preferentially aligned spins.

BM signatures can depend on mass and spin (see, for example, the Spin Quadrupole term in [138]). Following [42], one could model a correlation between mass ratio and effective spin by letting μ_χ and σ_χ depend on the mass ratio:

$$\mu_\chi(\mu_{\chi,0}, \alpha, q) = \mu_{\chi,0} + \alpha(q - 0.5), \tag{4.15}$$
$$\log_{10}\sigma_\chi(\sigma_{\chi,0}, \beta, q) = \log_{10}\sigma_{\chi,0} + \beta(q - 0.5), \tag{4.16}$$

and use the MLE values found in the data using this model: $\mu_{\chi,0} = 0.19$, $\log_{10}\sigma_{\chi,0} = -1.06$ $\alpha = -0.46$, $\beta = -0.83$. We did not include this effect in our study for brevity, but the impact of a correlation between mass ratio and effective spin on recovering a BM model that is mass and/or spin dependent is an interesting avenue for future work.

4.2 CRPS model

4.2.1 BM waveform model

In this section, we define the waveform model we use as our true signal $s(t)$ and the dependence of the BM signature on the source parameters. We write the true signal $s(t)$, including BM signature, as a deformation of the SM polarizations in amplitude and phase:

$$h_{\rm BM,\times,+} = h_{\rm SM,\times,+}\left(1 + \delta A\right)\exp\left(i\delta\phi\right), \tag{4.17}$$

where both the phase deviation $\delta\phi$ and the amplitude deviation δA can depend on the source parameters. We assume that the deviation is the same in both polarizations.

The `IMRPhenomPv2_NRTidalv2` model gives us the polarizations $h_{\mathrm{BM},\times,+}$. The signal measured at the detectors is given by

$$d_x = F_x^+ h_{\mathrm{BM},+} + F_x^\times h_{\mathrm{BM},\times} + n_x, \tag{4.18}$$

where $F_x^{+,\times}$ are the antenna patterns for the detector x. To compute $F_x^{+,\times}$, we use two fiducial CE-like detector locations from [36]. One is situated in New South Wales, Australia, and the other in Idaho, USA. Since we focus on ground-based detection, the time variation in the antenna pattern due to the Earth's rotation is negligible. The details of the antenna pattern computations can be found in [121]. The PSD giving the noise n_x is taken to be that of the 40km CE design from [207].

4.2.2 BM source dependence model

Motivated by EFTs of gravity where the BM signature can be captured to leading order by the tidal effects, we set h_{SM} to be the waveform from a BBH merger in GR, while h_{BM} is the waveform with the same source parameters but a non-zero tidal deformability. To compute h_{BM}, we use the `IMRPhenomPv2_NRTidalv2` model [72, 73]. Schematically, the phase deviation is given by

$$\delta\phi = -\beta \frac{M^2}{m_1 m_2} F(t), \tag{4.19}$$

where M is the total mass, m_1 and m_2 are the component masses, and $F(t)$ is a function of time, fitted to NR simulations. The parameter β, which in the `IMRPhenomPv2_NRTidalv2` model is the mass weighted dimensionless tidal deformability parametrizes the BM signature.

We model source parameters dependence of β based on the EFT model of gravity [41, 76, 74, 75, 89, 228]. As discussed in Sec. 1.1.2, general relativity can be seen as the leading order term in an EFT expansion, with higher order terms suppressed by a cutoff scale E_{UV}. The effective action which gives Einstein-Hilbert gravity (1.1) at low energies is

$$\mathcal{L}_{\mathrm{EFT}} = \frac{M_{\mathrm{Pl}}^2}{2}\sqrt{-g}\left(R + \frac{\mathcal{L}_4}{E_{\mathrm{UV}}^2} + \frac{\mathcal{L}_6}{E_{\mathrm{UV}}^4} + \frac{\mathcal{L}_8}{E_{\mathrm{UV}}^6} + \cdots\right), \tag{4.20}$$

where M_{Pl} is the Planck mass, R is the Ricci scalar, and E_{UV} is the cutoff scale of the EFT. The terms $\mathcal{L}_D$ represent all possible dimension D operators constructed with Riemann

tensors and their covariant derivatives (so that the theory is diffeomorphism invariant). The effects from terms of dimension D grow as $(E/E_{\rm UV})^D$, where E is the energy scale of the process—the scale set by the curvature scale of the merging binary.

Motivated by this observation, we model the BM signature as decaying as a power law of the chirp mass (as a measure of curvature) of the source. We let

$$\beta = \beta_0 \left(\mathcal{M}_c/M_0\right)^{-D}, \tag{4.21}$$

where $M_0 = 5M_\odot$, $\mathcal{M}_c$ is the chirp mass of the source, and β_0 is the size of the deviation at M_0. In this model model, $\Delta_M = (\beta_0, D)$ (the model parameters, see Sec. 2.4.4), and the residual is given by

$$\Delta s^{x,x'} = h_{\rm SM}^{x,x'} \left(\exp\left(i\delta\phi\right) + \delta A \exp\left(i\delta\phi\right) - 1\right). \tag{4.22}$$

The terms in the brackets will contribute a factor of $\mathcal{M}_c^{-D}$ to first order. Since the time-domain strain in GR scales as $h \propto \mathcal{M}_c^{5/4}$, the $h_{\rm SM}$ term will scale as $\mathcal{M}_c^{5/4}$, and the residual will scale as $\mathcal{M}_c^{5/4-D}$.

4.2.3 CRPS computation

As discussed in Sec. 2.4.4, the `SCoRe` framework can be agnostic to the form of the BM signature—for example, the "chirp-like" template (2.29) can be used to search for a general BM signature that causes a change in the rate of orbital energy dissipated.

To perform a forecast, however, we only compute the CRPS projection coefficient (2.34) computed with the template $Z(t)$ given by the exact waveform model (4.17); in essence, we consider the best-case scenario for the choice of template. Eq. (2.34) then gives

$$\alpha = \left(\int dt \frac{1}{K_D^2} Z(t)^2\right)^{-1/2}, \tag{4.23}$$

$$Z(t) = \left\langle \Delta s^x \Delta s^{x'} \right\rangle_\tau, \tag{4.24}$$

where Δs^x is defined in Eq. (4.22), K_D is computed as in Eq. (2.37) using the PSD in [207], and we use a constant $\tau = 6$ms for the cross-correlation window.

Assuming that there is a dependence of the BM signature on the source parameters does not depend on time, α (which is a measure of mean cross-correlated power) will scale

as $\alpha \propto \beta^2$, to leading order in β. For the model (4.21), we expect, when β is small:

$$\alpha \propto \mathcal{M}_c^{\gamma}, \tag{4.25}$$

$$\gamma = \frac{5}{2} - 2D. \tag{4.26}$$

The waveform, and therefore α, also depend on the other source parameters. For a population of events, the variation in these parameters will lead to a random spread in the residuals and, therefore, in the value of α. We examine the effects of this variation in Sec. 4.3.1.

4.2.4 Fisher Matrix Estimation

The Bayesian inference for the BM signature Δ_M as described in Sec. 2.4.4 requires the computation of the likelihood on each event, as well as the prior on the source parameters. For 15 parameters, this is computationally expensive to evaluate, and the problem scales for a population of events. Since, in this study, we only aim to forecast the precision of the framework, we can use a Fisher matrix forecast as a cheap approximation for the results valid in the limit of large SNR. We will introduce the Fisher matrix formalism in this section, but refer the reader to [98, 219] for examples and discussion about its use in GW parameter estimation.

Here, we briefly review the Fisher matrix estimation. Given a likelihood $\mathcal{L}(d|\theta, \alpha)$, where d is the data, θ are parameters to be estimated, we can expand the log likelihood around the MLE and find

$$\ln \mathcal{L}(d|\theta) = \ln \mathcal{L}(d|\theta_{\rm MLE}) + \frac{1}{2} (\theta - \theta_{\rm MLE})^i (\theta - \theta_{\rm MLE})^j \left(\frac{\partial^2 \ln \mathcal{L}}{\partial \theta^i \partial \theta^j} \right) \Bigg|_{\theta_{\rm MLE}} + \mathcal{O}(\theta^3), \tag{4.27}$$

where the linear, first derivative term vanishes at the MLE. When taking the expectation value over possible realizations of the data, the expectation of the MLE is the true value of the parameters. The difference $\Delta\theta = \theta - \theta_{\rm MLE=True}$ is then the error on the measurement.

The first term in the expansion is a constant and contributes to the normalization of the likelihood. Then, we see that to second order in $\Delta\theta$, the likelihood is a Gaussian with covariance given by

$$\Gamma_{ij} = -E \left[\left(\frac{\partial^2 \ln \mathcal{L}}{\partial \theta^i \partial \theta^j} \right) \Bigg|^{-1}_{\theta_{\rm MLE}} \right], \tag{4.28}$$

which is the Fisher matrix.

In the case of parameter estimation for a GW signal, the likelihood is as defined in (2.9) for Gaussian noise. Taking the second derivative of the log-likelihood, we find the Fisher matrix:

$$\ln p(d|\theta) = -\frac{1}{2}\left(d - h(\theta)|d - h(\theta)\right) \tag{4.29}$$

$$\Gamma_{ij} = -\frac{\partial^2 \ln p\left(d|\theta\right)}{\partial\theta^i \partial\theta^j} = \left(\frac{\partial h}{\partial\theta^i}\middle|\frac{\partial h}{\partial\theta^j}\right) - \left(\frac{\partial^2 h}{\partial\theta^i\partial\theta^j}\middle|h - d\right), \tag{4.30}$$

and, in the limit of large SNR, the second term is negligible compared to the first.

We, therefore, approximate the likelihood $\mathcal{L}\left(d|\theta,\alpha\right)$ as a Gaussian with covariance given by the Fisher matrix on the fiducial source parameters θ, sampled as described in Sec. 4.1, and on α, whose variance variance is 1 by definition.

As a note, the error caused by either a specific noise realization or a stealth bias can be estimated to first order in $\Delta\theta$. Starting with the definition of the MLE and substituting the expression for the data containing a noise realisation n and a BM signature Δs:

$$\left(\partial_i h\left(\theta_{\rm MLE}\right)\middle|h\left(\theta_{\rm MLE}\right) - d\right) = 0, \tag{4.31}$$

$$= -\left(\partial_i h\left(\theta_{\rm MLE}\right)\middle|\Delta\theta^j\partial_j h\left(\theta_{\rm MLE}\right) + \Delta s + n\right), \tag{4.32}$$

$$\therefore \Delta\theta^i\left(\partial_i h\left(\theta_{\rm MLE}\right)\middle|\partial_j h\left(\theta_{\rm MLE}\right)\right) = -\left(\partial_i h\left(\theta_{\rm MLE}\right)\middle|\Delta s + n\right) \tag{4.33}$$

$$\Delta\theta^i = \left(\Gamma^{-1}\right)^{ij}\left(\partial_i h\left(\theta_{\rm MLE}\right)\middle|\Delta s + n\right). \tag{4.34}$$

Including this term did not change our results. This is mostly due to the small error on the chirp mass in CE detectors $\left(\frac{\Delta\mathcal{M}_c}{\mathcal{M}_c}\right) \approx 10^{-3}$ [113]. Since we are not including any scatter due to noise or degeneracy between the BM parameters and the model, we assume that the MLE is the true value and do not take the expectation value over the data.

4.3 Forecast results

With the catalogue of events generated, we check the effect of two factors on the recovery of the mean cross-correlated power α. First, from (4.23), the dependence of the BM signature

parameter β on the chirp mass is only reproduced by α to leading order. How does this affect the scaling in α that can be measured? Second, there will be a spread in the values of α due to the variation in the other source parameters. What is the precision with which the BM signature can be detected, given this spread (and the error due to the noise in the detectors)?

4.3.1 Cross-correlated power scaling

In this section, we show how the injected dependence of β on the chirp mass can be recovered with the cross-correlated power α.

Consider first the case where β is small for all events. $\beta_0 = 5$, $D = 3$, and assign a value of β to each event in the catalog according to (4.21) and then compute α according to (4.23). In the figure, we plot the We show the α computed as a function of the chirp mass in the top panel of Fig. 4.3.1. The spread is due to the variation in the source parameters other than the chirp mass, and not to the noise in the detectors. The waveform, and hence the residuals, is a function of the products of the various source parameters. By the central limit theorem, the distribution in α for a given chirp mass is therefore a log-normal distribution.

We therefore fit the α values in log space with a linear model, which we show as a solid line in the Figure. Besides the α for each event, we also plot the linear fit in log space, as well as a dashed line showing the scaling with the same intercept as the fit, but with the expected scaling $\alpha \propto \mathcal{M}_C^{\frac{5}{2}-2D}$. Fitting the α values in Fig. 4.3.1 with a linear Gaussian model in log space, the expected γ from Eq. (4.25) is recovered to within 0.1. For larger values of β_0, the scaling breaks down. This is illustrated in Fig. 4.3.1 for $\beta_0 = 660, D = 6$.

4.3.2 BM signature detection

In this section, we use Fisher estimation as described in Sec. 4.2.4 to compute the likelihood on the source parameters and BM signature. We then show how γ and α_0 can be recovered in a Bayesian framework where the source parameters are marginalised, and the precision with which a BM signature can be constrained with `SCoRe` for this chirp mass dependent model.

With assume the likelihood $\mathcal{L}\left(\{d^x, d^{x'}\}_i|\theta, \alpha\right)$ in (2.43) is Gaussian with mean at the true value of the source parameters and zero for α. The covariance matrix is given by the Fisher matrix (4.28), with the parameters other than α and the chirp mass marginalised

over. For each value of α_0 and γ, We marginalise over α and γ over a grid by estting $p(\alpha|\gamma,\theta) = \delta(\alpha - \alpha_0 \mathcal{M}_c^\gamma)$. The prior on θ for each event is set to be uniform in an interval of 10 standard deviations around the true value (this is to reduce computational cost, as ideally).

The results are shown in Fig. 4.4. The curves on the left-hand plot show the upper limit of the 68 % credible interval on α_0, as representation of the constraint the method can put on the model. The right-hand plot shows the corresponding posteriors marginalised over γ.

The constraint scale as $N^{-1/2}$, as expected from SNR arguments. The more negative values of γ, corresponding to higher dimensional operators, the weaker the bound that can be found. This is also expected, since the higher the dimension of the operator, the steeper the fall with chirp mass in measurable power associated with the BM signature.

4.4 Discussion

This chapter aimed to forecast the recovery of a BM signature from a population of BBH mergers observed by a network of 3G detectors using the `SCoRe` method. We described the population of events that we used for the forecast as well as the model for the BM signature. Crucially, we assumed a dependence of the BM signature on the chirp mass of the source, motivated by the EFT of gravity considerations. We then showed the precision of the constraints that can be placed on the presence of a BM signature from the population of events, assuming this dependence.

We illustrated, notably, how the CRPS fails to reproduce the scaling with chirp mass beyond the regime of small BM signatures. This result is expected, as the framework assumes small residual. We also showed that the precision of the constraints on the BM signature scales as $N^{-1/2}$, as expected from SNR arguments, and that higher dimensional operators are harder to constrain due to the steep power law fall resulting in fewer events that contribute to measurable power.

A key idea of this chapter is that assumptions on the dependence of BM signatures on source parameters, particularly EFT motivates mass dependence can be folded in tests of the SM. We started to explore how this dependence can be recovered with a population of events, but left several avenues open for future work. These include correlations between mass and spin, which could play a role in recovering BM signatures that are dependent on either parameter. Which parts of the parameter space (e.g which mass ranges) are most informative in the recovery of the BM signature would also be valuable insight. Finally,

a significant aspect of the `SCoRe` method is the ability to adopt degrees of agnosticism in choosing templates used on the CRPS. It would be interesting to explore how the choice of templates affects the recovery of the BM signature.

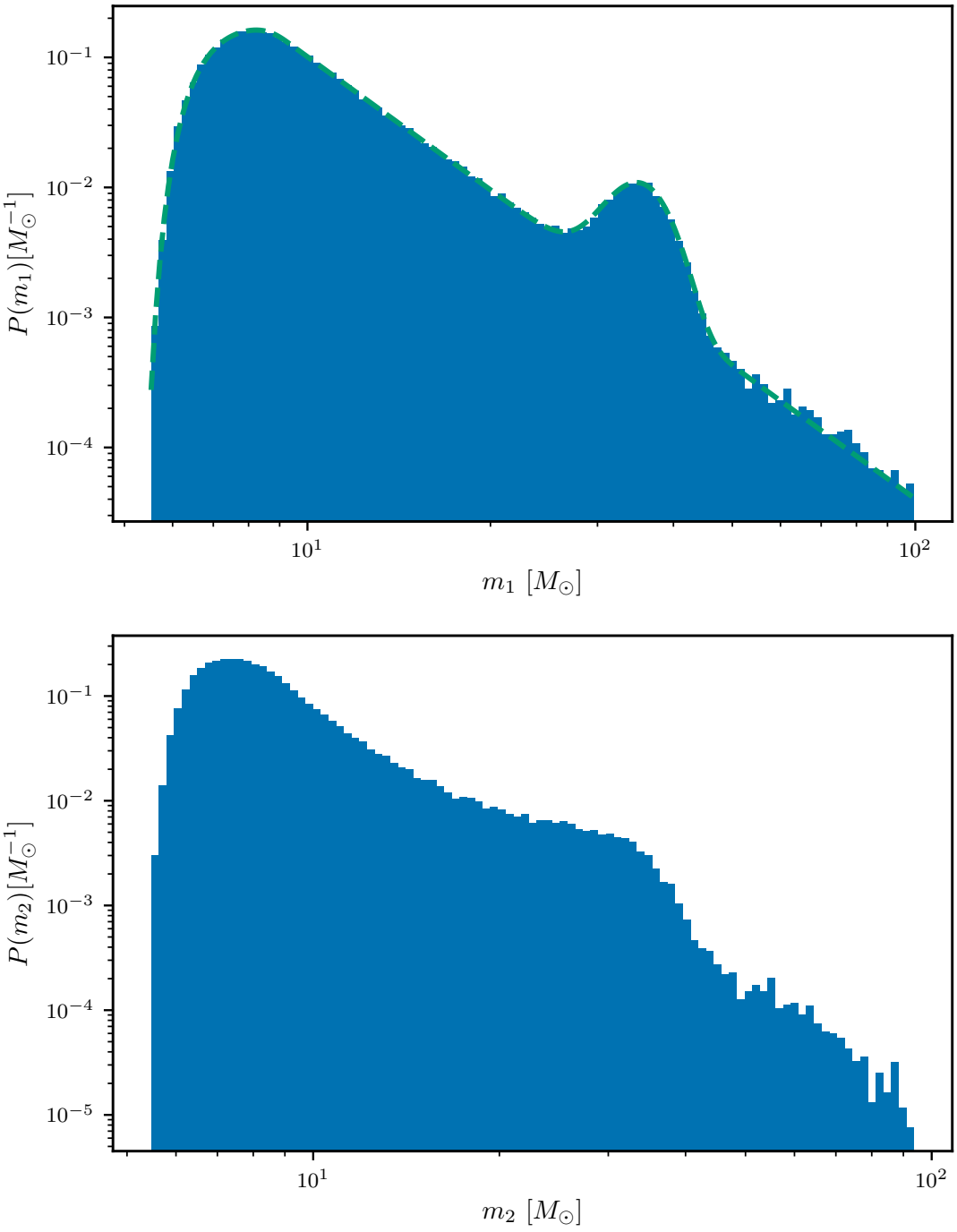
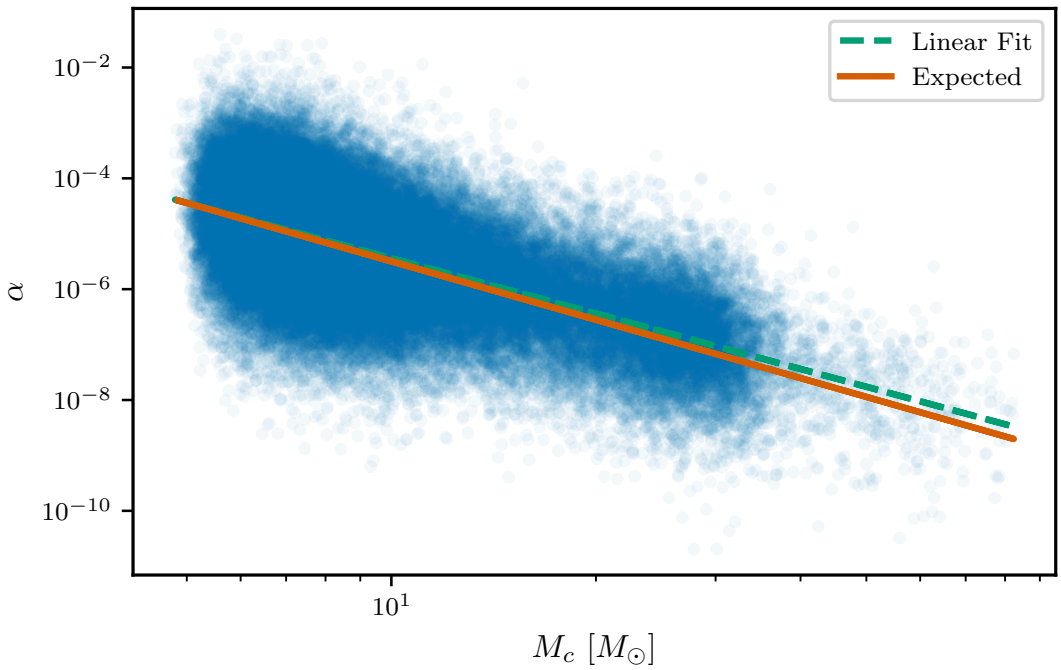


Figure 4.2: Samples drawn from the mass model (Power Law + Gaussian Peak) for the primary (**top**) and secondary (**bottom**) masses. The mass model is a power law (similar to the observed initial mass function of stars), with maximum mass set by the PISN scale, a Gaussian peak at the PPSN graveyard, and a tapering off at low masses to reproduce the observed dearth of low mass BHs. The parameters used are listed in Table 4.1.


Linear Fit
Expected
10^{-2}
10^{-4}
10^{-6}
10^{-8}
10^{-10}
α
10^{1}
$M_c\ [M_\odot]$

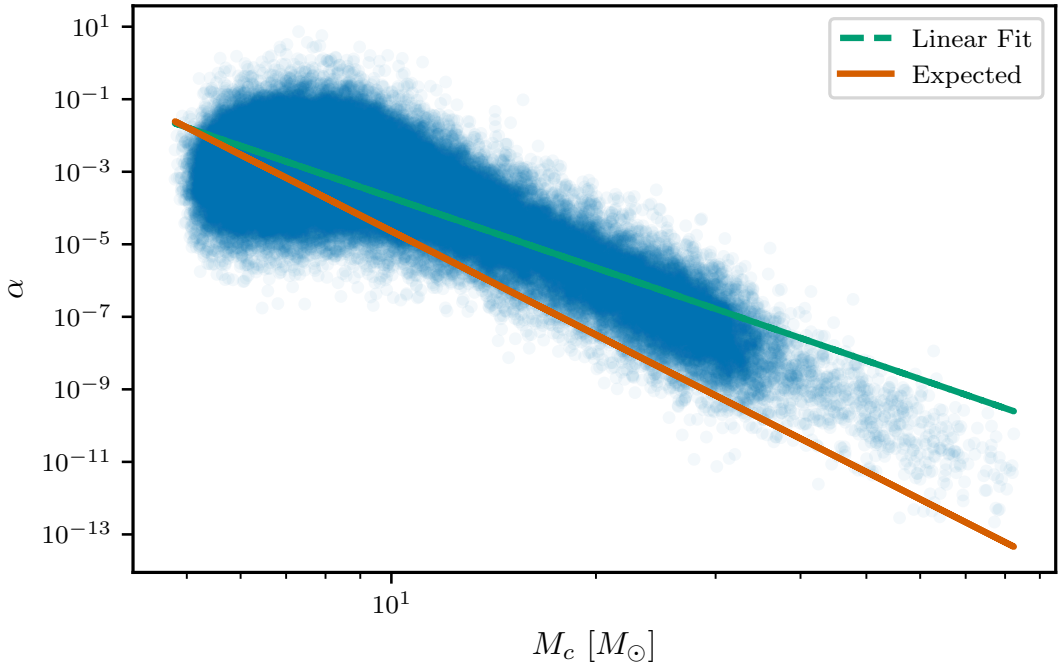

Linear Fit
Expected
10^{1}
10^{-1}
10^{-3}
10^{-5}
10^{-7}
10^{-9}
10^{-11}
10^{-13}
α
10^{1}
$M_c\ [M_\odot]$

Figure 4.3: (Opposite page) The cross-correlated power α as a function of the chirp mass $\mathcal{M}_c$, (**top**) for a model with small BM signature $\beta_0 = 5$, $D = 3$, and (**bottom**) for a model with large BM signature $\beta_0 = 660$, $D = 6$. The spread in the values of α is due to the variation in the other source parameters. The dashed line shows the linear fit in log space. The solid line shows the expected scaling $\alpha \propto \mathcal{M}_C^{\frac{5}{2}-2D}$. For small BM signatures, the expected scaling is recovered. For large BM signatures, higher than linear terms become relevant and the scaling breaks down.

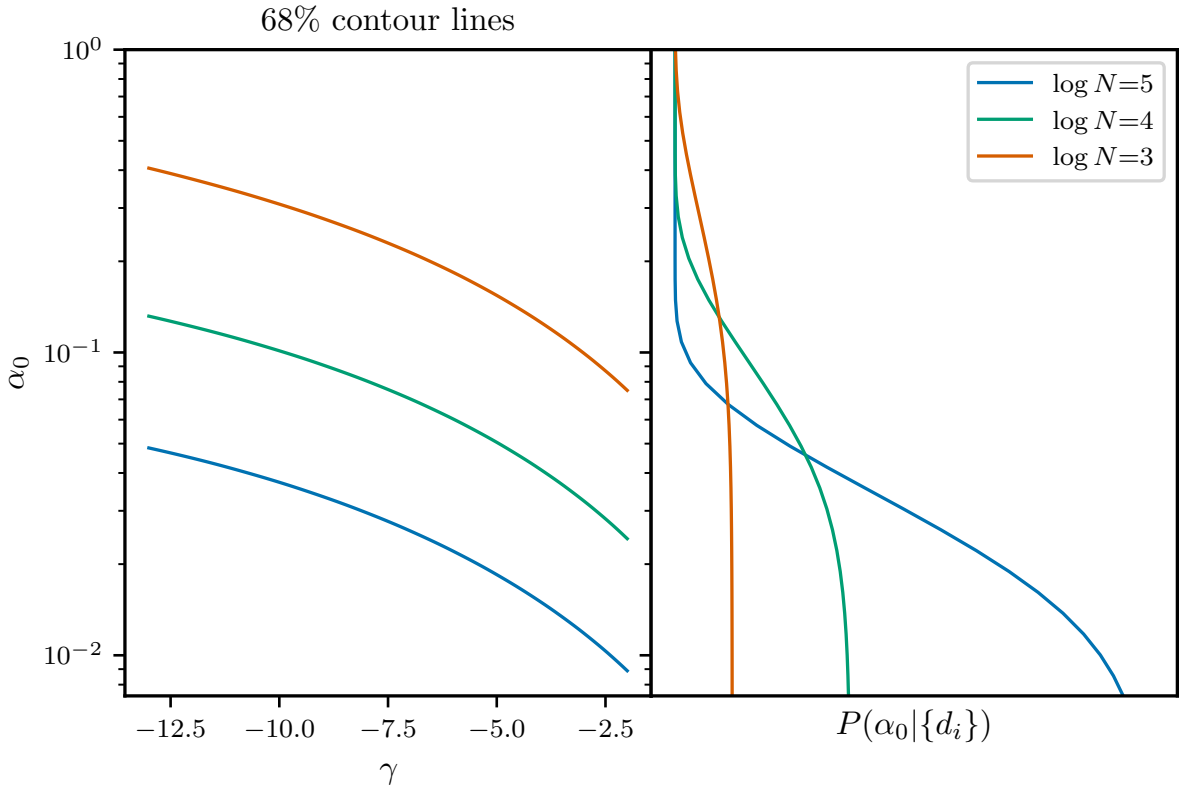


Figure 4.4: The upper limit of the 68 % credible interval on α_0 for different number of events, when the BM signature is set to zero. The right-hand plot shows the corresponding posteriors marginalised over γ. The constraint scale as $N^{-1/2}$, as expected from SNR arguments. The more negative values of γ, corresponding to higher dimensional operators, the weaker the bound that can be found.

Chapter 5

Challenges in solving Effective Fields of Gravity

The previous chapters were concerned with looking for BM signatures in a "bottom-up" approach, where the focus was on combing GW data for deviations from the SM without assuming a specific theory. This approach is motivated by the major technical and theoretical challenges in making accurate predictions for the BM signature in specific alternative theories of gravity in the strong field regime [107, 170, 171, 167, 49, 53, 81, 82, 190, 33]. There are downsides: BM signatures may appear in complex, subtle forms to which the search is not sensitive. Moreover, mapping between the agnostic and physically interpretable parameters may be difficult, if possible. In this chapter, we illustrate some aspects of solving the equations of motion for BBHs in a specific alternative theory of gravity. We focus on shift symmetric Einstein-scalar-Gauss-Bonnet theory, which is a well-motivated EFT alternative to GR, and the implementation of the "fixing-the-equations" approach to solve its equations in a regime where the problem is not obviously well-posed.

This chapter is mainly based on the work in [57]. I contributed to formulating the fixed equations and checking that they preserve the gauge constraints. The implementation of the scheme and the rest of the analysis described in the paper were performed by the other authors.

5.1 Einstein-scalar-Gauss-Bonnet theory as an EFT of gravity

As mentioned in Sec. 1.1.2, one way to introduce a deviation in the SM of GWs is to modify GR by adding higher dimensional operators to the action describing the dynamics of gravity. This is the framework of EFTs of gravity, where we assume that there exists a *complete theory* of gravity valid at all energy scales, which reduces to an EFT at low energies, with GR as the leading order term. A key point is that, when studying the EFT, we only consider a finite number of terms (up to a certain order of derivatives) in the action. This *truncated theory* correctly describes the dynamics of gravity up to a cut-off scale and loses its predictive power when higher-order derivatives become relevant.

The EFT is built by adding terms to the action chosen to satisfy certain assumptions. In this work, we make the assumptions that there is only one metric field, and that the theory is diffeomorphism invariant. In addition, it is common to require the action to lead to second-order field equations. We will expand on this last assumption shortly.

The Lovelock theorem [148] states that the most general equations of motion that satisfies the above assumptions are derived from the following Lagrangian density:

$$\mathcal{L} = \sqrt{-g}\left(R - 2\sum_{p\geq 2} k_p \delta^{a_1\ldots a_{2p}}_{b_1\ldots b_{2p}} R^{b_1 b_2}{}_{a_1 a_2}\ldots R^{b_{2p-1}b_{2p}}{}_{a_{2p-1}a_{2p}}\right), \tag{5.1}$$

where δ is the totally antisymmetric tensor. Importantly, the terms obtained from varying (5.1) with respect to the metric are conserved. This is important since they generalize the left-hand-side of (1.4), which must be conserved for the stress-energy tensor to be conserved as well ($\nabla_a T^{ab} = 0$). For future relevance, we note that the term with $p = 2$ is the Gauss-Bonnet term, and can be written as

$$\mathcal{G} = \left(R^2 - 4R_{ab}R^{ab} + R_{abcd}R^{abcd}\right). \tag{5.2}$$

Theories of this form are Lovelock theories and consist of the Einstein-Hilbert term to which are added antisymmetrized products of the Riemann tensor. Immediately, we see that in d dimensions, only the terms with $p \leq d/2$ do not vanish since antisymmetrizing over d or more indices gives zero. In 4 dimensions, the only non-vanishing term is the Einstein-Hilbert term. Therefore, Lovelock's theorem suggests that it is impossible to modify GR in 4 dimensions by adding higher curvature terms to the action while keeping the field equations second-order.

However, it is arguable that we have been too restrictive with this last assumption. Keeping second-order field equations is motivated by the Ostrogradsky theorem [173]: higher-order field equations generally lead to instabilities and unphysical solutions. There are arguments that this assumption may be too strong in the context of EFTs of gravity [40, 127, 203]. For example, it can be shown that the higher dimension operators leading to higher-order equations of motion can be refactored into lower-order operators. Furthermore, the theory we are constructing should be considered a truncation of a more fundamental theory of gravity, and the instability coming from higher-order derivatives may not be physical, but a removable artifact of the truncation. Finally, the higher-order derivative terms may simply remain small in the regime of validity of the EFT.

If we drop the requirements for the field equations to be second-order, we can consider theories other than Lovelock theories and modify GR in 4 dimensions. Notably, we can add terms to construct an EFT of gravity by adding terms made out of the Riemann tensor (and thus not introduce any other degrees of freedom). Such theories are actively studied in the literature [89, 53, 51, 50].

In this chapter, we take another approach. We keep the assumption that the theory should lead to second-order field equations, but instead, relax the assumption that the only gravitational field is the metric and add a non-minimally coupled scalar field—the most straightforward addition—to the theory. Horndeski's theorem is the equivalent of Lovelock's theorem with the addition of such a scalar field: it gives Horndeski theories as the most general diffeomorphism invariant theories of gravity with a single scalar field, a metric, and second order field equations. In the context of EFTs of gravity, the subset of Horndeski theories we will study is the most general containing up to dimension-4 operators that is parity invariant:

$$S = \frac{1}{8\pi G}\int d^4x\sqrt{-g}\left(\frac{1}{2}R - V(\phi) + X + \alpha(\phi)X^2 + \beta(\phi)\mathcal{G}\right). \tag{5.3}$$

It is commonly referred to as 4∂ST (4 derivative scalar-tensor) theory [227, 135]. Besides the potential term $V(\phi)$ and the kinetic term $X = -\frac{1}{2}g^{ab}\nabla_a\phi\nabla_b\phi$, the two new terms in the action are the X^2 term and the Gauss-Bonnet term. They are both of energy dimension four and must be suppressed by the square of some energy scale expressed in the functions α and β. This can be seen, equivalently, as the terms modifying GR being suppressed by a curvature scale, so we expect the strongest constraints on the theory to come from systems with large curvature. In the case of CBCs, this would be small mass BHs. Note that (5.3) is not in the canonical form of a Horndeski theory, but can be re-written in that form [133].

We focus, in particular, on the shift-symmetric 4∂ST theory with the action

$$S = \frac{1}{16\pi}\int d^4x\sqrt{-g}\left(R - g^{ab}\nabla_a\phi\nabla_b\phi + 2\lambda\phi\mathcal{G}\right), \tag{5.4}$$

where we have set $\beta(\phi) = \lambda\phi$, giving shift-symmetry up to total derivative (the integral of the Gauss-Bonnet term is a total derivative). This can also be seen as the linear term in the expansion of $f(\phi)$ in the small coupling approximation around $\phi = 0$ (the zeroth order term gives a total derivative). We also set $\alpha(\phi) = 0$, which corresponds to Einstein-dilaton-Gauss-Bonnet theory. The constraints on this theory can be given as the maximum value of $\sqrt{\lambda}$ (the square root is taken to give a length) allowed by observations. The most stringent to date is $\sqrt{\lambda} \lesssim 2.5\,\mathrm{km}$ from [182, 149].

Besides being a representative of 4∂ST theories, shift-symmetric Einstein-scalar-Gauss-Bonnet theory (which we will refer to as Einstein Scalar-Gauss-Bonnet (ESGB) for brevity) is particularly interesting for observational reasons [81, 192, 237, 236, 206, 204]. The scalar field equation of motion shown below in (5.5) means that even if the scalar field and its derivatives are initially zero, if the Gauss-Bonnet term is non-zero (which is the case for BHs), the scalar field will be sourced and grow. BH solutions in this theory are thus expected to have "hair"—to have a non-zero scalar charge. The scalar field dynamics also affect GW radiation. Dipole radiation has an effect at -1PN order and thus dominates the GW signal in the early inspiral regime. This effect has led to constraints on $\sqrt{\lambda}$ from GW observations [149, 182]. Overall, coalescing BHs in ESGB theory are expected to lose energy to scalar radiation, which will cause the coalescence to be faster than in GR. We thus expect a dephasing in the GW signal, which can also be observed in the late inspiral and merger [58].

The equations of motion for the theory (5.4) are

$$E^{(\phi)} = \Box\phi + \lambda\mathcal{G} = 0, \tag{5.5}$$

$$E^{(g)}_{ab} = R_{ab} - \frac{1}{2}g_{ab}R - \nabla_a\phi\nabla_b\phi + \frac{1}{2}(\nabla\phi)^2 g_{ab} + 2\lambda\delta^{efcd}_{ijg(a}g_{b)d}R^{ij}{}_{ef}\nabla^g\nabla_c\phi = 0. \tag{5.6}$$

As mentioned above, these equations were found to give well-posed initial value problems for sufficiently small values of λ [135, 136] in the Modified Generalized Harmonic (MGH) gauge. We point the reader to the above references for a review of this gauge. For this thesis, the gauge means that the equations we consider for numerical evolution are

$$E^{(g)}_{ab} = Q_{ab}, \tag{5.7}$$

$$E^{(\phi)} = 0, \tag{5.8}$$

where the MGH constraint is satisfied when $Q_{ab} = 0$ so that the equations reduce to the ones in eqs. (5.5) and (5.6). Due to the Bianchi identity, this constraint is conserved.

These equations can be written in the form:

$$\begin{pmatrix} \mathcal{A}_{ab}{}^{ef} & \mathcal{B}_{ab} \\ \mathcal{C}^{ef} & \mathcal{D} \end{pmatrix} \partial_0^2 \begin{pmatrix} g_{ef} \\ \phi \end{pmatrix} = \begin{pmatrix} \mathcal{S}^{(g)}_{ab} \\ \mathcal{S}^{(\phi)} \end{pmatrix}, \tag{5.9}$$

where the values of $\mathcal{A}_{ab}{}^{ef}$, $\mathcal{B}_{ab}$, $\mathcal{C}^{ef}$, and $\mathcal{D}$ are given in Appendix A of [82]. These equations are evolved using the method of lines.

5.2 Well posedness and the *fixing-the-equations* procedure

In order to evolve a system (BBHs for example) given equations of motion, the initial conditions, boundary conditions, and the equations must define an well-posed initial value problem. This allows us to make predictions about the system given a set of initial data. A well-posed problem is one for which a solution (i) exists, (ii) is unique, and (iii) depends continuously on the initial data. The last condition can be stated as follows: given an initial solution $\phi(t = 0, x)$, the solution at time t must be bounded as

$$||\phi(t, x)|| \leq A \exp(Bt) \, ||\phi(0, x)||, \tag{5.10}$$

where A and B are constants independent of the initial data, and $||\cdot||$ is a Sobolev norm, for example the L2 norm: $||\phi|| = \left(\int \phi^2 dx\right)^{1/2}$ [105].

Horndeski theories, and EFTs of gravity, contain higher-order derivatives terms which are non-trivial and important in the non-linear regime of BBH mergers. Even for an initially well-posed problem, these terms can lead to pathologies that break well-posedness when higher energy modes are excited. Even when no mathematical pathology arises, a cascade of energy from low to high frequencies can drive the problem outside the domain of validity of the EFT as higher-order derivative terms become dominant. A common pathology is the appearance of naked elliptical regions, which are regions where the equations of motion change character from hyperbolic to elliptic and are not shielded by an event horizon. This has been shown to happen in certain setups for ESGB [81].

To illustrate character transitions, consider the prototypical *Tricomi* and *Keldysh* equations

$$\partial_y^2 u(x,y) + y\partial_x^2 u(x,y) = 0, \tag{5.11}$$

$$\partial_y^2 u(x,y) + \frac{1}{y}\partial_x^2 u(x,y) = 0. \tag{5.12}$$

Both equations are hyperbolic for $y < 0$ and transition character to elliptic for $y > 0$ (and are parabolic at $y = 0$). However, the behaviour of the characteristic speeds is different around the character transition: for the Tricomi equation, the characteristic speeds are $\pm\sqrt{u}$—the speeds go to zero at the transition—while for the Keldysh equation, the characteristic speeds are $\pm\sqrt{1/u}$—the speeds diverge at the transition.

Importantly, ESGB theories are known to have a well-posed initial value problems when the coupling is small compared to other length scales in the problem (e.g. the size of the black holes) [135, 136] in a specific gauge. In the context of constraining EFTs of gravity with GW observations, the important question is whether the evolution of CBCs is well-posed in the theory. Numerical simulations have successfully been performed [82, 58] for mergers in ESGB. However, some parts of the parameter space of the theory could not be evolved, potentially due to a breakdown in hyperbolicity.

As mentioned before, it is possible that this breakdown is due to the excitation of high-frequency modes with truncation errors. It is also possible that the problem is indeed ill-posed in the truncated theory, but that higher-order terms appearing at a larger energy scale from the full theory would regularize the problem.

The *fixing-the-equations approach* [49] (also [7, 53]), is inspired by EFT arguments we discussed. It is related to strategies developed to fix issues in dissipative relativistic hydrodynamics [116, 115]. The key strategy is to adopt a prescription to dynamically control the high frequency behaviour of the truncated theory, motivated by respecting the separation of scales already assumed in obtaining the original equations in the first place. This is achieved by modifying, in a somewhat ad hoc way, the higher-order contributions to the equations of motion at *short wavelengths* through the introduction of auxiliary massive fields. The auxiliary fields are evolved according to driver equations that force them to approach the long wavelength behaviour dictated by the original theory, while effectively dissipating shorter wavelength components.

As a consequence, modes with wavelengths above a certain scale fully backreact dynamically respecting the original system of equations. If the system's dynamics do not display a significant UV cascade, the solution is largely insensitive to the details of the driver prescription (e.g. Ref. [99]). Otherwise, it does, therefore providing a powerful way

to discern whether the scenario studied satisfies the assumptions taken to design the beyond GR theory under study. This strategy has been successfully implemented in different models and spacetimes of physical interest [34, 33, 97, 142, 51].

To illustrate the procedure, we consider a toy model scalar field equation of motion in flat spacetime:

$$\gamma^{ab}\left(\phi_{,ab}, \phi_{,a}, \phi, x^a\right) \phi_{,ab} = \sigma\left(\phi_{,a}, \phi, x^a\right). \tag{5.13}$$

The effective metric γ^{ab}, which determines the characteristic behaviour of the system, can be a function of the field ϕ and its derivatives, hence the non-linearity and the potential for pathologies like character transitions. Repeated derivatives (e.g. $\left(\phi_{,ab}\right)^2$) cause ambiguities in defining γ^{ab}. Horndeski theories, however, do not generally have such terms [176, 177].

For simplicity and as a simple illustration of the features of the theory relevant to the fixing procedure we will shortly present, consider a 1+1 dimensional problem in a coordinate system (t, r). The equation can be re-arranged so that the second-order derivatives in time are isolated:

$$\begin{aligned} \gamma^{tt}\left(\phi_{,a}, \phi, x^a\right) \phi_{,tt} &= -2\gamma^{tr}\left(\phi_{,a}, \phi, x^a\right) \phi_{,tr} - \gamma^{rr}\left(\phi_{,a}, \phi, x^a\right) \phi_{,rr} + \sigma\left(\phi_{,a}, \phi, x^a\right) && (5.14)\\ &= S\left(\phi_{,tr}, \phi_{,rr}, \phi_{,a}, \phi, x^a\right), && (5.15) \end{aligned}$$

where we have defined S as all the terms that do not contain second-order time derivatives. When considering an EFT, whose leading-order term is known to give a well-posed problem, we can write γ^{tt} and S as the sum of the leading order terms and higher-order EFT contributions:

$$\begin{aligned} \gamma^{tt} &= \gamma^{tt}_{\mathrm{LO}} + \gamma^{tt}_{\mathrm{EFT}}, && (5.16)\\ S &= S_{\mathrm{LO}} + S_{\mathrm{EFT}}. && (5.17) \end{aligned}$$

Then, we can write the equation

$$\begin{aligned} &\gamma^{tt}_{\mathrm{LO}}\left(\phi_{,a}, \phi, x^a\right) \phi_{,tt} && (5.18)\\ &= S_{\mathrm{LO}}\left(\phi_{,tr}, \phi_{,rr}, \phi_{,a}, \phi, x^a\right) - \underbrace{\gamma^{tt}_{\mathrm{EFT}}\left(\phi_{,a}, \phi, x^a\right) \phi_{,tt} - S_{\mathrm{EFT}}\left(\phi_{,tr}, \phi_{,rr}, \phi_{,a}, \phi, x^a\right)}_{\tilde{S}}. && (5.19) \end{aligned}$$

We obtain an expression similar to that of the well-posed problem, plus a source term $\tilde{S}$ that contains all the effects of the higher-order terms. There is a crucial difference, as $\tilde{S}$ depends on the second-order time derivatives of the field, which prevents us from evolving (e.g numerically) the equation in the same way as the well-posed problem. This can be

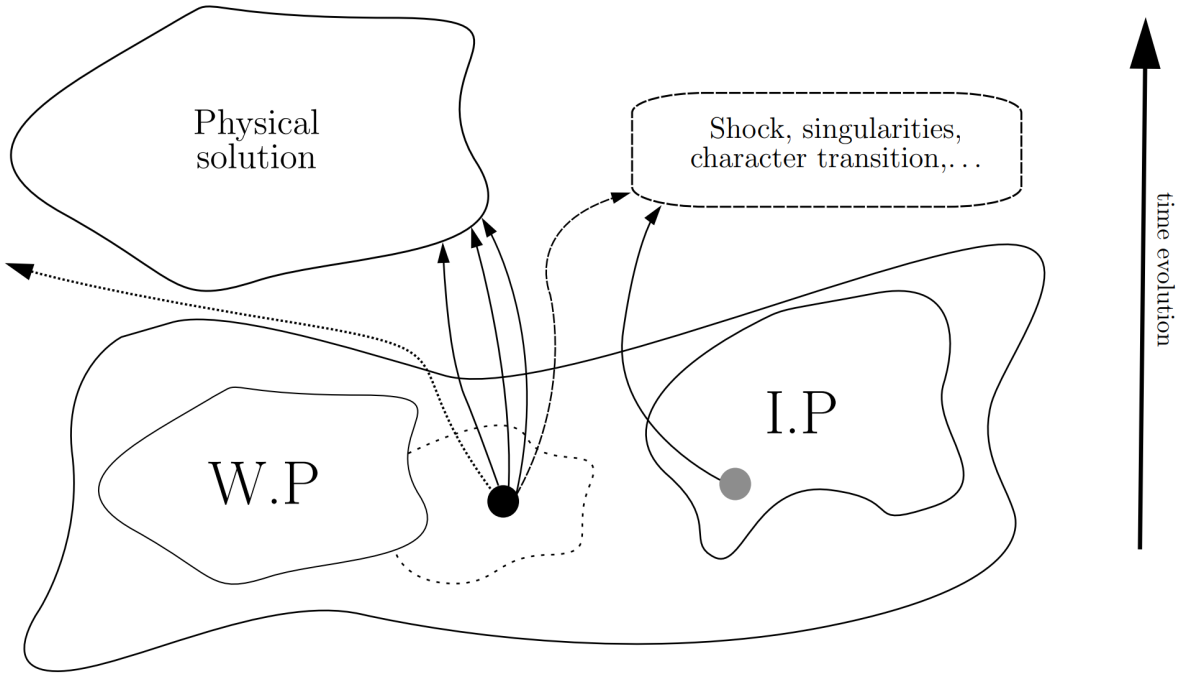


Figure 5.1: **Parameter space of possible theories, initial conditions and boundary conditions**. Through observations or analysis, some regions are known to lead to ill-posed problems (I.P) with shocks, character transitions, and other pathologies, and some are known to be well-posed (W.P), leading to physical solutions. A particular problem (black circle) of a given theory in a region of unknown well-posedness may appear ill-posed (dashed trajectory). By controlling the higher frequency behaviour of the theory, one can regularize the problem into the full arrows. By studying at the dependence of the solution on the control parameter (moving between the full trajectories) one can infer whether one is cutting off a flow to the UV.

bypassed by using *order reduction*, where we solve for $\phi_{,tt}$ to leading order (without the EFT contributions), and substitute the result on the right-hand side of the equation.

As an interesting note, the characteristic speeds $V_\pm$ for a system of the form (5.15) are given by

$$V_\pm = -\frac{\gamma^{tr}}{\gamma^{tt}} \pm \sqrt{-\frac{\det(\gamma^{ab})}{(\gamma^{tt})^2}}. \tag{5.20}$$

A character transition occurs when the determinant of the effective metric changes sign. Whether the transition is of Tricomi or Keldysh type depends on whether $\det(\gamma^{ab}) \to 0$ or $\gamma^{tt} \to 0$ faster. In the order reduced system, the γ^{tt} term is the same as in the well-posed problem, so $(\gamma^{tt})^2$ is positive definite and the system can only undergo a Tricomi-type transition. Order reduction can therefore control some of the pathologies that may arise in the truncated theory.

With the fixing-the-equations approach, we can further modify the equations of motion so that the entire principle part is that of the well-posed problem. Let G be the leading order terms $(\gamma^{tt}_{\rm LO} - S_{\rm LO})$ and M and N be a splitting of the EFT terms. Then, the equation of motion can be written as

$$G + M + N = 0. \tag{5.21}$$

In the fixing procedure, the equation is modified to

$$G + \Pi + N = 0, \tag{5.22}$$

$$\sigma A[M] = \Pi_{,t} + \kappa\left(\Pi - M\right), \tag{5.23}$$

where A is a differential operator (for example, we will use the curved space d'Alembertian in the next section). The prescription replaces the M terms with the auxiliary field Π. The right-hand side drives Π to the solution of the original equation within a timescale set by κ and σ. The parameters κ and σ, the form of A, and the splitting between M and N are chosen to control the high-frequency behaviour of the theory while reproducing the low-frequency behaviour of the original theory.

5.3 Fixing scheme for EsGB gravity

To implement the fixing scheme, we replace the equations of motion eqs. (5.5) and (5.6) with the following fixed system of equations:

$$\Box\phi + \Pi^{(\phi)} = 0, \tag{5.24}$$

$$R_{ab} - \frac{1}{2}g_{ab}R - \nabla_a\phi\nabla_b\phi + \frac{1}{2}\left(\nabla\phi\right)^2 g_{ab} + \Pi^{(g)}_{ab} \tag{5.25}$$

$$= Q_{ab}, \tag{5.26}$$

$$\sigma g^{ab}\partial_a\partial_b\mathbf{P} = \partial_0\mathbf{P} + \kappa\left(\mathbf{P} - \mathbf{S}\right), \tag{5.27}$$

where, as mentioned in the previous section, Q_{ab} is some function of the MGH constraint that vanishes when the constraint is satisfied, $\mathbf{P} = \left(\Pi^{(\phi)}, \Pi^{(g)}_{ab}\right)$ encompasses the metric and scalar auxiliary fields, and κ and σ are constants that determine the timescale over which the auxiliary fields are driven to their corresponding desired values $\mathbf{S}$. These parameters also determine the length scale below which short wavelength features are effectively damped away.

Associated with these parameters we define two timescales

$$t_1 \equiv 2\sigma, \quad t_2 \equiv \sqrt{\frac{\sigma}{\kappa}}\,, \tag{5.28}$$

which combine to give the slowest[1] timescale for the variable $\mathbf{P}$ to decay to its target solution $\mathbf{S}$, given by $T^{-1} = -t_1^{-1} + \sqrt{-t_2^{-2} + t_1^{-2}}$. We stress here that there are many ways one could drive the fixing variables $\mathbf{P}$ to their true solution $\mathbf{S}$. From an EFT point of view, sub-leading terms to the equations of ESGB would come with one higher power of curvature, thus two additional derivatives of the gravitational field. Thus, we find a wave operator prescription to be natural in light of this observation and the nature of the Einstein equations. Nevertheless, this is just a matter of choice if a strong UV cascade does not take place.

We note that a non-trivial departure from a stationary solution satisfying $\mathbf{P} = \mathbf{S}$ can be obtained for a non-vanishing value of σ (due to contributions from $\sigma g^{\mu\nu}\partial_\mu\partial_\nu\mathbf{P}$). However, by making this parameter sufficiently small, one can minimize the difference[2] between $\mathbf{P}$ and $\mathbf{S}$.

[1] There is also a faster timescale that can be relevant for numerical applications, as it has to be suitably resolved when employing an explicit time integrator.

[2] Alternative choices can be made so that this is not an issue, e.g., by adding to the source a suitable contribution of $\partial_\mu\partial_\nu\mathbf{S}$, considering a different type of driver equation, etc. We do not concern ourselves with such options in this work.

Naturally, the solution to this system of equations will depend on the value of the ad hoc timescales, though if these are made sufficiently small compared to the other physical scales, and there is no significant cascade towards the UV, we expect this dependency to be subleading. We will thus check how our solutions depend on the fixing parameters and their impact on physical observables and contrast it with the full solution obtained though the MGH formulation of shift-symmetric ESGB gravity. We note that the equations of motion for ESGB gravity can only be stably evolved in time for weakly-coupled solutions [191, 136, 135, 82, 190]. That is, when the Gauss-Bonnet corrections to the spacetime geometry remain sufficiently small compared to the smallest curvature length scale in the solution. We will also use the fixing-the-equations approach to briefly explore regimes of the parameter space where the MGH formulation breaks down.

Rewrite the fixed system of equations eqs. (5.24), (5.25) and (5.27) in the same form as (5.9). To do so, we move all the ESGB contribution to the right-hand side of (5.9) where the source terms are,

$$\begin{pmatrix} \mathcal{A}_{ab}{}^{(\mathrm{GR})ef} & 0 \\ 0 & \mathcal{D} \end{pmatrix} \partial_0^2 \begin{pmatrix} g_{ef} \\ \phi \end{pmatrix} = \begin{pmatrix} \mathcal{S}_{ab}^{(\mathrm{GR})(g)} + \mathcal{S}_{ab}^{(\mathrm{GB})(g)} - \mathcal{B}_{ab}\partial_0^2\phi - \mathcal{A}_{ab}{}^{(\mathrm{GB})ef}\partial_0^2 g_{ef} \\ \mathcal{S}^{(\mathrm{GR})(\phi)} + \mathcal{S}^{(\mathrm{GB})(\phi)} - \mathcal{C}^{ef}\partial_0^2 g_{ef} \end{pmatrix} . \tag{5.29}$$

Note that, by doing so, we have recovered the same principal part as in GR. Note that we also split the purely GR and additional ESGB contributions in the source terms. Introducing the source terms $\mathbf{S} = \left(\tilde{S}_{ab}^{(g)}, \tilde{S}^{(\phi)}\right)$, which include all contributions from ESGB, one has

$$\begin{pmatrix} \mathcal{A}_{ab}{}^{(\mathrm{GR})ef} & 0 \\ 0 & \mathcal{D} \end{pmatrix} \partial_0^2 \begin{pmatrix} g_{ef} \\ \phi \end{pmatrix} = \begin{pmatrix} \mathcal{S}_{ab}^{(\mathrm{GR})(g)} \\ \mathcal{S}^{(\mathrm{GR})(\phi)} \end{pmatrix} - \begin{pmatrix} \tilde{S}_{ab}^{(g)} \\ \tilde{S}^{(\phi)} \end{pmatrix} . \tag{5.30}$$

Introducing eleven massive fields $\mathbf{P} = \left(\Pi^{(\phi)}, \Pi_{ab}^{(g)}\right)$, we write the system as,

$$\begin{pmatrix} \mathcal{A}_{ab}{}^{(\mathrm{GR})ef} & 0 \\ 0 & \mathcal{D} \end{pmatrix} \partial_0^2 \begin{pmatrix} g_{ef} \\ \phi \end{pmatrix} = \begin{pmatrix} \mathcal{S}_{ab}^{(\mathrm{GR})(g)} \\ \mathcal{S}^{(\mathrm{GR})(\phi)} \end{pmatrix} - \begin{pmatrix} \Pi_{ab}^{(g)} \\ \Pi^{(\phi)} \end{pmatrix} . \tag{5.31}$$

When $\Pi = \tilde{S}$, the equations are 'unfixed.' To fix the equations, we choose the driver equation (5.27). Note that the source terms depend on second derivatives in time of the metric and scalar field $\mathbf{S} = \mathbf{S}\left[\ldots \partial_0^2 g, \partial_0^2 \phi \ldots\right]$. We compute those by applying order reduction, i.e. we substitute the zeroth order solutions to the second time derivatives, obtained by solving for (5.30) with $\mathbf{S} = 0$. This implies that the solutions to the fixed system eqs. (5.24), (5.25) and (5.27) are valid to first order in the coupling of the theory.

Finally, in order to justify and guide our choices for the fixing parameters $\{\sigma, \kappa\}$, we analytically solve for a simpler fixing equation (where we set any spatial dependence to zero), albeit with most of the features of the true fixed equation,

$$\sigma \frac{d^2 P}{dt^2} + \frac{dP}{dt} + \kappa(P-1) = 0. \tag{5.32}$$

The general solution to this equation, subject to $P(0) = dP/dt(0) = 0$, is

$$\begin{aligned} P(t) = &-e^{a_+ t} \frac{(-\sqrt{-4\kappa\sigma+1} + 4\kappa\sigma - 1)}{2(4\kappa\sigma - 1)} \\ &-e^{a_- t} \frac{(\sqrt{-4\kappa\sigma+1} + 4\kappa\sigma - 1)}{2(4\kappa\sigma - 1)} + 1, \end{aligned} \tag{5.33}$$

where

$$a_+ = \frac{-1 + \sqrt{1 - 4\kappa\sigma}}{2\sigma} \quad , \quad a_- = -\frac{1 + \sqrt{1 - 4\kappa\sigma}}{2\sigma}. \tag{5.34}$$

The solutions to this system will decay, but depending on the values chosen for the fixing parameters, the solutions might undergo an oscillatory decay. Large oscillations will lead to stages where the system overshoots the original one, a feature that we consider it best to avoid. To keep both solutions decaying at roughly the same rate, and the frequency of oscillations small, one could choose $4\kappa\sigma \simeq 1$. In that case, the decay rate is $T \approx 2\sigma$, though care should be exercised to avoid singular behavior indicated by the solution, Eq. (5.33). The timescale should also be taken to be smaller than the smallest relevant scales in the problem being studied, in order to approach the original system; however, if the timescale T is made too short, it may lead to stiff behavior in the numerical evolution, requiring higher resolution. Finally we note that, depending on the driver equation adopted, a small σ is desirable to avoid spurious spatial dependence.

5.4 Applying the fixing scheme to BHS

The goal of [57] was to compare ESGB solutions obtained from the fixing scheme to the solutions obtained from the original equations in the strong regime—BHs and their mergers—in a region of parameter space where the original equations have a well-posedness problem. The paper also compared the solutions obtained by another method of approximation, the *order-by-order* method, which we will not discuss here, but which has been studied for EFT-motivated theories in the strong regime [170, 171, 167].

Three different spacetimes were considered: a single BH undergoing scalarization, a head-on collision of two BHs, and a binary system of two BHs in a quasi-circular orbit.

Single BH scalarization: the solution obtained with the fixed equations agrees to an error of order one percent with the reference solution obtained from the original equations. This holds true as the dimensionless coupling $\frac{\lambda}{M^2}$ increases (up to the tested $\lambda = 0.15M^2$). This is shown in Figure 5.2, where the charge of the scalar field Q computed at $r = 100M$ is plotted against look-back time. [3] In all cases, the initially hairless BH acquires a scalar charge that saturates to a stationary value/state. For larger couplings, this happens fast enough to overshoot the final charge value [192]. As mentioned in Sec. 5.2, the time scale at which the fixed solution decays to the original solution should be shorter than any other time scale in the system. In the limit $T \to 0$, the fixed equations should recover the original equations. On the right panel of Figure 5.2, we see that longer decay timescales lead to a larger error compared to the reference solution, but that the original equations are recovered as $T \to 0$. The solution at $T = 0$ is interpolated from the non-zero T solutions. The fixed solutions on the left panel of Figure 5.2 are the interpolated solutions at $T = 0$. To probe the use of the fixing scheme as a tool to explore EFT theories, jkit is interesting to see whether the fixed equations can evolve a solution in a regime where the hyperbolicity of the original ESGB equations breaks down. For a non-spinning BH, the hyperbolicity of the original ESGB will fail for $\lambda > 0.23M^2$ [205, 193]. However, with the fixed equations, solutions can be obtained for a coupling $\lambda = 0.25M^2$, at least until a certain time.

Head-on collision of two BHs: Two initially un-scalarized BHs of equal masses are initialised with enough separation to form scalar hair before merger—the ESGB coupling is gradually turned on between $t = 0$ and $t = 100M$, while the merger occurs around $t = 315M$. As in the single BH case, the fixed solutions become closer to the reference as the decay time T is decreased, both in terms of peak amplitude and dephasing. This is seen in Figure 5.3, where the Ψ_4 Penrose-Newman quantity ($l = 2, m = 0$ mode) is plotted as a function of look-back time.

Quasi-circular inspiral of two BHs: The final case considered is a GW150914-like binary system, where the BHs have a mass ratio of 1.22 and inital separation of $9.8M$ (about 6 orbits before merger in GR). The coupling is again turned on gradually, between $t = 0$ and $t = 200M$. Unlike the head-on collision, the fixed solutions merge earlier than the reference solutions. In fact, the shorter the decay timescale the earlier the merger and the larger error compared to the reference solution. This is shown in Figure 5.4, where the waveform is plotted against look-back time for the GR waveform, the reference solution, and two fixed solutions with different decay timescales. On the right panel, the dephasing

[3] The charge Q is computed from the asymptotic behaviour of the scalar field: $\phi = Q/r + \mathcal{O}(1/r^2)$.

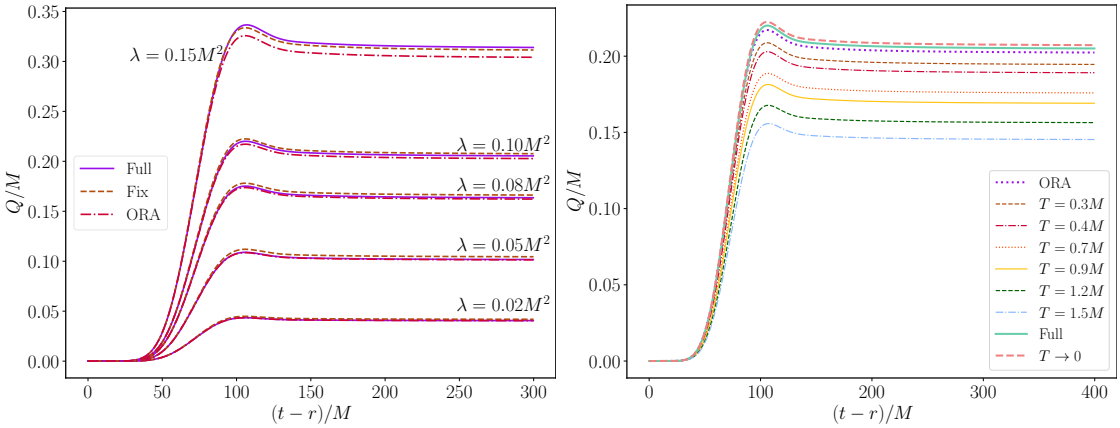


Figure 5.2: Charge of the scalar field Q as a function of look-back time for a single BH undergoing scalarization. The BH, initially hairless, acquires a scalar charge that saturates to a stationary state. **Left:** The fixed solutions (dashed lines) for $T \to 0$ agree with the reference solution (full lines) obtained for increasing values of the coupling. The lines labelled "ORA" are order-by-order solutions, which we do not discuss here. **Right:** The fixed solutions approach the reference solution as $T \to 0$.

$\Delta\Phi$ compared to GR is plotted, showing that it is larger for shorter decay timescales. One possible explanation for this is a lack of numerical resolution to resolve the timescales in the fixed system.

5.5 Fixing equations and constraints

Here we argue that constraints are preserved by the fixed equations. First, recall that constraint damping in the generalized harmonic formulation is achieved by ensuring the effective evolution of the coordinate conditions is damped away (see Ref. [103]). Such a behaviour is enforced by adding a suitable contribution to Einstein equations that: (i) is proportional to the constraints, and (ii) is such that, upon taking the divergence and using the Bianchi identity, the constraints are seen to obey a homogeneous damped wave equation. As a result, violations of the constraints are driven towards zero.

In the case of beyond GR theories, extra contributions appear in the equations of motion in addition to the Einstein tensor. An analogous constraint damping strategy can be adopted in such cases (for an explicit discussion in the case of ESGB, see Ref. [82]), where one uses explicitly that the extra contributions should have zero divergence.

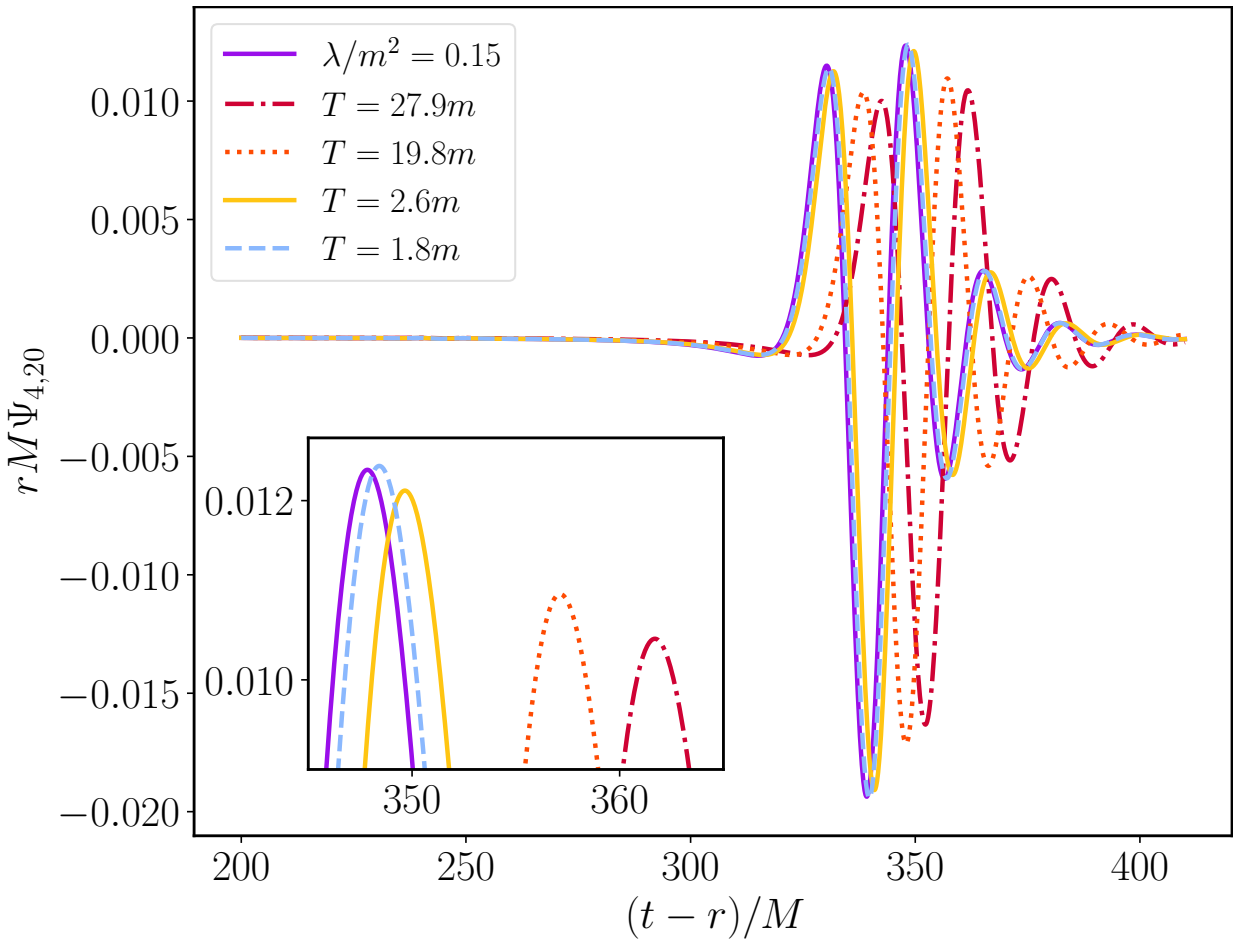


Figure 5.3: Ψ_4 as a function of look-back time for a head-on collision of two BHs. The fixed solutions (dashed lines) approach the reference solution (full line) as $T \to 0$.

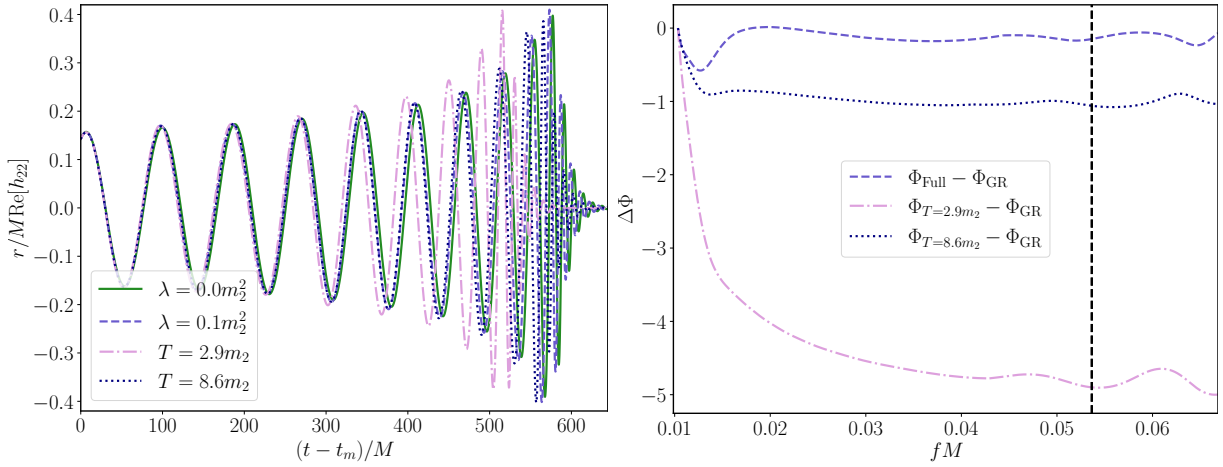


Figure 5.4: **Left:** The waveform as a function of look-back time for a binary BH inspiral. The fixed solutions merge earlier than the reference solution and than in GR. **Right:** The dephasing $\Delta\Phi$ compared to GR is larger for shorter decay timescales T.

When fixing the equations, such an identity is not explicitly enforced. The resulting induced evolution equations for the constraint violation contain an additional source from the divergence of such tensor which must be shown to suitably approach zero in the adopted fixing-the-equations approach. We next argue this is the case.

The modified gravity theory in a suitable formulation is governed by

$$G^{ab} + S^{ab} + M^{ab} = Q^{ab}, \tag{5.35}$$

where the beyond GR contributions are split into S^{ab}—containing contributions with second order derivatives—and M^{ab}—which contains the remaining terms, and Q^{ab} is the constraint function that vanishes when the constraints are satisfied (for example, F^{ab} in Eq. (5.25)). Furthermore, the divergence of Q^{ab} gives rise to a damped evolution equation for the constraints, to converge to the left hand side, which is zero as $\nabla_a S^{ab} = -\nabla_a M^{ab}$. That is

$$\nabla_a \left(G^{ab} + S^{ab} + M^{ab}\right) = 0 = \nabla_a Q^{ab}, \tag{5.36}$$

so the constraints are conserved. The fixed equations replace S^{ab} by $\Pi^{(g)}{}_{ab}$[4] and provide an equation of motion for this tensor to approach S^{ab}:

$$G^{ab} + \Pi^{ab} + M^{ab} = Q^{ab}. \tag{5.37}$$

[4]In the main text, we label such an object as $\Pi^{(g)}{}_{ab}$. Here, we will drop the label $^{(g)}$ for convenience.

Notice that $\nabla_a M^{ab} = \Pi^{\phi} \nabla_b \phi$ by definition and, due to the fixed equation introduced for its dynamics, it approaches $-2\lambda \mathcal{G} \nabla_b \phi$. We next argue that the fixing equation enforces that $\nabla_a \Pi^{ab}$ approaches $\nabla_a S^{ab}$ in a controlled manner.

Starting with the equation of motion for Π_{ab}:

$$\nabla_c \nabla^c \Pi^{ab} = \frac{1}{\sigma} n^c \nabla_c \Pi^{ab} + \frac{\kappa}{\sigma} \left(\Pi^{ab} - S^{ab} \right), \tag{5.38}$$

where, for simplicity, we adopted a slightly different form of the equation than the one used explicitly in this work to aid in the presentation. Next, we take the covariant derivative

$$\begin{aligned} \nabla_a \nabla_c \nabla^c \Pi^{ab} - \frac{1}{\sigma} \nabla_a \left(n^c \nabla_c \Pi^{ab} \right) \\ - \frac{\kappa}{\sigma} \left(\nabla_a \Pi^{ab} - \nabla_a S^{ab} \right) = 0. \end{aligned} \tag{5.39}$$

Using the fact that $R_{ab} \simeq \mathcal{O}(\lambda)$, the first term, to order $\mathcal{O}(\lambda^2)$, gives

$$\begin{aligned} \nabla_a \nabla_c \nabla^c \Pi^{ab} &= \nabla_c \nabla_a \nabla^c \Pi^{ab} - R_{ace}{}^b \nabla^c \Pi^{ae} \\ &= \Box \left(\nabla_a \Pi^{ab} \right) - R_{ace}{}^b \nabla^c \Pi^{ae} - \nabla^c \left(R_{ace}{}^b \Pi^{ae} \right). \end{aligned} \tag{5.40}$$

Proceeding analogously, to the same order, the second term gives

$$\begin{aligned} \nabla_a \left(n^c \nabla_c \Pi^{ab} \right) &= \left(\nabla_a n^c \right) \nabla_c \Pi^{ab} + n^c \nabla_a \nabla_c \Pi^{ab} \\ &= \left(\nabla_a n^c \right) \nabla_c \Pi^{ab} + n^c \nabla_c \nabla_a \Pi^{ab} - n^c R_{ace}{}^b \Pi^{ae}. \end{aligned} \tag{5.41}$$

Combining it all together we have

$$\begin{aligned} 0 =& \Box \left(\nabla_a \Pi^{ab} \right) - \frac{1}{\sigma} n^c \nabla_c \left(\nabla_a \Pi^{ab} \right) \\ & - \frac{\kappa}{\sigma} \left(\nabla_a \Pi^{ab} - \nabla_a S^{ab} - \frac{1}{\kappa} n^c R_{ace}{}^b \Pi^{ae} \right) \\ & - R_{ace}{}^b \nabla^c \Pi^{ae} - \nabla^c \left(R_{ace}{}^b \Pi^{ae} \right) \\ & - \frac{1}{\sigma} \left(\nabla_a n^c \right) \nabla_c \Pi^{ab}. \end{aligned} \tag{5.42}$$

The first two lines drive $\nabla_a \Pi^{ab}$ to $\nabla_a S^{ab} + (1/\kappa)\, n^c R^b_{ace} \Pi^{ae}$. The first term is precisely what cancels the contribution from $\nabla_a M^{ab}$, and the second one is not only subleading with respect to curvature, but also can be made smaller by a judicious choice of κ. To examine

the role of the other contributions, we can use the cyclic symmetries of the Riemann tensor and $\Pi^{ab} = \Pi^{(ab)}$. The third line simplifies, because

$$\Pi^{ae}\nabla^c R_{ace}{}^b = -\Pi^{ae}\nabla^c \left(R_{cea}{}^b + R_{eac}{}^b\right) \tag{5.43}$$
$$= -\Pi^{ae}\nabla^c R_{cea}{}^b \tag{5.44}$$
$$= -\Pi^{ae} g^{bd}\nabla_c R^c{}_{ead} \tag{5.45}$$
$$= \Pi^{ae} g^{bd}\left(\nabla_a R^c{}_{edc} + \nabla_d R^c{}_{eca}\right) \sim \mathcal{O}\left(\lambda^2\right). \tag{5.46}$$

So we then have

$$R_{ace}{}^b \nabla^c \Pi^{ae} = \nabla^c \left(R_{ace}{}^b \Pi^{ae}\right) + \mathcal{O}\left(\lambda^2\right). \tag{5.47}$$

The third line and the last term from the second line give

$$2\nabla^c F_c{}^b - \frac{1}{\sigma} n^c F_c{}^b, \tag{5.48}$$
$$F_c{}^b := R_{ace}{}^b \Pi^{ae}. \tag{5.49}$$

This contribution is not only proportional to curvature terms, but also has an extra order of derivatives, which should be subleading in the valid EFT regime. Thus, $\nabla_a \Pi^{ab}$ converges to $\simeq \nabla_a S^{ab} + (1/\kappa)\, n^c R^b_{ace} \Pi^{ae}$. The last term can be reduced by the choice of κ. As a consequence, the divergence of Eq. (5.37) gives rise to controlled dynamics for the constraints, approximating the behavior from the original system, as expected.

In our studies, we have confirmed this behavior and, unless the timescale T employed is much larger than the scale of the black holes considered, the constraints remain under control and the solutions show a convergent behavior throughout the evolutions. We show the behavior of the constraint violation with increasing numerical resolution in Fig. 5.5, and when increasing κ in Fig. 5.6. The constraint violation is found to decrease with one or the other, depending on which contribution dominates at a given time.

5.6 Discussion

In this chapter, we gave an overview of particular challenges and solutions in numerically evolving alternative theories of gravity. Numerical solutions to such theories are the foundations of theory-specific tests of the SM of GWs, which are complementary to the null-tests discussed in the rest of this thesis.

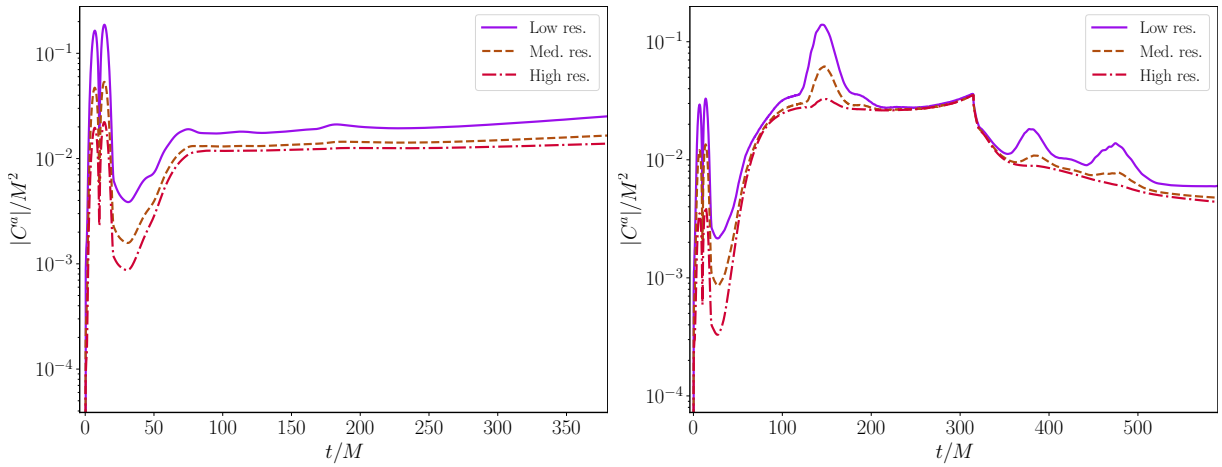


Figure 5.5: Integrated norm of the constraint violation C_a as a function of coordinate time (in units of the total mass) for the scalarization of a single black hole spacetime with a coupling value of $\lambda = 0.04M^2$ (left) and for an equal-mass head-on collision with $\lambda = 0.04m^2$ (right) at three resolutions when solving the fixed system of equations. The damping parameters for the single black hole are $\{\sigma, \kappa\} = \{0.2M, 0.5/M\}$ so that $T = 1.8M$, and similarly for the head-on collision, where M is now mass of each individual black hole. The medium and high resolutions have 1.5 and 2× the resolution of the low resolution simulation.

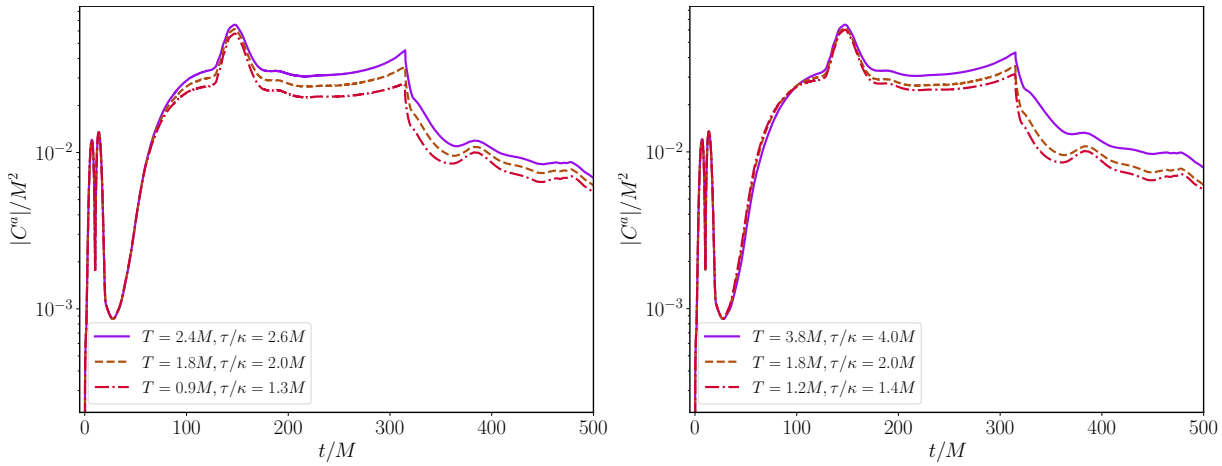


Figure 5.6: Integrated norm of the constraint violation C_a as a function of coordinate time (in units of the total mass) for the same equal-mass head-on collision with $\lambda = 0.04m^2$ shown in the right panel of Fig. 5.5 when varying t_1 but keeping t_2 fixed (left), or varying t_2 but keeping t_1 fixed (right). As expected, the constraints decrease with increasing κ.

We particular focused on the EFT formulation of alternatives to GR, which is a powerful phenomenological framework where deviations from GR are introduced by higher-dimensional terms in the action for gravity in an expansion valid up to a certain cut-off energy scale. ESGB theory is a specific example of an EFT of gravity, which has strong theoretical motivations from string theory and as a representative of theories with a scalar field in the gravitational sector. It is also interesting phenomenologically, as it predicts scalar hair around BHs, which may be observable with GWs.

By construction, EFTs introduce higher order derivatives in the equations of motion. These derivatives make it unclear whether the theory admits well-posed initial value problems. We illustrated such pathologies with a toy model, and introduced the "fixing the equations" approach. This approach is motivated by the fact that an EFT is a low-energy approximation to a more complete theory and is only valid up to a certain energy scale. The equations of motion are modified in an "ad hoc" way to control the flow of energy to high frequencies so that the theory remains in its regime of validity.

We presented the results of [57], as part of which shift-symmetric ESGB theory was evolved numerically using the "fixing the equations" approach. Among other results, we showed how the equations of the theory can be modified with auxiliary fields, and how these new equations of motion conserve the constraints of the gauge used to numerically evolve the problem. [5] The results of the study showed that the approach is successful in reproducing the results when solving the original equations (which in this particular case can be solved without approximation thanks to the choice of gauge). In addition, solutions were obtained outside of the regime where the original equations could be solved. This is an example of how the "fixing the equations" approach can be used to explore phenomenologically interesting regimes of EFTs of gravity.

[5] These are the part of the study I contributed to.

Conclusion and future outlook

The objective of this thesis was to develop and study data analysis methods to test BM physics in GW data. This is motivated by the expected increase in the number of GW detections and sensitivity of GW detectors in the coming years and the next generation of detectors. All these factors will reduce the statistical uncertainty in physical inference and bring systematic uncertainties to the forefront. Developing methods to detect and understand these systematic uncertainties is, therefore, a pressing aspect of GW astronomy.

With this goal in mind, we developed the `SCoRe` framework, a method to detect and provide interpretability both to known but unprecise modelled physics and to unknown physics. In Chapter 2, we explained the formalism of the method and showed its application to toy models in Chapter 3. The method has three main components, each aimed at a different challenge in tests of the SM of GWs. First, we leverage the observation that noise in GW detectors is for the majority uncorrelated between detectors by cross-correlating the residual power in pairs of detectors. Second, we filter the cross-correlated power for physically motivated behaviour by projecting onto physically motivated or agnostic bases. This can further reduce the effect of noise, particularly transient, in the detection of BM signatures. Finally, we combine information from different events to inform on the origin of the BM signature by assuming a dependence of the BM signature on the source parameters. BM signatures generally do not affect all parts of the parameter space identically. As an example we used throughout the thesis, the effect of higher-order terms in an EFT of gravity may preferentially affect BBHs of smaller masses. We can use this dependence when hierarchically combining information from events to obtain a more physically informative measure of the BM signature—in our example, the energy dimension of the leading order term in the EFT of gravity.

We demonstrated the last step on a population of BBH mergers as expected to be observed by a network of 3G detectors in Chapter 4. We notably showed the possible constraints that can be placed on the BM signature with up to 10^5 events. A result that may not be surprising is that the precision of the constraint drops as the energy dimension

of the EFT terms increases. This is due to the power law fall-off of the BM signature with the mass, which is steeper for higher dimensional operators, causing fewer events to have information on the BM signature.

The next step in showcasing the capabilities of the method would be to apply it to the data from the current and past observing runs. Obtaining constraints on BM signature from the current catalogues using the `SCoRe` method is an essential step in checking the method's applicability. The currently available catalogues (GWTC-1–3 [12, 17, 23]), contain ~ 100, while the currently O4a observation has on the order of $\sim$ candidate events on the public event database (GraceDB). With several hundreds of events, the method can be tested for its ability to combine information from different events.

An important assumption in the method is that noise is uncorrelated between detectors. This is not expected to hold in 3G detectors—magnetic coupling, which is expected to cause cross-correlated noise above 3G (ET and CE) sensitivity curves for < 100 Hz [119]. Investigating the effect of correlated noise on the `SCoRe` method would be a valuable next step, although we note that correlated noise itself can be considered a source of unmodeled physics, and the `SCoRe` method could be used to detect and quantify this effect. Along similar lines, probing the effect of glitches on the identification of BM signatures with the `SCoRe` method is another possible extension of this work.

A pivotal design concept of `SCoRe` is flexibility in the choice of templates used to model the CRPS. In this thesis, we have limited ourselves to agnostic templates, capturing "chirp-like" behaviour, and physically motivated templates capturing leading order phase deviations in an EFT of gravity. A survey of the recoverability of different physical models, such as the effect of micro-lensing, environmental effects, or parametrized deviations such as PN deviations would be a valuable measure of the range of the method.

Although adding the assumption of dependence on source parameters can be a valuable tool in the inference of BM signatures, the success of the method relies on understanding the effect of the distribution of source parameters. For example, correlation in the spin and mass of the compact objects may affect the inference of the BM signature. Such population effects and their impact on the hierarchical inference we perform in `SCoRe` warrant further investigation.

Another simple extension of the work in Chapter 4 would be to quantify the information different sectors of the parameter space (i.e different mass ranges) provide on the inference of the BM model (the power law coefficients defining the dependence on chirp mass). Generally, two effects can come into play: BM effects may be more prominent in certain regions of parameters space, while the distribution of *detected* events covers regions better than others. In the case of the power law scaling of the BM signature with the chirp mass,

the BM effect is strongest for low mass BBH mergers. While the source mass distribution is also a decaying power law, it is currently understood to have a paucity at low masses, so it is not clear which regions of the mass spectrum provide the most information for the inference.

Each of the three main components of the `SCoRe` method is applicable independently. A straightforward investigation would be to include the assumption of source parameter dependence of the BM signature to current tests included in the LVK testing GR papers. For example, re-running the hierarchical inference on the previous catalogues but assuming a power law dependence of the PN deviation coefficients on the chirp mass of the source.

The `SCoRe` method is designed as a data-driven method, which aims to make minimal assumptions about the origin of the BM signature. In chapter 5, we gave a brief introduction to challenges faced in computing GW signals for theory-specific tests of the SM. In particular, we discussed the difficulty in defining a well-posed initial value problem for ESGB theory. We describe the "fixing the equations" method of making a problem well-posed so that numerical simulations can be performed to compute GW signals in the theory, and discussed its application to ESGB theory.

The field of GW astronomy is rapidly evolving. With the prospect of ever-increasing detections and sensitivity, GW science is poised to become increasingly data-driven. The ideas developed in this thesis will hopefully be helpful in the coming years as the need to better understand what our models may be missing in the data becomes more pressing.

References

[1] A. Nitz *et al.* Gwastro/pycbc: V2.0.2 release of PyCBC. Zenodo, March 2022.

[2] Abbott *et al.* (LIGO Scientific Collaboration). Population of Merging Compact Binaries Inferred Using Gravitational Waves through GWTC-3. *Physical Review X*, 13(1):011048, March 2023.

[3] Jahed Abedi, Hannah Dykaar, and Niayesh Afshordi. Echoes from the abyss: Tentative evidence for Planck-scale structure at black hole horizons. *Physical Review D*, 96(8):082004, October 2017.

[4] M. Abernathy, F. Acernese, P. Ajith, B. Allen, P. Amaro Seoane, N. Andersson, et al. Einstein gravitational wave telescope conceptual design study. Technical report, EGO, May 2011.

[5] Michalis Agathos, Walter Del Pozzo, Tjonnie G. F. Li, Chris Van Den Broeck, John Veitch, and Salvatore Vitale. TIGER: A data analysis pipeline for testing the strong-field dynamics of general relativity with gravitational wave signals from coalescing compact binaries. *Physical Review D*, 89(8):082001, April 2014.

[6] Bruce Allen and Joseph D. Romano. Detecting a stochastic background of gravitational radiation: Signal processing strategies and sensitivities. *Physical Review D*, 59(10):102001, March 1999.

[7] Gwyneth Allwright and Luis Lehner. Towards the nonlinear regime in extensions to GR: Assessing possible options. *Classical and Quantum Gravity*, 36(8):084001, April 2019.

[8] Gregory Ashton, Ofek Birnholtz, Miriam Cabero, Collin Capano, Thomas Dent, Badri Krishnan, Grant David Meadors, Alex B. Nielsen, Alex Nitz, and Julian Westerweck. Comments on: "Echoes from the abyss: Evidence for Planck-scale structure at black hole horizons", December 2016.

[9] B. P. Abbott *et al.* (LIGO Scientific and Virgo Collaborations). Characterization of transient noise in Advanced LIGO relevant to gravitational wave signal GW150914. *Classical and Quantum Gravity*, 33(13):134001, June 2016.

[10] B. P. Abbott *et al.* (LIGO Scientific and Virgo Collaborations). Observation of Gravitational Waves from a Binary Black Hole Merger. *Physical Review Letters*, 116(6):061102, February 2016.

[11] B. P. Abbott *et al.* (LIGO Scientific and Virgo Collaborations). Tests of General Relativity with GW150914. *Physical Review Letters*, 116(22):221101, May 2016.

[12] B. P. Abbott *et al.* (LIGO Scientific and Virgo Collaborations). GWTC-1: A Gravitational-Wave Transient Catalog of Compact Binary Mergers Observed by LIGO and Virgo during the First and Second Observing Runs. *Physical Review X*, 9(3):031040, September 2019.

[13] B. P. Abbott *et al.* (LIGO Scientific and Virgo Collaborations). Tests of General Relativity with GW170817. *Physical Review Letters*, 123(1):011102, July 2019.

[14] B. P. Abbott *et al.* (LIGO Scientific and Virgo Collaborations). Tests of general relativity with the binary black hole signals from the LIGO-Virgo catalog GWTC-1. *Physical Review D*, 100(10):104036, November 2019.

[15] B. P. Abbott *et al.* (LIGO Scientific and Virgo Collaborations). A guide to LIGO–Virgo detector noise and extraction of transient gravitational-wave signals. *Classical and Quantum Gravity*, 37(5):055002, February 2020.

[16] B. P. Abbott *et al.* (LIGO Scientific and Virgo Collaborations). Properties and Astrophysical Implications of the 150 $M_{\odot}$ Binary Black Hole Merger GW190521. *The Astrophysical Journal*, 900(1):L13, September 2020.

[17] B. P. Abbott *et al.* (LIGO Scientific and Virgo Collaborations). GWTC-2: Compact Binary Coalescences Observed by LIGO and Virgo During the First Half of the Third Observing Run. *Physical Review X*, 11(2):021053, June 2021.

[18] B. P. Abbott *et al.* (LIGO Scientific and Virgo Collaborations). Tests of General Relativity with Binary Black Holes from the second LIGO-Virgo Gravitational-Wave Transient Catalog. *Physical Review D*, 103(12):122002, June 2021.

[19] B. P. Abbott *et al.* (LIGO Scientific Collaboration). Analysis of first LIGO science data for stochastic gravitational waves. *Physical Review D*, 69(12):122004, June 2004.

[20] B. P. Abbott *et al.* (LIGO Scientific Collaborations). LIGO: The Laser Interferometer Gravitational-Wave Observatory. *Reports on Progress in Physics*, 72(7):076901, June 2009.

[21] B. P. Abbott *et al.* (LIGO Scientific, Virgo, and KAGRA Collaborations). Prospects for observing and localizing gravitational-wave transients with Advanced LIGO, Advanced Virgo and KAGRA. *Living Reviews in Relativity*, 23(1):3, September 2020.

[22] B. P. Abbott *et al.* (LIGO Scientific, Virgo and KAGRA Collaborations). All-sky search for short gravitational-wave bursts in the third Advanced LIGO and Advanced Virgo run. *Physical Review D*, 104(12):122004, December 2021.

[23] B. P. Abbott *et al.* (LIGO Scientific, Virgo, and KAGRA Collaborations). GWTC-3: Compact Binary Coalescences Observed by LIGO and Virgo During the Second Part of the Third Observing Run. *arXiv:2111.03606*, November 2021.

[24] B. P. Abbott *et al.* (LIGO Scientific, Virgo and KAGRA Collaborations). Tests of General Relativity with GWTC-3, December 2021.

[25] Stanislav Babak, Martin Hewitson, and Antoine Petiteau. LISA Sensitivity and SNR Calculations, 2021.

[26] Enrico Barausse et al. Prospects for Fundamental Physics with LISA. *Gen. Rel. Grav.*, 52(8):81, 2020.

[27] Enrico Barausse, Carlos Palenzuela, Marcelo Ponce, and Luis Lehner. Neutron-star mergers in scalar-tensor theories of gravity. *Phys. Rev. D*, 87:081506, 2013.

[28] Thomas Bayes and Robert Price. LII. An essay towards solving a problem in the doctrine of chances. By the late Rev. Mr. Bayes, F. R. S. communicated by Mr. Price, in a letter to John Canton, A. M. F. R. S. *Philosophical Transactions of the Royal Society of London*, 53:370–418, January 1763.

[29] Enis Belgacem, Yves Dirian, Stefano Foffa, and Michele Maggiore. The gravitational-wave luminosity distance in modified gravity theories. *Physical Review D*, 97(10):104066, May 2018.

[30] Enis Belgacem, Yves Dirian, Stefano Foffa, and Michele Maggiore. Modified gravitational-wave propagation and standard sirens. *Phys. Rev. D*, 98(2):023510, 2018.

[31] Laura Bernard. Dynamics of compact binary systems in scalar-tensor theories: Equations of motion to the third post-Newtonian order. *Phys. Rev. D*, 98(4):044004, 2018.

[32] Emanuele Berti, Vitor Cardoso, and Clifford M. Will. Gravitational-wave spectroscopy of massive black holes with the space interferometer LISA. *Physical Review D*, 73(6):064030, March 2006.

[33] Miguel Bezares, Ricard Aguilera-Miret, Lotte Ter Haar, Marco Crisostomi, Carlos Palenzuela, and Enrico Barausse. No Evidence of Kinetic Screening in Simulations of Merging Binary Neutron Stars beyond General Relativity. *Physical Review Letters*, 128(9):091103, March 2022.

[34] Miguel Bezares, Lotte ter Haar, Marco Crisostomi, Enrico Barausse, and Carlos Palenzuela. Kinetic screening in nonlinear stellar oscillations and gravitational collapse. *Phys. Rev. D*, 104(4):044022, 2021.

[35] Sajad A. Bhat, Pankaj Saini, Marc Favata, and K. G. Arun. Systematic bias on the inspiral-merger-ringdown consistency test due to neglect of orbital eccentricity, July 2022.

[36] S. Borhanian. GWBENCH: A novel Fisher information package for gravitational-wave benchmarking. *Classical and Quantum Gravity*, 38(17):175014, August 2021.

[37] A. Buonanno and T. Damour. Effective one-body approach to general relativistic two-body dynamics. *Physical Review D*, 59(8):084006, March 1999.

[38] Alessandra Buonanno and Thibault Damour. Transition from inspiral to plunge in binary black hole coalescences. *Phys. Rev. D*, 62:064015, 2000.

[39] Alessandra Buonanno, Lawrence E. Kidder, and Luis Lehner. Estimating the final spin of a binary black hole coalescence. *Phys. Rev. D*, 77:026004, 2008.

[40] C. P. Burgess and M. Williams. Who you gonna call? Runaway ghosts, higher derivatives and time-dependence in EFTs. *Journal of High Energy Physics*, 2014(8):74, August 2014.

[41] Cliff P. Burgess. Quantum Gravity in Everyday Life: General Relativity as an Effective Field Theory. *Living Reviews in Relativity*, 7(1):5, December 2004.

[42] Thomas A. Callister, Carl-Johan Haster, Ken K. Y. Ng, Salvatore Vitale, and Will M. Farr. Who Ordered That? Unequal-mass Binary Black Hole Mergers Have Larger Effective Spins. *The Astrophysical Journal Letters*, 922(1):L5, November 2021.

[43] Pablo A. Cano, Kwinten Fransen, Thomas Hertog, and Simon Maenaut. Gravitational ringing of rotating black holes in higher-derivative gravity. *Phys. Rev. D*, 105(2):024064, 2022.

[44] Vitor Cardoso, Edgardo Franzin, and Paolo Pani. Is the Gravitational-Wave Ringdown a Probe of the Event Horizon? *Physical Review Letters*, 116(17):171101, April 2016.

[45] Vitor Cardoso, Seth Hopper, Caio F. B. Macedo, Carlos Palenzuela, and Paolo Pani. Gravitational-wave signatures of exotic compact objects and of quantum corrections at the horizon scale. *Physical Review D*, 94(8):084031, October 2016.

[46] Vitor Cardoso, Masashi Kimura, Andrea Maselli, and Leonardo Senatore. Black Holes in an Effective Field Theory Extension of General Relativity. *Phys. Rev. Lett.*, 121(25):251105, 2018.

[47] Vitor Cardoso and Paolo Pani. Tests for the existence of black holes through gravitational wave echoes. *Nature Astronomy*, 1(9):586–591, September 2017.

[48] B. Carter. Axisymmetric Black Hole Has Only Two Degrees of Freedom. *Physical Review Letters*, 26(6):331–333, February 1971.

[49] Juan Cayuso, Néstor Ortiz, and Luis Lehner. Fixing extensions to General Relativity in the non-linear regime. *Physical Review D*, 96(8):084043, October 2017.

[50] Ramiro Cayuso. Gravitational collapse in quadratic gravity. *Physical Review D*, 108(12):124066, December 2023.

[51] Ramiro Cayuso, Pau Figueras, Tiago França, and Luis Lehner. Self-Consistent Modeling of Gravitational Theories beyond General Relativity. *Physical Review Letters*, 131(11):111403, September 2023.

[52] Ramiro Cayuso and Luis Lehner. Nonlinear, noniterative treatment of EFT-motivated gravity. *Phys. Rev. D*, 102(8):084008, 2020.

[53] Ramiro Cayuso and Luis Lehner. Nonlinear, noniterative treatment of EFT-motivated gravity. *Physical Review D*, 102(8):084008, October 2020.

[54] Joan Centrella, John G. Baker, Bernard J. Kelly, and James R. Van Meter. Black-hole binaries, gravitational waves, and numerical relativity. *Reviews of Modern Physics*, 82(4):3069–3119, November 2010.

[55] Katerina Chatziioannou, Carl-Johan Haster, Tyson B. Littenberg, Will M. Farr, Sudarshan Ghonge, Margaret Millhouse, James A. Clark, and Neil Cornish. Noise spectral estimation methods and their impact on gravitational wave measurement of compact binary mergers. *Physical Review D*, 100(10):104004, November 2019.

[56] The LIGO Scientific Collaboration. Advanced LIGO. *Classical and Quantum Gravity*, 32(7):074001, April 2015.

[57] Maxence Corman, Luis Lehner, William E. East, and Guillaume Dideron. Nonlinear studies of modifications to general relativity: Comparing different approaches, May 2024.

[58] Maxence Corman, Justin L. Ripley, and William E. East. Nonlinear studies of binary black hole mergers in Einstein-scalar-Gauss-Bonnet gravity, October 2022.

[59] Neil J. Cornish and Tyson B. Littenberg. Bayeswave: Bayesian inference for gravitational wave bursts and instrument glitches. *Classical and Quantum Gravity*, 32(13):135012, June 2015.

[60] Neil J. Cornish, Tyson B. Littenberg, Bence Bécsy, Katerina Chatziioannou, James A. Clark, Sudarshan Ghonge, and Margaret Millhouse. BayesWave analysis pipeline in the era of gravitational wave observations. *Physical Review D*, 103(4):044006, February 2021.

[61] Jolien D. E. Creighton and Warren G. Anderson. *Gravitational-Wave Physics and Astronomy: An Introduction to Theory, Experiment and Data Analysis*. Wiley Series in Cosmology. Wiley-VCH, Weinheim, Germany, 2011.

[62] D. Reitze *et al.* Cosmic Explorer: The U.S. Contribution to Gravitational-Wave Astronomy beyond LIGO. *Bulletin of the AAS*, 51(7), September 2019.

[63] T. Damour. Gravitational radiation and the motion of compact bodies. *Lecture Notes in Physics, Berlin Springer Verlag*, 124:59–144, January 1983.

[64] Thibault Damour and Gilles Esposito-Farese. Tensor multiscalar theories of gravitation. *Class. Quant. Grav.*, 9:2093–2176, 1992.

[65] Thibault Damour, Alessandro Nagar, and Loïc Villain. Measurability of the tidal polarizability of neutron stars in late-inspiral gravitational-wave signals. *Physical Review D*, 85(12):123007, June 2012.

[66] Thibault Damour, Michael Soffel, and Chongming Xu. General-relativistic celestial mechanics II. Translational equations of motion. *Physical Review D*, 45(4):1017–1044, February 1992.

[67] Ulf Danielsson, Luis Lehner, and Frans Pretorius. Dynamics and Observational Signatures of Shell-like Black Hole Mimickers. *Physical Review D*, 104(12):124011, December 2021.

[68] Claudia De Rham. Massive Gravity. *Living Reviews in Relativity*, 17(1):7, December 2014.

[69] Claudia de Rham, Lavinia Heisenberg, and Andrew J. Tolley. Spin-2 fields and the weak gravity conjecture. *Phys. Rev. D*, 100(10):104033, 2019.

[70] Sanjeev Dhurandhar, Badri Krishnan, Himan Mukhopadhyay, and John T. Whelan. Cross-correlation search for periodic gravitational waves. *Phys. Rev. D*, 77:082001, 2008.

[71] Guillaume Dideron, Suvodip Mukherjee, and Luis Lehner. New framework to study unmodeled physics from gravitational wave data. *Physical Review D*, 107(10):104023, May 2023.

[72] Tim Dietrich, Sebastiano Bernuzzi, and Wolfgang Tichy. Closed-form tidal approximants for binary neutron star gravitational waveforms constructed from high-resolution numerical relativity simulations. *Physical Review D*, 96(12):121501, December 2017.

[73] Tim Dietrich, Anuradha Samajdar, Sebastian Khan, Nathan K. Johnson-McDaniel, Reetika Dudi, and Wolfgang Tichy. Improving the NRTidal model for binary neutron star systems. *Physical Review D*, 100(4):044003, August 2019.

[74] John F. Donoghue. General relativity as an effective field theory: The leading quantum corrections. *Physical Review D*, 50(6):3874–3888, September 1994.

[75] John F. Donoghue. Introduction to the Effective Field Theory Description of Gravity, December 1995.

[76] John F. Donoghue. The effective field theory treatment of quantum gravity. In *The sixth international school on field theory and gravitation-2012*, pages 73–94, Petrpolis - RJ, Brazil, 2012.

[77] Olaf Dreyer, Bernard Kelly, Badri Krishnan, Lee Samuel Finn, David Garrison, and Ramon Lopez-Aleman. Black-hole spectroscopy: Testing general relativity through gravitational-wave observations. *Classical and Quantum Gravity*, 21(4):787–803, January 2004.

[78] Freeman J. Dyson. Gravitational Machines, May 2023.

[79] Douglas M. Eardley, David L. Lee, and Alan P. Lightman. Gravitational-Wave Observations as a Tool for Testing Relativistic Gravity. *Physical Review D*, 8(10):3308–3321, November 1973.

[80] Douglas M. Eardley, David L. Lee, and Alan P. Lightman. Gravitational-Wave Observations as a Tool for Testing Relativistic Gravity. *Physical Review D*, 8(10):3308–3321, November 1973.

[81] William E. East and Justin L. Ripley. Dynamics of spontaneous black hole scalarization and mergers in Einstein-scalar-Gauss-Bonnet gravity. *Physical Review Letters*, 127(10):101102, September 2021.

[82] William E. East and Justin L. Ripley. Evolution of Einstein-scalar-Gauss-Bonnet gravity using a modified harmonic formulation. *Physical Review D*, 103(4):044040, February 2021.

[83] Fernando Echeverria. *Topics in General Relativity Theory : Gravitational-Wave Measurements of Black-Hole Parameters; Gravitational Collapse of a Cylindrical Body; and Classical-Particle Evolution in the Presence of Closed, Timelike Curves*. PhD thesis, California Institute of Technology, December 2008.

[84] Arthur Eddington, S. The propagation of gravitational waves. *Proceedings of the Royal Society of London. Series A, Containing Papers of a Mathematical and Physical Character*, 102(716):268–282, December 1922.

[85] Bruce Edelman, F. J. Rivera-Paleo, J. D. Merritt, Ben Farr, Zoheyr Doctor, Jeandrew Brink, Will M. Farr, Jonathan Gair, Joey Shapiro Key, Jess McIver, and Alex B. Nielsen. Constraining unmodeled physics with compact binary mergers from GWTC-1. *Physical Review D*, 103(4):042004, February 2021.

[86] Oliver Edy, Andrew Lundgren, and Laura K. Nuttall. Issues of mismodeling gravitational-wave data for parameter estimation. *Physical Review D*, 103(12):124061, June 2021.

[87] Albert Einstein. Näherungsweise Integration der Feldgleichungen der Gravitation. *Sitzungsberichte der Königlich Preussischen Akademie der Wissenschaften*, pages 688–696, January 1916.

[88] Albert Einstein. Über Gravitationswellen. *Sitzungsberichte der Königlich Preussischen Akademie der Wissenschaften*, pages 154–167, January 1918.

[89] Solomon Endlich, Victor Gorbenko, Junwu Huang, and Leonardo Senatore. An effective formalism for testing extensions to General Relativity with gravitational waves. *Journal of High Energy Physics*, 2017(9):122, September 2017.

[90] Rana X Adhikari et al. Ligo voyager upgrade: Design concept. Technical Report LIGO-T1400226-v10, LIGO Scientific Collaboration, May 2024. Technical Note.

[91] Matthew *et al.* Evans. A Horizon Study for Cosmic Explorer: Science, Observatories, and Community, October 2021.

[92] Joshua A. Faber and Frederic A. Rasio. Binary Neutron Star Mergers. *Living Reviews in Relativity*, 15(1):8, July 2012.

[93] Stephen Fairhurst. Localization of transient gravitational wave sources: Beyond triangulation. *Classical and Quantum Gravity*, 35(10):105002, April 2018.

[94] Éanna É. Flanagan and Tanja Hinderer. Constraining neutron-star tidal Love numbers with gravitational-wave detectors. *Physical Review D*, 77(2):021502, January 2008.

[95] William A. Fowler and F. Hoyle. Neutrino Processes and Pair Formation in Massive Stars and Supernovae. *The Astrophysical Journal Supplement Series*, 9:201, December 1964.

[96] Gary S. Fraley. Supernovae explosions induced by pair-production instability. *Astrophysics and Space Science*, 2(1):96–114, August 1968.

[97] Nicola Franchini, Miguel Bezares, Enrico Barausse, and Luis Lehner. Fixing the dynamical evolution in scalar-Gauss-Bonnet gravity. 5 2022.

[98] Jonathan R Gair, Andrea Antonelli, and Riccardo Barbieri. A Fisher matrix for gravitational-wave population inference. *Monthly Notices of the Royal Astronomical Society*, 519(2):2736–2753, February 2023.

[99] Robert Geroch. Relativistic theories of dissipative fluids. *Journal of Mathematical Physics*, 36(8):4226–4241, 08 1995.

[100] Gian F. Giudice, Matthew McCullough, and Alfredo Urbano. Hunting for Dark Particles with Gravitational Waves. *Journal of Cosmology and Astroparticle Physics*, 2016(10):001–001, October 2016.

[101] S. Gossan, J. Veitch, and B. S. Sathyaprakash. Bayesian model selection for testing the no-hair theorem with black hole ringdowns. *Physical Review D*, 85(12):124056, June 2012.

[102] The LSC Post-O5 Study Group. Report of the lsc post-o5 study group. Technical Report LIGO-T2200287, LIGO, 2022.

[103] Carsten Gundlach, Gioel Calabrese, Ian Hinder, and José M Martín-García. Constraint damping in the z4 formulation and harmonic gauge. *Classical and Quantum Gravity*, 22(17):3767–3773, August 2005.

[104] Anuradha et al. Gupta. Possible Causes of False General Relativity Violations in Gravitational Wave Observations, 2024.

[105] J. Hadamard. Sur les problèmes aux dérivés partielles et leur signification physique. *Princeton University Bulletin*, 13:49–52, 1902.

[106] Mark Hannam. Status of black-hole-binary simulations for gravitational-wave detection. *Classical and Quantum Gravity*, 26(11):114001, June 2009.

[107] Eric W. Hirschmann, Luis Lehner, Steven L. Liebling, and Carlos Palenzuela. Black hole dynamics in Einstein-Maxwell-dilaton theory. *Physical Review D*, 97(6):064032, March 2018.

[108] David W. Hogg. Distance measures in cosmology, December 2000.

[109] Kenta Hotokezaka, Koutarou Kyutoku, and Masaru Shibata. Exploring tidal effects of coalescing binary neutron stars in numerical relativity. *Physical Review D*, 87(4):044001, February 2013.

[110] Qian Hu and John Veitch. Accumulating errors in tests of general relativity with the Einstein Telescope: Overlapping signals and inaccurate waveforms, October 2022.

[111] R. A. Hulse and J. H. Taylor. Discovery of a pulsar in a binary system. *The Astrophysical Journal*, 195:L51, January 1975.

[112] Sascha Husa, Sebastian Khan, Mark Hannam, Michael Pürrer, Frank Ohme, Xisco Jiménez Forteza, and Alejandro Bohé. Frequency-domain gravitational waves from nonprecessing black-hole binaries. I. New numerical waveforms and anatomy of the signal. *Physical Review D*, 93(4):044006, February 2016.

[113] Francesco Iacovelli, Michele Mancarella, Stefano Foffa, and Michele Maggiore. Forecasting the Detection Capabilities of Third-generation Gravitational-wave Detectors Using GWFAST. *The Astrophysical Journal*, 941(2):208, December 2022.

[114] Maximiliano Isi, Will M. Farr, and Katerina Chatziioannou. Comparing Bayes factors and hierarchical inference for testing general relativity with gravitational waves, April 2022.

[115] W. Israel. Nonstationary irreversible thermodynamics: A Causal relativistic theory. *Annals Phys.*, 100:310–331, 1976.

[116] W. Israel and J. M. Stewart. Thermodynamics of nonstationary and transient effects in a relativistic gas. *Physics Letters A*, 58(4):213–215, September 1976.

[117] J. Meidam *et al.* Parametrized tests of the strong-field dynamics of general relativity using gravitational wave signals from coalescing binary black holes: Fast likelihood calculations and sensitivity of the method. *Physical Review D*, 97(4):044033, February 2018.

[118] Kamiel Janssens. Prospects for an isotropic gravitational wave background detection with Earth-based interferometric detectors and the threat of correlated noise, May 2023.

[119] Kamiel Janssens, Matthew Ball, Robert M. S. Schofield, Nelson Christensen, Raymond Frey, Nick van Remortel, Sharan Banagiri, Michael W. Coughlin, Anamaria Effler, Mark Gołkowski, Jerzy Kubisz, and Michał Ostrowski. Correlated 1–1000 Hz magnetic field fluctuations from lightning over Earth-scale distances and their impact on gravitational wave searches. *Physical Review D*, 107(2):022004, January 2023.

[120] Piotr Jaranowski and Andrzej Królak. Gravitational-Wave Data Analysis. Formalism and Sample Applications: The Gaussian Case. *Living Reviews in Relativity*, 15(1):4, March 2012.

[121] Piotr Jaranowski, Andrzej Królak, and Bernard F. Schutz. Data analysis of gravitational-wave signals from spinning neutron stars. I. The signal and its detection. *Physical Review D*, 58(6):063001, August 1998.

[122] Nathan K. Johnson-McDaniel, Abhirup Ghosh, Sudarshan Ghonge, Muhammed Saleem, N. V. Krishnendu, and James A. Clark. Investigating the relation between gravitational wave tests of general relativity. *Phys. Rev. D*, 105(4):044020, 2022.

[123] Christos Karathanasis, Suvodip Mukherjee, and Simone Mastrogiovanni. Binary black holes population and cosmology in new lights: Signature of PISN mass and formation channel in GWTC-3. *Monthly Notices of the Royal Astronomical Society*, 523(3):4539–4555, August 2023.

[124] R. P. Kerr and A. Schild. Republication of: A new class of vacuum solutions of the Einstein field equations. *General Relativity and Gravitation*, 41(10):2485–2499, October 2009.

[125] Michael Kesden. Can binary mergers produce maximally spinning black holes? *Phys. Rev. D*, 78:084030, 2008.

[126] Sebastian Khan, Sascha Husa, Mark Hannam, Frank Ohme, Michael Pürrer, Xisco Jiménez Forteza, and Alejandro Bohé. Frequency-domain gravitational waves from nonprecessing black-hole binaries. II. A phenomenological model for the advanced detector era. *Physical Review D*, 93(4):044007, February 2016.

[127] Remko Klein and Diederik Roest. Exorcising the Ostrogradsky ghost in coupled systems. *Journal of High Energy Physics*, 2016(7):130, July 2016.

[128] S Klimenko and G Mitselmakher. A wavelet method for detection of gravitational wave bursts. *Classical and Quantum Gravity*, 21(20):S1819–S1830, October 2004.

[129] S. Klimenko, S. Mohanty, M. Rakhmanov, and G. Mitselmakher. Constraint likelihood analysis for a network of gravitational wave detectors. *Physical Review D*, 72(12):122002, December 2005.

[130] S Klimenko, S Mohanty, M Rakhmanov, and G Mitselmakher. Constraint likelihood method: Generalization for colored noise. *Journal of Physics: Conference Series*, 32:12–17, March 2006.

[131] S. Klimenko, G. Vedovato, M. Drago, G. Mazzolo, G. Mitselmakher, C. Pankow, G. Prodi, V. Re, F. Salemi, and I. Yakushin. Localization of gravitational wave sources with networks of advanced detectors. *Physical Review D*, 83(10):102001, May 2011.

[132] S. Klimenko, G. Vedovato, M. Drago, F. Salemi, V. Tiwari, G. A. Prodi, C. Lazzaro, K. Ackley, S. Tiwari, C. F. Da Silva, and G. Mitselmakher. Method for detection and reconstruction of gravitational wave transients with networks of advanced detectors. *Physical Review D*, 93(4):042004, February 2016.

[133] T. Kobayashi, M. Yamaguchi, and J. Yokoyama. Generalized G-Inflation: –Inflation with the Most General Second-Order Field Equations–. *Progress of Theoretical Physics*, 126(3):511–529, September 2011.

[134] V. Alan Kostelecký and Matthew Mewes. Testing local Lorentz invariance with gravitational waves. *Physics Letters B*, 757:510–514, June 2016.

[135] Aron D. Kovacs and Harvey S. Reall. Well-posed formulation of Lovelock and Horndeski theories. *Physical Review D*, 101(12):124003, June 2020.

[136] Áron D. Kovács and Harvey S. Reall. Well-Posed Formulation of Scalar-Tensor Effective Field Theory. *Physical Review Letters*, 124(22):221101, June 2020.

[137] Ely D. Kovetz, Ilias Cholis, Patrick C. Breysse, and Marc Kamionkowski. Black hole mass function from gravitational wave measurements. *Physical Review D*, 95:103010, May 2017.

[138] N. V. Krishnendu, K. G. Arun, and Chandra Kant Mishra. Testing the Binary Black Hole Nature of a Compact Binary Coalescence. *Physical Review Letters*, 119(9):091101, August 2017.

[139] Jack Y. L. Kwok, Rico K. L. Lo, Alan J. Weinstein, and Tjonnie G. F. Li. Investigation of the effects of non-Gaussian noise transients and their mitigation in parameterized gravitational-wave tests of general relativity. *Physical Review D*, 105(2):024066, January 2022.

[140] L. Blackburn *et al.* The LSC glitch group: Monitoring noise transients during the fifth LIGO science run. *Classical and Quantum Gravity*, 25(18):184004, September 2008.

[141] William G. Laarakkers and Eric Poisson. Quadrupole Moments of Rotating Neutron Stars. *The Astrophysical Journal*, 512(1):282, February 1999.

[142] Guillermo Lara, Miguel Bezares, and Enrico Barausse. UV completions, fixing the equations, and nonlinearities in k-essence. *Phys. Rev. D*, 105(6):064058, 2022.

[143] Luis Lehner. Numerical Relativity: A review. *Classical and Quantum Gravity*, 18(17):R25–R86, September 2001.

[144] Luis Lehner and Frans Pretorius. Numerical Relativity and Astrophysics. *Annual Review of Astronomy and Astrophysics*, 52(1):661–694, August 2014.

[145] Steven L. Liebling and Carlos Palenzuela. Dynamical Boson Stars. *Living Reviews in Relativity*, 15(1):6, May 2012.

[146] LIGO O4 Detector Collaboration. Broadband Quantum Enhancement of the LIGO Detectors with Frequency-Dependent Squeezing. *Physical Review X*, 13(4):041021, October 2023.

[147] LIGO Scientific Collaboration. LIGO Algorithm Library - LALSuite. free software (GPL), 2018.

[148] David Lovelock. The Einstein Tensor and Its Generalizations. *Journal of Mathematical Physics*, 12(3):498–501, March 1971.

[149] Zhenwei Lyu, Nan Jiang, and Kent Yagi. Constraints on Einstein-dilation-Gauss-Bonnet gravity from Black Hole-Neutron Star Gravitational Wave Events. *Physical Review D*, 105(6):064001, March 2022.

[150] M. Puntuto *et al.* The Einstein Telescope: A third-generation gravitational wave observatory. *Classical and Quantum Gravity*, 27(19):194002, September 2010.

[151] Piero Madau and Mark Dickinson. Cosmic Star-Formation History. *Annual Review of Astronomy and Astrophysics*, 52(1):415–486, 2014.

[152] *et al.* Maggiore. Science case for the Einstein telescope. *Journal of Cosmology and Astroparticle Physics*, 2020(03):050–050, March 2020.

[153] Michele Maggiore. *Gravitational Waves: Volume 1: Theory and Experiments*. OUP Oxford, October 2007.

[154] S. Mastrogiovanni, D. A. Steer, and M. Barsuglia. Probing modified gravity theories and cosmology using gravitational-waves and associated electromagnetic counterparts. *Phys. Rev. D*, 102(4):044009, 2020.

[155] Pawel O. Mazur and Emil Mottola. Gravitational vacuum condensate stars. *Proceedings of the National Academy of Sciences*, 101(26):9545–9550, June 2004.

[156] Sean T. McWilliams. Analytical Black-Hole Binary Merger Waveforms. *Phys. Rev. Lett.*, 122(19):191102, 2019.

[157] Ajit Kumar Mehta, Alessandra Buonanno, Roberto Cotesta, Abhirup Ghosh, Noah Sennett, and Jan Steinhoff. Tests of General Relativity with Gravitational-Wave Observations using a Flexible–Theory-Independent Method, March 2022.

[158] J. Meidam, M. Agathos, C. Van Den Broeck, J. Veitch, and B. S. Sathyaprakash. Testing the no-hair theorem with black hole ringdowns using TIGER. *Physical Review D*, 90(6):064009, September 2014.

[159] Matthew Mewes. Signals for Lorentz violation in gravitational waves. *Physical Review D*, 99(10):104062, May 2019.

[160] Saeed Mirshekari, Nicolás Yunes, and Clifford M. Will. Constraining Lorentz-violating, modified dispersion relations with gravitational waves. *Physical Review D*, 85(2):024041, January 2012.

[161] Charles W. Misner, Kip S. Thorne, and John Archibald Wheeler. *Gravitation*. W. H. Freeman, San Francisco, 1973.

[162] Suvodip Mukherjee, Benjamin D. Wandelt, and Joseph Silk. Testing the general theory of relativity using gravitational wave propagation from dark standard sirens. *Mon. Not. Roy. Astron. Soc.*, 502(1):1136–1144, 2021.

[163] Remya Nair, Scott Perkins, Hector O. Silva, and Nicolás Yunes. Fundamental Physics Implications for Higher-Curvature Theories from Binary Black Hole Signals in the LIGO-Virgo Catalog GWTC-1. *Physical Review Letters*, 123(19):191101, November 2019.

[164] Ezra Newman and Roger Penrose. An Approach to Gravitational Radiation by a Method of Spin Coefficients. *Journal of Mathematical Physics*, 3(3):566–578, May 1962.

[165] Atsushi Nishizawa. Generalized framework for testing gravity with gravitational-wave propagation. I. Formulation. *Physical Review D*, 97(10):104037, May 2018.

[166] Rui Niu, Xing Zhang, Bo Wang, and Wen Zhao. Constraining Scalar-tensor Theories Using Neutron Star–Black Hole Gravitational Wave Events. *The Astrophysical Journal*, 921(2):149, November 2021.

[167] Maria Okounkova. Numerical relativity simulation of GW150914 in Einstein-dilaton-Gauss-Bonnet gravity. *Physical Review D*, 102(8):084046, October 2020.

[168] Maria Okounkova, Will M. Farr, Maximiliano Isi, and Leo C. Stein. Constraining gravitational wave amplitude birefringence and Chern-Simons gravity with GWTC-2. *Physical Review D*, 106(4):044067, August 2022.

[169] Maria Okounkova, Maximiliano Isi, Katerina Chatziioannou, and Will M. Farr. Gravitational wave inference on a numerical-relativity simulation of a black hole merger beyond general relativity, August 2022.

[170] Maria Okounkova, Leo C. Stein, Mark A. Scheel, and Daniel A. Hemberger. Numerical binary black hole mergers in dynamical Chern-Simons gravity: Scalar field. *Physical Review D*, 96(4):044020, August 2017.

[171] Maria Okounkova, Leo C. Stein, Mark A. Scheel, and Saul A. Teukolsky. Numerical binary black hole collisions in dynamical Chern-Simons gravity. *Physical Review D*, 100(10):104026, November 2019.

[172] Kellie O'Neal-Ault, Quentin G. Bailey, Tyann Dumerchat, Leïla Haegel, and Jay Tasson. Analysis of Birefringence and Dispersion Effects from Spacetime-Symmetry Breaking in Gravitational Waves. *Universe*, 7(10):380, October 2021.

[173] M. Ostrogradsky. Mémoires sur les équations différentielles, relatives au problème des isopérimètres. *Mem. Acad. St. Petersbourg*, 6(4):385–517, 1850.

[174] Feryal Özel, Dimitrios Psaltis, Ramesh Narayan, and Jeffrey E. McClintock. The black hole mass distribution in the galaxy. *The Astrophysical Journal*, 725(2):1918–1927, December 2010.

[175] P. Nguyen *et al.* Environmental noise in advanced LIGO detectors. *Classical and Quantum Gravity*, 38(14):145001, June 2021.

[176] Giuseppe Papallo. On the hyperbolicity of the most general Horndeski theory. *Physical Review D*, 96(12):124036, December 2017.

[177] Giuseppe Papallo and Harvey S. Reall. On the local well-posedness of Lovelock and Horndeski theories. *Physical Review D*, 96(4):044019, August 2017.

[178] Kris Pardo, Maya Fishbach, Daniel E. Holz, and David N. Spergel. Limits on the number of spacetime dimensions from GW170817. *Journal of Cosmology and Astroparticle Physics*, 2018(07):048–048, July 2018.

[179] P. J. E. Peebles and Bharat Ratra. The cosmological constant and dark energy. *Reviews of Modern Physics*, 75(2):559–606, April 2003.

[180] Roger Penrose. Gravitational Collapse and Space-Time Singularities. *Physical Review Letters*, 14(3):57–59, January 1965.

[181] Roger Penrose. Gravitational Collapse: The Role of General Relativity. *Nuovo Cimento Rivista Serie*, 1:252, January 1969.

[182] Scott E. Perkins, Remya Nair, Hector O. Silva, and Nicolas Yunes. Improved gravitational-wave constraints on higher-order curvature theories of gravity. *Physical Review D*, 104(2):024060, July 2021.

[183] Felix A. E. Pirani. Republication of: On the physical significance of the Riemann tensor. *General Relativity and Gravitation*, 41(5):1215–1232, May 2009.

[184] Eric Poisson. Gravitational waves from inspiraling compact binaries: The quadrupole-moment term. *Physical Review D*, 57(8):5287–5290, April 1998.

[185] Eric Poisson and Clifford M. Will. *Gravity: Newtonian, Post-Newtonian, Relativistic*. Cambridge University Press, Cambridge ; New York, 2014.

[186] Michael Pürrer and Carl-Johan Haster. Gravitational waveform accuracy requirements for future ground-based detectors. *Physical Review Research*, 2(2):023151, May 2020.

[187] R. Abbott *et al.* (LIGO Scientific and Virgo Collaborations). Open data from the first and second observing runs of Advanced LIGO and Advanced Virgo. *SoftwareX*, 13:100658, January 2021.

[188] G. Rakavy and G. Shaviv. Instabilities in Highly Evolved Stellar Models. *The Astrophysical Journal*, 148:803, June 1967.

[189] David H. Reitze, Peter R. Saulson, and Hartmut Grote. *Advanced Interferometric Gravitational-Wave Detectors in 2 Volumes*. World Scientific, New Jersey, 2019.

[190] Justin L. Ripley. Numerical relativity for Horndeski gravity, July 2022.

[191] Justin L. Ripley and Frans Pretorius. Gravitational collapse in Einstein dilaton-Gauss–Bonnet gravity. *Class. Quant. Grav.*, 36(13):134001, 2019.

[192] Justin L. Ripley and Frans Pretorius. Dynamics of a Z2 symmetric EdGB gravity in spherical symmetry. *Classical and Quantum Gravity*, 37(15):155003, August 2020.

[193] Justin L. Ripley and Frans Pretorius. Scalarized Black Hole dynamics in Einstein dilaton Gauss-Bonnet Gravity. *Phys. Rev. D*, 101(4):044015, 2020.

[194] D. C. Robinson. Uniqueness of the Kerr Black Hole. *Physical Review Letters*, 34(14):905–906, April 1975.

[195] Isobel Romero-Shaw, Paul D. Lasky, and Eric Thrane. Signs of Eccentricity in Two Gravitational-wave Signals May Indicate a Subpopulation of Dynamically Assembled Binary Black Holes. *The Astrophysical Journal Letters*, 921(2):L31, November 2021.

[196] Fintan D. Ryan. Gravitational waves from the inspiral of a compact object into a massive, axisymmetric body with arbitrary multipole moments. *Physical Review D*, 52(10):5707–5718, November 1995.

[197] Edwin E. Salpeter. The Luminosity Function and Stellar Evolution. *The Astrophysical Journal*, 121:161, January 1955.

[198] Laura Sampson, Nicolás Yunes, Neil Cornish, Marcelo Ponce, Enrico Barausse, Antoine Klein, Carlos Palenzuela, and Luis Lehner. Projected Constraints on Scalarization with Gravitational Waves from Neutron Star Binaries. *Phys. Rev. D*, 90(12):124091, 2014.

[199] W. O. Schumann. über die Dämpfung der elektromagnetischen Eigenschwingungen des Systems Erde — Luft — Ionosphäre. *Zeitschrift für Naturforschung A*, 7(3-4):250–252, March 1952.

[200] Noah Sennett, Richard Brito, Alessandra Buonanno, Victor Gorbenko, and Leonardo Senatore. Gravitational-Wave Constraints on an Effective Field-Theory Extension of General Relativity. *Phys. Rev. D*, 102(4):044056, 2020.

[201] Lijing Shao. Combined search for anisotropic birefringence in the gravitational-wave transient catalog GWTC-1. *Physical Review D*, 101(10):104019, May 2020.

[202] Vasileios Skliris, Michael R. K. Norman, and Patrick J. Sutton. Real-Time Detection of Unmodelled Gravitational-Wave Transients Using Convolutional Neural Networks, September 2020.

[203] Adam R. Solomon and Mark Trodden. Higher-derivative operators and effective field theory for general scalar-tensor theories. *Journal of Cosmology and Astroparticle Physics*, 2018(02):031–031, February 2018.

[204] Thomas P. Sotiriou and Shuang-Yong Zhou. Black Hole Hair in Generalized Scalar-Tensor Gravity. *Physical Review Letters*, 112(25):251102, June 2014.

[205] Thomas P. Sotiriou and Shuang-Yong Zhou. Black hole hair in generalized scalar-tensor gravity. *Phys. Rev. Lett.*, 112:251102, 2014.

[206] Thomas P. Sotiriou and Shuang-Yong Zhou. Black hole hair in generalized scalar-tensor gravity: An explicit example. *Physical Review D*, 90(12):124063, December 2014.

[207] Varun Srivastava, Derek Davis, Kevin Kuns, Philippe Landry, Stefan Ballmer, Matthew Evans, Evan D. Hall, Jocelyn Read, and B. S. Sathyaprakash. Science-driven Tunable Design of Cosmic Explorer Detectors. *The Astrophysical Journal*, 931(1):22, May 2022.

[208] Colm Talbot and Eric Thrane. Measuring the Binary Black Hole Mass Spectrum with an Astrophysically Motivated Parameterization. *The Astrophysical Journal*, 856(2):173, April 2018.

[209] J. H. Taylor, L. A. Fowler, and P. M. McCulloch. Measurements of general relativistic effects in the binary pulsar PSR1913 + 16. *Nature*, 277(5696):437–440, February 1979.

[210] The 1M2H Collaboration The Dark Energy Camera GW-EM Collaboration The DES Collaboration The DLT40 Collaboration The Las Cumbres Observatory Collaboration The VINROUGE Collaboration The MASTER Collaboration The LIGO Scientific Collaboration, The Virgo Collaboration. A gravitational-wave standard siren measurement of the Hubble constant. *Nature*, 551(7678):85–88, November 2017.

[211] The Virgo Collaboration The LIGO Scientific Collaboration. A Gravitational-wave Measurement of the Hubble Constant Following the Second Observing Run of Advanced LIGO and Virgo. *The Astrophysical Journal*, 909(2):218, March 2021.

[212] The Dark Energy Survey Collaboration The LIGO Scientific Scientific Collaboration, The Virgo Collaboration. First Measurement of the Hubble Constant from a Dark

Standard Siren using the Dark Energy Survey Galaxies and the LIGO/Virgo Binary–Black-hole Merger GW170814. *The Astrophysical Journal Letters*, 876(1):L7, April 2019.

[213] E. Thrane, N. Christensen, and R. M. S. Schofield. Correlated magnetic noise in global networks of gravitational-wave detectors: Observations and implications. *Physical Review D*, 87(12):123009, June 2013.

[214] E. Thrane, N. Christensen, R. M. S. Schofield, and A. Effler. Correlated noise in networks of gravitational-wave detectors: Subtraction and mitigation. *Physical Review D*, 90(2):023013, July 2014.

[215] Nami Uchikata, Hiroyuki Nakano, Tatsuya Narikawa, Norichika Sago, Hideyuki Tagoshi, and Takahiro Tanaka. Searching for black hole echoes from the LIGO-Virgo catalog GWTC-1. *Physical Review D*, 100(6):062006, September 2019.

[216] C. S. Unnikrishnan. IndIGO and LIGO-India: Scope and plans for gravitational wave research and precision metrology in India. *International Journal of Modern Physics D*, 22(01):1341010, January 2013.

[217] William G. Unruh and Robert M. Wald. Information loss. *Reports on Progress in Physics*, 80(9):092002, July 2017.

[218] V. Kalogera *et al.* The Next Generation Global Gravitational Wave Observatory: The Science Book, November 2021.

[219] Michele Vallisneri. Use and Abuse of the Fisher Information Matrix in the Assessment of Gravitational-Wave Parameter-Estimation Prospects. *Physical Review D*, 77(4):042001, February 2008.

[220] Michele Vallisneri and Nicolás Yunes. Stealth bias in gravitational-wave parameter estimation. *Physical Review D*, 87(10):102002, May 2013.

[221] Salvatore Vitale and Walter Del Pozzo. How serious can the stealth bias be in gravitational wave parameter estimation? *Physical Review D*, 89(2):022002, January 2014.

[222] Robbie Vogt, Fred Raab, Ronald Drever, Kip Thorne, and Rainer Weiss. A laser interferometer gravitational wave observatory (LIGO). Technical report, December 1989.

[223] Robert M. Wald. *General Relativity*. University of Chicago Press, Chicago, 1984.

[224] J. Weber. Detection and Generation of Gravitational Waves. *Physical Review*, 117(1):306–313, January 1960.

[225] J. Weber. Evidence for Discovery of Gravitational Radiation. *Physical Review Letters*, 22(24):1320–1324, June 1969.

[226] J. Weber. Anisotropy and Polarization in the Gravitational-Radiation Experiments. *Physical Review Letters*, 25(3):180–184, July 1970.

[227] Steven Weinberg. Effective Field Theory for Inflation. *Physical Review D*, 77(12):123541, June 2008.

[228] Steven Weinberg. Effective field theory, past and future. *International Journal of Modern Physics A*, 31(06):1630007, February 2016.

[229] Rainer Weiss. Republication of: Electromagnetically coupled broadband gravitational antenna. *General Relativity and Gravitation*, 54(11):153, November 2022.

[230] P. Welch. The use of fast Fourier transform for the estimation of power spectra: A method based on time averaging over short, modified periodograms. *IEEE Transactions on Audio and Electroacoustics*, 15(2):70–73, June 1967.

[231] Julian Westerweck, Alex B. Nielsen, Ofek Fischer-Birnholtz, Miriam Cabero, Collin Capano, Thomas Dent, Badri Krishnan, Grant Meadors, and Alexander H. Nitz. Low significance of evidence for black hole echoes in gravitational wave data. *Physical Review D*, 97(12):124037, June 2018.

[232] Clifford M. Will. Bounding the mass of the graviton using gravitational-wave observations of inspiralling compact binaries. *Physical Review D*, 57(4):2061–2068, February 1998.

[233] Clifford M. Will. The Confrontation between General Relativity and Experiment. *Living Rev. Rel.*, 17:4, 2014.

[234] Clifford M. Will. *Theory and Experiment in Gravitational Physics*. Cambridge University Press, Cambridge, United Kingdom ; New York, NY, USA, second edition edition, 2018.

[235] S. E. Woosley, A. Heger, and T. A. Weaver. The evolution and explosion of massive stars. *Reviews of Modern Physics*, 74(4):1015–1071, November 2002.

[236] Kent Yagi, Leo C. Stein, and Nicolás Yunes. Challenging the presence of scalar charge and dipolar radiation in binary pulsars. *Physical Review D*, 93(2):024010, January 2016.

[237] Kent Yagi, Leo C. Stein, Nicolás Yunes, and Takahiro Tanaka. Post-Newtonian, quasicircular binary inspirals in quadratic modified gravity. *Physical Review D*, 85(6):064022, March 2012.

[238] Huan Yang, Kent Yagi, Jonathan Blackman, Luis Lehner, Vasileios Paschalidis, Frans Pretorius, and Nicolás Yunes. Black hole spectroscopy with coherent mode stacking. *Phys. Rev. Lett.*, 118(16):161101, 2017.

[239] Nicolas Yunes and Frans Pretorius. Fundamental Theoretical Bias in Gravitational Wave Astrophysics and the Parameterized Post-Einsteinian Framework. *Phys. Rev. D*, 80:122003, 2009.

[240] Nicolas Yunes, Kent Yagi, and Frans Pretorius. Theoretical Physics Implications of the Binary Black-Hole Mergers GW150914 and GW151226. *Physical Review D*, 94(8):084002, October 2016.

[241] Aaron Zimmerman, Carl-Johan Haster, and Katerina Chatziioannou. On combining information from multiple gravitational wave sources. *Phys. Rev. D*, 99(12):124044, 2019.

APPENDICES

Appendix A

Appendix for Chapter 3

A.1 Modeling residual strain

In the previous section, we discussed the template constructed to recover signal from the cross-correlation power spectrum. In this section, we will briefly describe the template that can be used to model any deviation on the strain. Instead of modeling the residual power, $\mathcal{S}_\theta(t)$, we can model the residual strain Δs_θ. The decomposition of the signal in terms of template functions (Eq. (2.28)) becomes

$$\Delta s_{\theta_{\rm MLE}}(t) = \sum_{i=1}^{i=n} \beta_i(\theta_{\rm MLE})\zeta_i(f(t)), \tag{A.1}$$

where the coefficients βi and bases ζ_i give α_i and Z_i when cross-correlated using Eq. (2.20). In this case, both sides of the equation still depend on the timescale τ, but they take values in strain rather than strain power.

In analogy to Eq. (2.34), we can write the estimator for β as

$$\hat{\beta}_i(\theta_{\rm MLE}) = \int_{t_s}^{t_e} dt W_i(t) D(t)^{1/2} \zeta_i, \tag{A.2}$$

with $W_i(t) = K_n^{-1}(t)/\int_{t_s}^{t_e} K_n^{-1}(t)\zeta_i(t)^2 dt$. The corresponding SNR is

$$\rho_i^2 = \sum_{x=1,x'>x}^{N_{\rm det}} \sum_j^{N_{GW}} \left(\frac{(\hat{\beta}_i^{xx'}(\theta_{\rm MLE}))^2}{\left(K_{\beta_i}^{xx'}\right)^2} \right)_j, \tag{A.3}$$

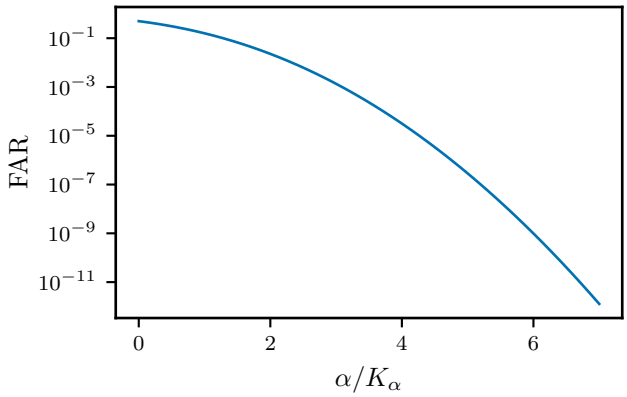


Figure A.1: FAR on the measurement of α for Gaussian, stationary noise. We define the FAR for a value of the projection coefficient α as the probability of obtaining a measurement equal or greater to α from data without a signal. Since our noise is Gaussian and stationary, this is given by the survival function of a Gaussian distribution. Here, we plot the survival function for the normal distribution, which gives the FAR as a function of the ratio of α to the error on α.

where, $\left(K^{xx'}_{\beta_i}\right)^2$ is the noise on the parameter β is defined as

$$(K^{xx'}_{\beta_i})^2 = \int_{t_s}^{t_e} dt \left(W_i(t) K_n^{\frac{1}{2}} \zeta_i(t)\right)^2, \tag{A.4}$$

where there is now a square root on K_n.

Again for a Gaussian, stationary, uncorrelated noise, we will get a $\sqrt{N_{GW}}$ enhancement in the SNR by combining $N_{\rm GW}$ events and number of detector pairs $\sqrt{N_{\rm det}(N_{\rm det}-1)/2}$.

A.2 False Alarm Rate

False Alarm Rate (FAR) measures the probability of detecting a signal when it is absent from the data. In the LVK catalogs [12, 17, 23], the FARs reported are computed using real data and using different methods depending on the pipeline used. In this work, we define the FAR for a given value of α as the probability of obtaining a value of α equal or greater when there is no signal in the data. As we are considering Gaussian, stationary noise, the (frequentist) distribution of α measurements from noise is a Gaussian distribution centred

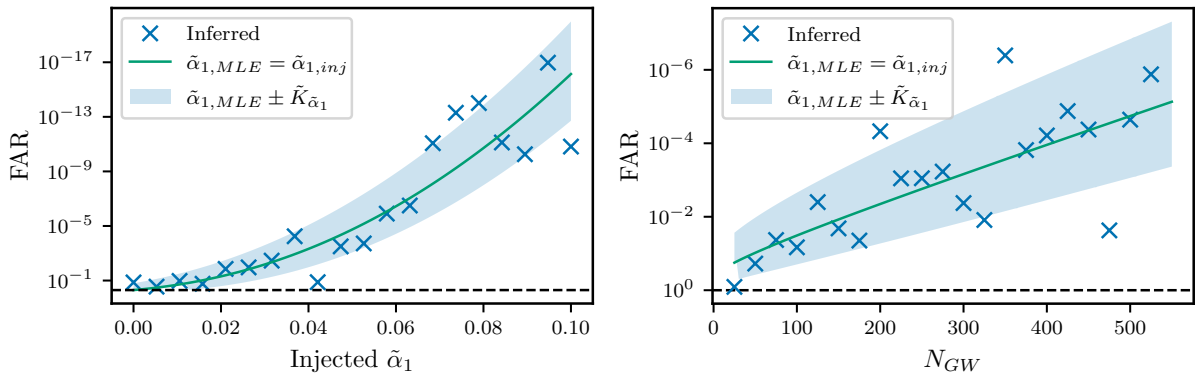


Figure A.2: FAR, or the probability of measuring a projection coefficient equal or greater to $\tilde{\alpha}_1$. The y-axis scale has been inverted to show that the FAR scales in the same way as $\mathcal{B}^{\rm BM}_{\rm SM}$, the Bayes factor in favour of a BM hypothesis, shown in Fig. 3.6. The dashed line is a visual aid indicating a FAR of 0.5.

around zero, with variance given by Eq. (2.37). The FAR is then the survival function of this Gaussian evaluated at α:

$$\text{FAR}(\alpha) = 1 - \int_{-\infty}^{\alpha} d\alpha \frac{1}{K_\alpha \sqrt{2\pi}} \exp\left(-\frac{1}{2}\left(\frac{\alpha}{K_\alpha}\right)^2\right)$$

The FAR for any pair of measured α and K_α can be obtained by substituting α/K_α in the survival function for the normal distribution, plotted in Fig. A.1. The same can be done with $\tilde{\alpha}_1/\tilde{K}_\alpha$.

The FAR scales with the injected projected coefficient and the number of events in the same way as the Bayes factor, as shown in Fig. A.2. In future work, we will compute the FAR by considering available GW data and how often an event that is not believed to contain any BM signal can lead to a non-zero measurement of the projection coefficients.